Seeing Sound: Dynamical Effects in Ultrafast X-ray Diffraction

by

Matthew F. DeCamp

A dissertation submitted in partial fulfillment
of the requirements for the degree of
Doctor of Philosophy
(Physics)
in The University of Michigan
2002

Doctoral Committee:

Professor Philip H. Bucksbaum, Chair
Professor Roberto Merlin
Assistant Professor Georg Raithel
Assistant Professor Alberto Rojo
Adjunct Professor John Whitaker

ACKNOWLEDGEMENTS

There are many people that I would like to thank. Without their mental and physical support this Ph.D. thesis would not have been possible.

First, to my scientific mentor Phil Bucksbaum. Without your wisdom and foresight I may never have started down the path that I have taken. Your leadership and guidance have made this trip enjoyable and fruitful. I can only hope that someday I can be as good a role model for future scientists as you have been for me.

To David Reis. For over 2 years you and I have argued, laughed, ate, drove, rode tricycles, and slept our way through experiments. If you had never been involved with this project three things would have happened: I would have never slept at Argonne, I would have never understood dynamical diffraction, and this thesis would never have been finished. Thank you for being a great colleague and a good friend.

To Roberto Merlin and Roy Clarke. Thank you for showing me that being a successful researcher is not incompatible with being an approachable colleague.

To John Zerger, Liz Tabak, John Carlson and the rest of the Game Show Hosts All-Stars and Grumpy Old Men. Thanks for proving that you can study physics and see the light of day too.

To John Caraher and Jared Wahlstrand. Thank you for volunteering your time and energy to this project. Without your help and friendship I would have gone crazy at Argonne.

To Jae Ahn, Dohn Arms, Eric Dufresne, Marc Hertlein, Catherine Herne, Brett

Pearson, Emily Peterson, Chitra Rangan, and Tom Weinacht. It takes quite a bit to make coming to work enjoyable, but somehow you guys made it easy.

To Pop, Alice, and Chris: Thank you for always being there.

To Mom and Dad: Your endless support and guidance has allowed me to pursue my goals and dreams. I can never repay you for what you have given me.

To Aaron: You have always given me a shoulder to turn to when life was hard or easy. I will always treasure your humor and insight. Thank you for being my best friend.

To Lisa: There are no words that can describe what you mean to me. For 9 years you have been beside me as a friend and loyal supporter. Thank you for enduring the long experiments that make me disappear for days on end. Thank you for being there when I needed you the most. Thank you for making me want to come home at night. And most of all, thank you for being the love of my life.

TABLE OF CONTENTS

LIST OF TABLES

Table

LIST OF FIGURES

Figure

LIST OF APPENDICES

Appendix

CHAPTER I

Introduction

Ultrafast x-ray diffraction has become a very powerful tool in studying structural dynamics of solids. The wave nature of x-rays allows the detection of milliÅngstrom changes in crystalline structure. Coupling the sensitivity of x-ray scattering with the ultrafast techniques developed for optical systems can provide unprecedented studies of ultrafast dynamics in solids. This thesis demonstrates how ultrafast x-ray diffraction can be used to view transient strains in crystalline solids.

1.1 Coherent Phonon Generation and Detection

The fundamental unit of motion in solids is a phonon. Two flavors of phonons exist in materials; optical phonons (motion of atoms within a crystalline unit cell) and acoustic phonons (crystalline lattice motion). A coherent phonon can be generated by using an optical pulse whose pulsewidth is shorter than one half the vibrational period. Crystalline lattice dynamics are typically measured indirectly through optical scattering techniques (i.e. Raman scattering). The time evolution of a coherent phonon can be measured by introducing an optical delay between a pump and a probe pulse (see figure 1.1).

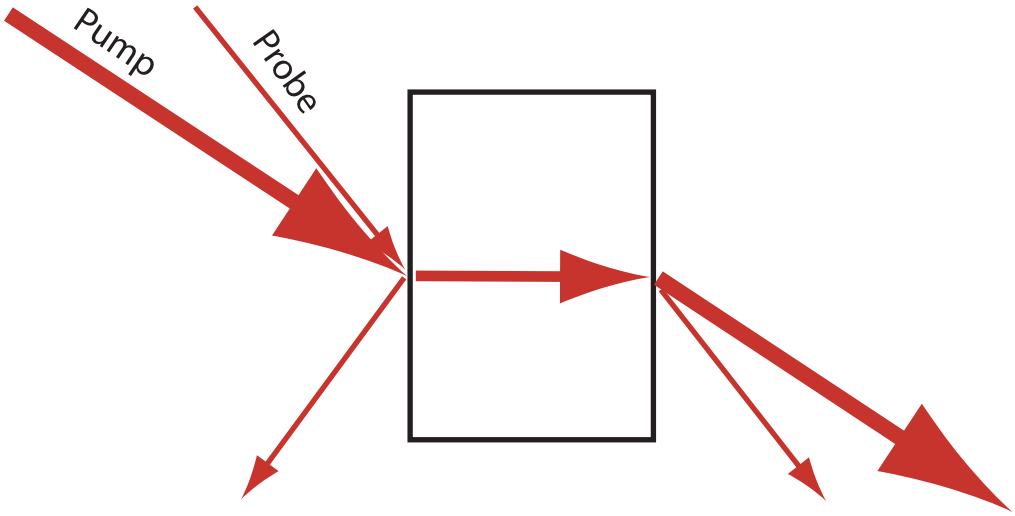

Figure 1.1: Typical optical pump-probe geometries.

The change in optical transmission and/or optical reflectivity is proportional to the relative phase and amplitude of a coherent phonon. The study of picosecond acoustic phonons first used the optical transmission technique [1] (see figure 1.2). Although transmission measurements are sensitive to lattice distortions, optical transmission does not provide a localized measurement of phonons. In the reflection geometry, however, the limited penetration depth of the incident light can be utilized to measure localized strains. This method has been very successful in the detection and measurement of ultrafast acoustic pulses [2, 3, 4, 5] (see section 2.2). Recently these optical techniques have been extended to the study of optical phonon generation [6, 7, 8] (see section 2.1).

Optical pump-probe techniques, though very successful, only provide indirect structural information. Measuring the atomic positions directly is impossible since the wavelength of optical radiation is orders of magnitude larger than the atomic spacing in a crystal lattice. X-ray scattering, however, is a proven technique for

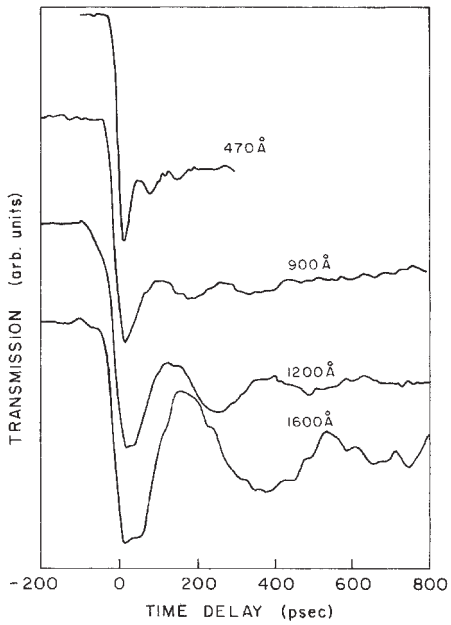

Figure 1.2: Observation of coherent acoustic phonon oscillations by an optical time-resolved transmission experiment. Adapted from [1]

providing precise information about atomic positions in crystalline lattices [9, 10, 11]. X-ray scattering is also sensitive to lattice motion if that motion is slow compared to the natural timescale of x-ray diffraction (∼1fs).

1.2 Previous work in Time-Resolved X-ray diffraction

Experiments performed with coherent acoustic waves demonstrated the sensitivity of x-ray diffraction to acoustic excitation[12, 13, 14, 15]. An accurate time-resolved picture of the structural dynamics within solids can be obtained by combining techniques developed for optical scattering and x-ray scattering. The early time-resolved x-ray diffraction (TRXD) experiments utilized laser based x-ray sources [16, 17, 18]. The hot dense plasmas generated by an ultrafast laser pulse provide a mechanism to generate hard x-rays[19, 20]. The generated x-rays are as monochro-

matic as the width of inner shell electron resonance, which for many diffraction applications is sufficient.

1.2.1 Laser based x-ray sources

The first experiments to utilize this fast source of narrow band x-rays examined the propagation of acoustic shockwaves generated by an ∼100ps optical pulse[16, 17]. The amount of lattice distortion imparted by the shockwave was inferred by solving the x-ray wave equation at different times and comparing the calculation to the observed diffraction patterns. These experiments demonstrate the ability of time-resolved x-ray diffraction to detect and measure strong acoustic disturbances in crystals. The time resolution was limited by the x-ray pulse length. Although ∼100ps is able to measure shockwave propagation, it is still several orders of magnitude slower than natural timescales of atomic motion in solids (typically 0.01-10ps).

To generated a sub-picosecond source of x-rays, faster more intense optical radiation is required. Ti:Sapphire modelocked oscillators and chirped pulse amplification (see section 4.3) can generate optical pulses with sub-picosecond pulse lengths and pulse energies of many milliJoules. These laser systems have the potential to generate ultrafast x-ray pulses (subpicosecond) which can enable the study crystalline disturbances on the natural timescales of nuclear motion[21, 20, 22]. This ultrafast source of x-rays has been used to study the mechanism of rapid heating in crystals. Rapid heating of the crystal surface can dramatically alter the x-ray diffraction patterns. Rischel *et al.* [23] showed that if a thin film is rapidly heated the efficiency of a Bragg reflection is reduced on a picosecond timescale (figure 1.3). The data

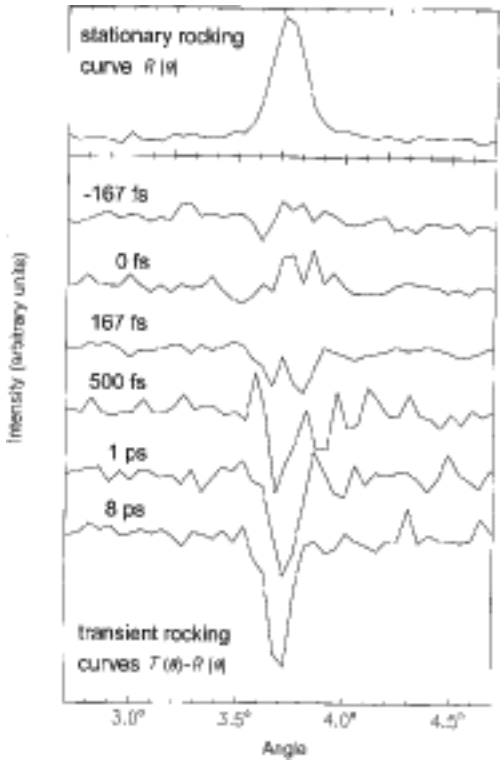

Figure 1.3: Time-resolved rocking curves of a crystal undergoing 'non-thermal melting'. The curves presented are the difference between the heated lattice and the static lattice. Adapted from [23].

were interpreted as 'non-thermal melting', or the loss of the long range order on a supersonic timescale. Siders *et al.* [24] demonstrated a similar effect in a bulk crystal.

Simple heating is an incoherent process. The study of phonon dynamics requires a coherent lattice vibration. Thomsen *et al.* [2] described an efficient method of generating a coherent acoustic pulse (see section 2.2). As the incident laser power is reduced to below the melt threshold, a coherent acoustic phonon can be generated. This coherent lattice motion changes the x-ray diffraction patterns over time [19, 25, 26] (see figure 1.4). With the help of dynamical diffraction theory (see chapter III), the coherent acoustic pulse was compared to the Thomsen model of ultrafast

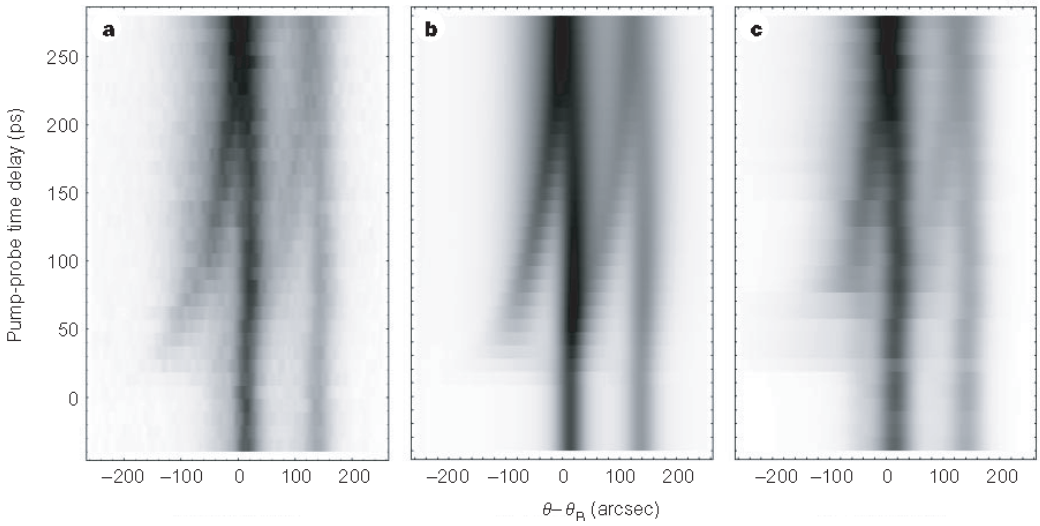

Figure 1.4: Time-resolved rocking curves of an impulsively generated acoustic pulse. (a) is data using a laser-plasma x-ray source, (b) is a dynamical theory calculation based on the Thomsen model of acoustic strain generation, and (c) the best fit acoustic pulse found by a fitting algorithm. Adapted from [19].

acoustic pulse generation.

The laser based experiments, while ground breaking, have some systematic drawbacks. First, the x-rays generated from a laser based plasma source radiate in all directions. The divergence poses significant problems in the collection of useable x-ray photons. Second, in many materials that are used to generate x-rays, there are multiple emission lines in a very narrow energy range. The lack of monochromaticity interferes with the precise interpretation of the x-ray diffraction patterns. In the studies on acoustic pulse propagation, for example, the compression component of acoustic pulse is not immediately apparent because of the two nearby emission lines (see figure 1.4)[19]. An x-ray synchrotron source is designed to compensate for these two systematic problems.

1.2.2 Time-Resolved Studies at synchrotron Sources

X-ray synchrotrons can generate a large number of hard x-ray photons without the divergence problems associated with laser based x-ray sources. The use of simple x-ray optics, which can make the x-rays spectrally pure, can be utilized without significantly deteriorating the average x-ray intensity (see chapter IV). The spectral and spatial attributes of a synchrotron, however, come at a price. The x-ray pulse width is limited by the accelerating electron bunches which generate the radiation, which typically is 50-100ps in duration. There have been a number of advances which extend the effective time-resolution of an x-ray synchrotron.

Larsson *et al.* [27]presented data which measured the time-resolved diffraction efficiency of a laser heated crystal. A ∼1ps lattice change was measured using an 80ps x-ray pulses and a two crystal cross-correlation technique.

Direct manipulation of the synchrotron electron beam is also a potential source of fast x-rays. Part of the electron bunch may be differentially excited by an ultra-fast laser via Thomson scattering. The sub-picosecond excited electron bunch will generate a sub-picosecond x-ray pulse[28, 20]. Chin *et al.* [29] used this method to show that impulsively heated crystals could shift the energy of scattered x-rays by the acoustic phonon energy.

The least invasive method of detecting picosecond structural changes in a long x-ray pulse is an x-ray streak camera (see section 4.2.3). X-ray streak cameras map the time-intensity distribution of an x-ray pulse. Averaging a series of x-ray pulses, the maximum resolution of an x-ray streak camera is ∼2ps[30]. Lindenberg *et al.*

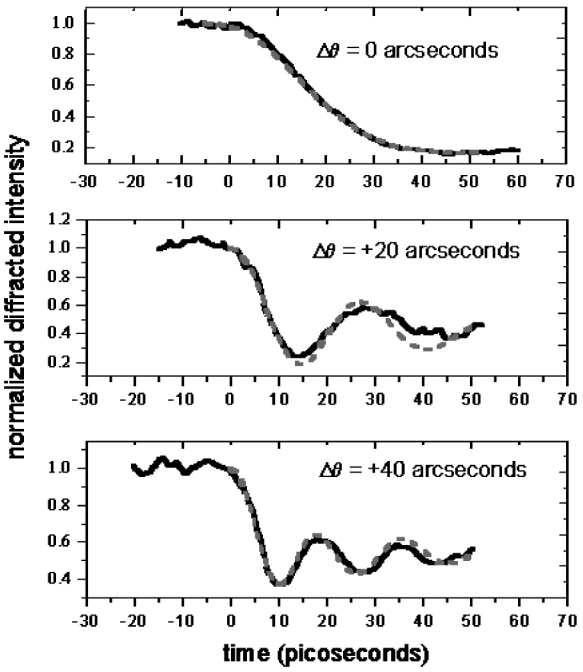

Figure 1.5: Measured (solid line) and calculated (dashed) acoustic phonon spectra using a picosecond x-ray streak camera. Adapted from [31].

[31] used an x-ray streak camera to measure the frequency spectrum of a coherent acoustic pulse and compared the results to the theory developed by Thomsen *et al.* [2] (figure 1.5).

These experiments, though novel, did not use the full resources of a synchrotron. This thesis reports the ability to meld ultrafast pump-probe techniques with the monochromaticity of synchrotron x-pulses. The study of acoustic pulses is expanded to include a full spectrum analysis of the generated acoustic pulse as well as the study of the long term (microsecond) evolution of acoustic pulses in crystals. The data demonstrates that the Thomsen model of strain generation and propagation does not predict all of the observed x-ray diffraction patterns in laser heated crystals (chapter V). This thesis will also demonstrate novel experiments that utilize Laue diffraction to study strain propagation (chapters VI and VII). In the same way that

optical pump-probe techniques were extended to THz regime, the x-ray pump-probe techniques developed and demonstrated in this thesis could be extended to the study of coherent optical phonons and other ultrafast phenomena.

CHAPTER II

Ultrafast Lattice Motion

For decades the study of phonons was limited to the frequency domain. Stable sources of ultrafast optical pulses allows the generation and study of coherent phonon oscillations in the time-domain. Ultrafast lattice dynamics is split into two distinct regimes; high frequency (optical phonons) and low frequency (acoustic phonons). Although the same laser can generate both coherent optical and coherent acoustic phonons simultaneously, the mechanism for their generation is vastly different.

2.1 Coherent Optical Phonon Generation

Optical phonons are the vibrational modes of a crystalline unit cell. The fundamental frequencies of these oscillations range from 1-10's THz depending on the bonding strengths and the mass of the atoms within the atomic lattice. Stimulated Raman scattering is a standard method by which an optical phonon mode may be excited. Two light sources, whose frequency difference is equal to the optical phonon frequency, transfer energy to the specific phonon mode. If the two light sources are mutually incoherent, then the relative phase of the oscillations within neighboring unit cells is random and thus the phonon is said to be incoherent. If, however, the

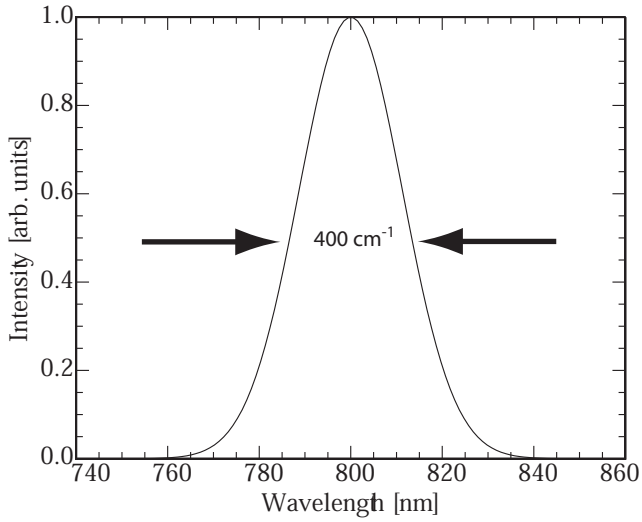

Figure 2.1: The spectrum of an ultrafast optical pulse. The bandwidth is large enough to excite a coherent $400\,cm^{-1}$optical phonon mode.

Raman transition takes place within one half a phonon period, all the unit cells can be excited with the same relative phase and thus the phonon is said to be coherent.

Experimentally, a coherent optical phonon can be generated using an optical pulse whose pulse width is less than one half an optical phonon cycle. In this case the optical pulse possesses enough frequency bandwidth to satisfy the Raman transition (see figure 2.1). This method of exciting a coherent phonon mode is called Impulsive Stimulated Raman Scattering (ISRS)[32, 8].

2.1.1 Impulsive Stimulated Raman Scattering

ISRS has been used to generate coherent optical phonons in many systems, from insulators to semi-metals[6, 7, 33, 32, 8]. Many materials have atomic unit cells consisting of many atoms of various species and bond strengths. This diversity makes the Raman spectrum of these materials very complicated in the number and energy of the excited phonon modes. If an ultrafast optical pulse has enough bandwidth

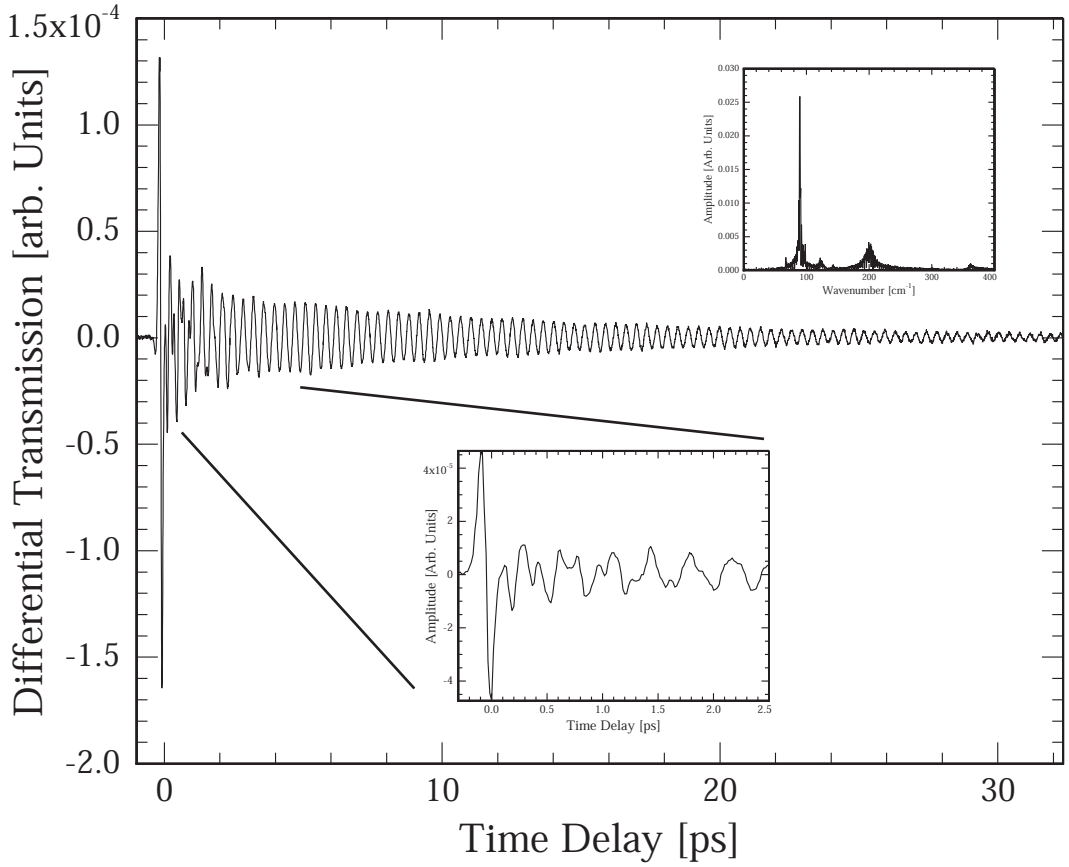

Figure 2.2: Time-resolved phonon spectra of a single BGO crystal. Inset: Fourier transform of the phonon oscillations.

and short enough pulse length, ISRS can excite many of the phonon modes simultaneously. $Bi_3Ge_4O_{12}$ (BGO) is such a system.

Figure 2.2 shows the time-resolved phonon oscillations in BGO excited by a 50fs optical pulse using ISRS. The phonon spectrum indicates the single optical pulse excited at least 6 coherent modes. The lifetime of these individual modes depends on the 'Q' of the particular phonon mode. After a few phonon cycles the only remaining mode is the $90\,cm^{-1}$.

Using multiple pump pulses it is possible to generate a set of optical phonons that have a specific phase relationship. Since the phonons are coherent, by generating

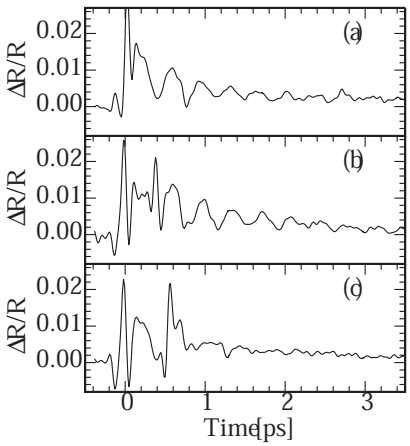

Figure 2.3: Coherent control of optical phonon mode in single crystal bismuth. (a) Single pulse excitation. (b) Double pulse excitation; constructive interference. (c) Double pulse excitation; destructive interference. Adapted from [36].

multiple phonons it is possible control the amplitude, phase, and specific mode that is excited. For a system that has only one observable phonon mode, two optical pulses are sufficient to achieve full control of the phonon [34, 35, 36](see figure 2.3).

More complicated systems require more degrees of freedom to control the lattice vibration. In figure 2.4 a semi-metal crystal consisting of a mix of antimony and bismuth has three accessible phonon modes [35]. As seen from the phonon spectra, a series of optical pulses can quench or amplify a specific Raman mode.

2.1.2 Amplitude of coherent lattice vibrations

The standard method of detecting coherent lattice vibrations is to measure the transient surface reflectivity or transient bulk transmission. The local index of refraction of the material changes as the coherent phonon oscillates leading to a change in the optical transmission and optical reflectivity. Since the index of refraction is a measurement of local crystal density, these optical techniques represent an indi-

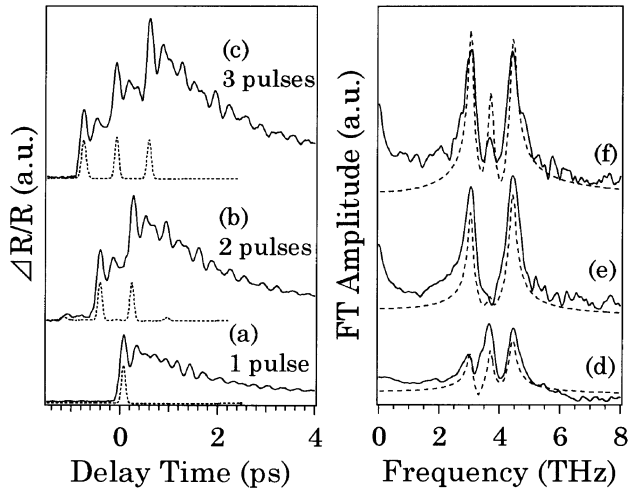

Figure 2.4: left: Coherent control of three phonon modes in antimony-bismuth semimetal blend. right: the corresponding fourier transforms. Adapted from [35].

rect measurement of atomic motion in solids. Using the mathematical formalism of Raman scattering, however, the absolute amplitude of the lattice motion may be estimated.

Assuming that the optical phonon mode is harmonic, the generated phonon field at a crystal surface due to an impulsive optical pulse is given by[32]:

$$Q = \frac{1}{\Omega_0}\int_{-\infty}^{\infty} d\omega \frac{E(\omega)E^*(\omega \pm \Omega_0)\Re_Q(\omega, \omega \pm \Omega_0)}{\eta(\omega)\eta(\omega \pm \Omega_0)} \tag{2.1}$$

where $E(\omega)$ is the incident electric field, Ω_0 is the optical phonon frequency, and $\Re_Q$ is a Raman tensor which can be approximated in terms of the complex dielectric constant[37, 38]:

$$\Re_Q(\omega, \omega \pm \Omega) \sim D\frac{\epsilon^*(\omega) - \epsilon(\omega \pm \Omega)}{\pm\Omega} \tag{2.2}$$

where D is some deformation potential and $\eta(\omega)$ is defined in terms of the complex index of refraction:

$$\eta(\omega) \equiv 1 + n(\omega) + i\kappa(\omega) \tag{2.3}$$

If the optical properties of the crystal are known, an estimate of the phonon amplitude may be obtained. In a semi-metal, for example, the amplitude of the ion motion is approximated by (see appendix A)[36]:

$$U_0^2 \sim \left(\frac{\Delta R}{R}\right)_Q \frac{377\mathcal{F}}{\rho\nu_0|\epsilon|} \tag{2.4}$$

where U_0 is the ion displacement in Å, 377 is the vacuum impedance, $\mathcal{F}$ is the incident fluence of the excitation pulse in mJ/cm^2, ρ is the density of the material in amu/Å^3, and ν_0 is the phonon frequency in THz.

A coherent lattice vibration as large as 1% the equilibrium lattice condition can be inferred from optical reflectivity data (figure 2.5) and equation 2.4. Although the atomic motion of optical phonons can be quite large, the momentum associated with an optical phonon is only as large as the bandwidth of the generating laser. Coherent strain pulses, however, can possess momentum with very large amplitudes.

2.2 Bulk Crystal Strain

The response of a crystal upon a feeling a force is defined as the stress. The equations of motion for crystal in one dimension can then be defined as [39]:

$$\rho\frac{\partial^2 u_k}{\partial t^2} = \frac{\partial \sigma_{ki}}{\partial x_i} + \frac{\partial \sigma_{kj}}{\partial x_j} + \frac{\partial \sigma_{kk}}{\partial x_k} \tag{2.5}$$

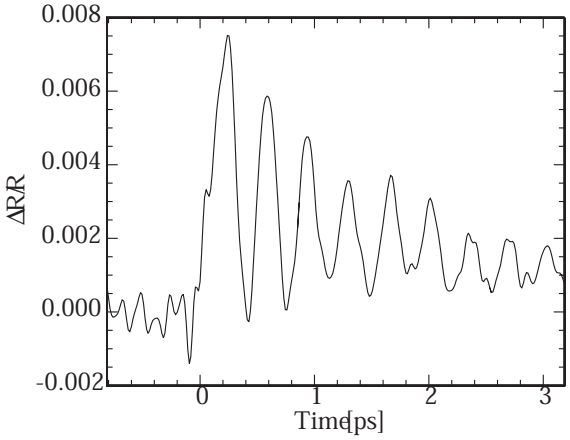

Figure 2.5: Time-resolved reflectivity change of the impulsively generated optical phonon in bulk bismuth. Adapted from [36]

Where ρ is the crystal density. If a strain is defined as the differential atomic displacement:

$$\eta_{ii} = \frac{\partial u_i}{\partial x_i} \tag{2.6}$$

$$\eta_{ij} = \frac{\partial u_j}{\partial x_i} + \frac{\partial u_i}{\partial x_j} \tag{2.7}$$

then the equations of motion may be defined in terms of the strain. If the crystal displacement is small, then the crystalline strain will be directly proportional to the stress (i.e. Hooke's Law). Therefore the strain tensor may be defined as:

$$\begin{pmatrix} C_{11} & C_{12} & C_{13} & C_{14} & C_{15} & C_{16} \\ C_{21} & C_{22} & C_{23} & C_{24} & C_{25} & C_{26} \\ C_{31} & C_{32} & C_{33} & C_{34} & C_{35} & C_{36} \\ C_{41} & C_{42} & C_{43} & C_{44} & C_{45} & C_{46} \\ C_{51} & C_{52} & C_{53} & C_{54} & C_{55} & C_{56} \\ C_{61} & C_{62} & C_{63} & C_{64} & C_{65} & C_{66} \end{pmatrix} \begin{pmatrix} \sigma_{11} \\ \sigma_{22} \\ \sigma_{33} \\ \sigma_{23} \\ \sigma_{13} \\ \sigma_{12} \end{pmatrix} = \begin{pmatrix} \eta_{11} \\ \eta_{22} \\ \eta_{33} \\ \eta_{23} \\ \eta_{13} \\ \eta_{12} \end{pmatrix} \tag{2.8}$$

where $\sigma_{13} = \sigma_{31}$,$\sigma_{23} = \sigma_{32}$, and $\sigma_{12} = \sigma_{21}$ because of symmetry and the coefficients of the matrix of the elastic moduli of the material [39].

Direction	C_{eff}
[100]	C_{11}
[110]	$\frac{1}{2}(C_{11}+C_{12}+2C_{44})$
[111]	$\frac{1}{3}(C_{11}+2C_{12}+4C_{44})$

Table 2.1: Table of elastic moduli of a longitudinal sound wave in various direction

In cubic crystals, the elastic moduli tensor may be simplified to the following matrix:

$$\begin{pmatrix} C_{11} & C_{12} & C_{12} & 0 & 0 & 0 \\ C_{12} & C_{11} & C_{12} & 0 & 0 & 0 \\ C_{12} & C_{12} & C_{11} & 0 & 0 & 0 \\ 0 & 0 & 0 & C_{44} & 0 & 0 \\ 0 & 0 & 0 & 0 & C_{44} & 0 \\ 0 & 0 & 0 & 0 & 0 & C_{44} \end{pmatrix} \tag{2.9}$$

thus for a strain along in the u_i direction, the equations of motion become:

$$\rho\frac{\partial^2 u_i}{\partial t^2} = C_{11}\frac{\partial \eta_{ii}}{\partial x_i} + C_{12}\left(\frac{\partial \eta_{jj}}{\partial x_i} + \frac{\partial \eta_{kk}}{\partial x_i}\right) + C_{44}\left(\frac{\partial \eta_{ij}}{\partial x_j} + \frac{\partial \eta_{ki}}{\partial x_k}\right) \tag{2.10}$$

Using equations 2.6 this equation may be reduced to:

$$\rho\frac{\partial^2 u_i}{\partial t^2} = C_{11}\frac{\partial^2 u_i}{\partial x_i^2} + C_{44}\left(\frac{\partial^2 u_i}{\partial x_j^2} + \frac{\partial^2 u_i}{\partial x_k^2}\right) + (C_{12}+C_{44})\left(\frac{\partial^2 u_j}{\partial x_i \partial x_j} + \frac{\partial^2 u_k}{\partial x_i \partial x_k}\right) \tag{2.11}$$

If it is assumed that the there is a longitudinal strain wave in the material ($u = u_0 e^{i(Kx-\omega t)}$) the sound speeds in various directions may be defined. Substituting the strain wave into the equation of motion the following equation is found $\omega^2\rho = C_{eff}K^2$. For a longitudinal strain, the sound speed is represented by $\sqrt{\frac{C_{eff}}{\rho}}$ assuming a linear acoustic dispersion relation. The C_{eff} for various crystalline directions is given in table 2.1.

2.2.1 Ultrafast Strain Generation

Crystalline strain can be generated in many different ways; Ion bombardment, multiple quantum wells, etc. Strains with central frequencies in the MHz regime can propagate by exciting an electric transducer at the crystal surface [12, 14, 15]. The absorption of ultrafast optical pulses may generate coherent strains with central frequencies in the GHz regime.

Thomsen Model

Thomsen *et al.*[2] presented a simple model which describes the generation and propagation of a laser induced coherent strain pulse. In optically opaque crystals, a significant amount of optical radiation can be absorbed on the crystal surface. This absorption will cause the surface temperature of a crystal to increase. Assuming that the illuminated area is large compared to the square of the optical absorption depth, η, the amount of energy deposited per unit volume at a distance z into the crystal bulk is given by:

$$W(z) = (1 - R)\frac{\mathcal{F}}{\eta}e^{-z/\eta} \tag{2.12}$$

where R is the surface reflectivity and $\mathcal{F}$ is the incident optical fluence. If the electron-phonon relaxation time is extremely fast (in semiconductors this typically is $\sim$1ps), a thermal gradient will be generated almost instantaneously:

$$\Delta T(z) = \frac{W(z)}{C} \tag{2.13}$$

where C is the specific heat per unit volume. The generated temperature differential produces a thermal stress in the $\hat{z}$ direction:

$$-3B\beta\Delta T(z) \tag{2.14}$$

where B is the bulk modulus of the material and β is the linear expansion coefficient.

Since the stress is only in the $\hat{z}$ direction the only nonzero component of the strain tensor is $\eta_{33} = \frac{\partial u_3}{\partial z}$. The thermo-elastic equations of motion (equation 2.5) can then be simplified:

$$\rho\frac{\partial^2 u_3}{\partial t^2} = \frac{\partial \sigma_{33}}{\partial z} \tag{2.15}$$

where σ_{33} is the component of stress tensor in the $\hat{z}$ direction given by:

$$\sigma_{33} = v^2\rho\eta_{33} - 3B\beta\Delta T(z) \tag{2.16}$$

where v is the longitudinal sound velocity in the material and the harmonic response of the material is represented by the first term. Thomsen *et al.* presented a solution to equation 2.15 with the assumption that initially the strain is zero everywhere and that the stress is zero at the crystal surface ($z = 0$):

$$\eta_{33}(z,t) = (1-R)\frac{F\beta}{\eta C}\frac{v^2\rho}{3B}\left[e^{-z/\eta}\left(1 - 0.5e^{-vt/\eta}\right) - 0.5e^{-|z-vt|/\eta}sgn(z-vt)\right] \tag{2.17}$$

Equation 2.17 represents a lattice strain with two separate components; a static thermal layer and a coherent acoustic pulse. By calculating the strain as a function of crystal depth for a few time steps, this partitioning of acoustic energy becomes clear (see figure 2.6). Optical scattering experiments have shown that this model is qualitatively correct[1, 2] (see figure 2.7). It is impossible, however, to get a

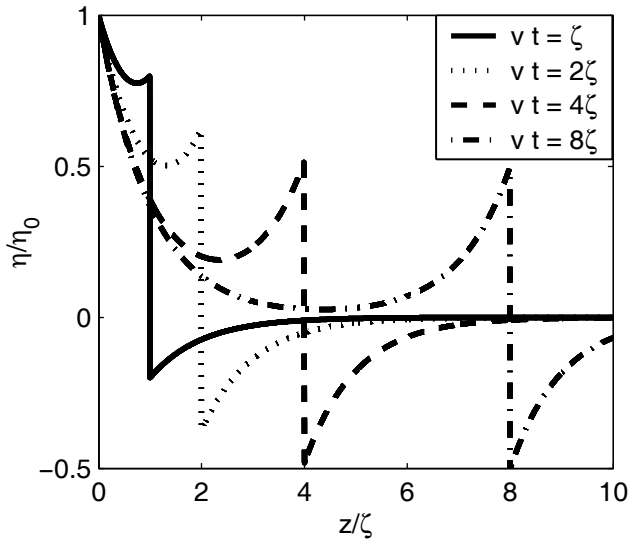

Figure 2.6: Calculated strain profiles at four different time delays using the Thomsen model.

measurement of the absolute lattice strain as well as the absolute partitioning of energy using optical scattering techniques.

Although the Thomsen model is analytically sound, the solution uses some physical assumptions that are inconsistent with 'real' world behavior. The discontinuity in the center of the acoustic pulse, for example, is due to the instantaneous generation of the thermal strain. In reality, this generation is governed by the electron-phonon coupling time, which for many semi-conductors is ∼10ps[19, 29, 31]. Incorporating the electron-phonon coupling into the Thomsen strain is equivalent to the smoothing of the discontinuity in the spatial domain or a Fourier filter in the frequency domain. To incorporate this spatial and temporal smoothing, the sgn function in equation 2.17 is replaced with a hyperbolic tangent[40].

The Thomsen model also assumes that the acoustic pulse shape does not distort with propagation. This assumption is valid only if the acoustic frequencies are rela-

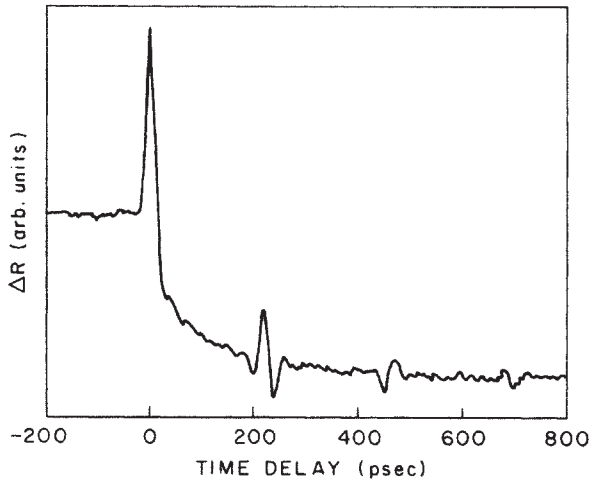

Figure 2.7: Time-Resolved reflectivity measurements of an impulsively generated acoustic pulse. Adapted from [2].

tively small and $\omega = ck$. However, if higher frequency acoustic phonons are generated the acoustic dispersion relation may include higher order terms, $\omega = ck - \gamma k^3$[3].

The consequence of higher order terms in the acoustic dispersion relation is that the acoustic pulse will spatially disperse by an amount:

$$\frac{x\gamma}{c(\Delta x)^2} \tag{2.18}$$

where Δx is the initial spatial extent of the acoustic pulse, which in the Thomsen model is $\sim 2\eta$. Physically this dispersion becomes significant when the acoustic pulse travels at least a distance x such that:

$$x = \frac{c(\Delta x)^3}{\gamma} \tag{2.19}$$

For ultrafast acoustic pulses generated in Ge ($\gamma \sim .85^{-11} cm^3 s^1$ [3]) the length scale where acoustic dispersion becomes important is ∼35m.

Other Methods of Generating Ultrafast Strain

The Thomsen model is not the only theory of generating a time-dependent strain with an ultrafast laser. Akhmanov and Gusev[41] present a generalized study of laser generated ultrafast acoustic pulses. Two other prevalent methods are described here which have relevance to this work; Electron-hole plasma diffusion and acoustic shockwaves.

Plasma Diffusion

When a large dense electron-hole plasma is generated at a crystal surface, boundary conditions require that the generated gradient must be relieved. The amount of particle flow is determined by the density gradient of the system[39].

$$J = -D\nabla n \tag{2.20}$$

where J is the particle current, D is the diffusion constant, and n is the density of particles in the system. This equation is called Fick's Law. If the continuity equation is maintained:

$$\frac{\partial n}{\partial t} + \nabla \cdot J = 0 \tag{2.21}$$

the following time-dependent diffusion equation may be derived:

$$\frac{\partial n}{\partial t} = D\nabla^2 n \tag{2.22}$$

If the density gradient is initially given by a delta function, the time-dependent density may be given of the form[42]:

$$n(x,t) = (4\pi Dt)^{-1/2}\, e^{-x^2/4Dt} \tag{2.23}$$

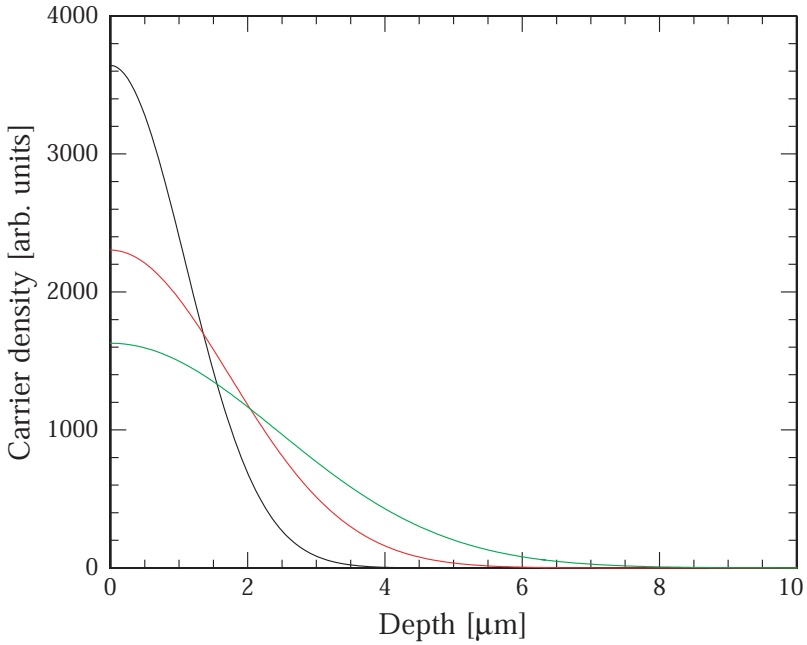

Figure 2.8: Time dependence of ultrafast carrier diffusion. Black 40ps, Red 100ps, and Green 200ps.

If n represents a dense electron-hole plasma, the evolution of this plasma will be governed by the equation above. Figure 2.8 shows the time-dependence of the electron-hole plasma assuming that initial carrier density is a delta function.

Assuming that the strain field is generated by the electron-hole plasma, the propagation of the strain field is not limited by the sound speed, but rather the speed of the electron-hole diffusion. The time evolution of this strain is completely dependent on the diffusion constant of the material, which for low carrier densities is constant. Young and van Driel [43] showed that large carrier densities ($10^{19} cm^{-3}$) can radically change the diffusion constant and thus the time dependence of the carrier diffusion (see figure 2.9). For typical incident laser fluences (1-10 $\frac{mJ}{cm^2}$), carrier densities are $\sim 10^{20} cm^{-3}$. In this fluence range, the diffusion constant should change linearly with optical fluence. This implies that the time-dependence of the diffusion will also

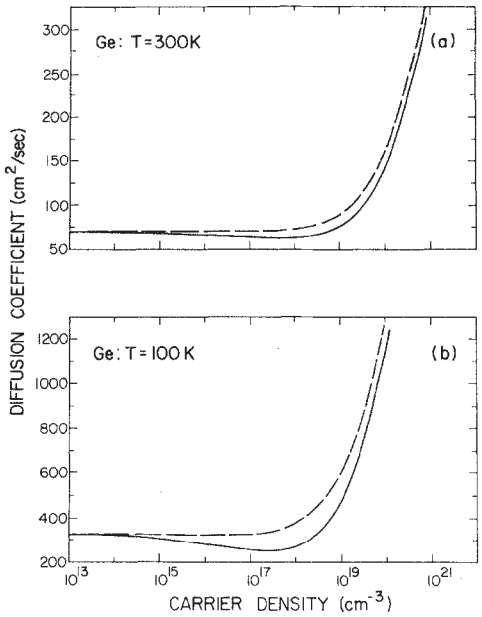

Figure 2.9: Carrier diffusion constant as a function of carrier density in Ge. Adapted from [43].

change with the incident optical fluence.

Shockwaves

Another method of generating strain is the generation of a supersonic shockwave. When material is ablated from a solid, momentum conservation requires that the crystal lattice will undergo a compression [16, 17]. If the ablation is performed using an ultrafast laser source, the resulting compression wave can induce a supersonic strain that propagates into the bulk.

2.3 Coherent folded acoustic phonons

The methods of phonon generation described in the previous sections have limitations. Optical phonons generated by ISRS possess very small wave vectors while the acoustic phonon generation had frequencies limited to ∼100GHz. Folded acous-

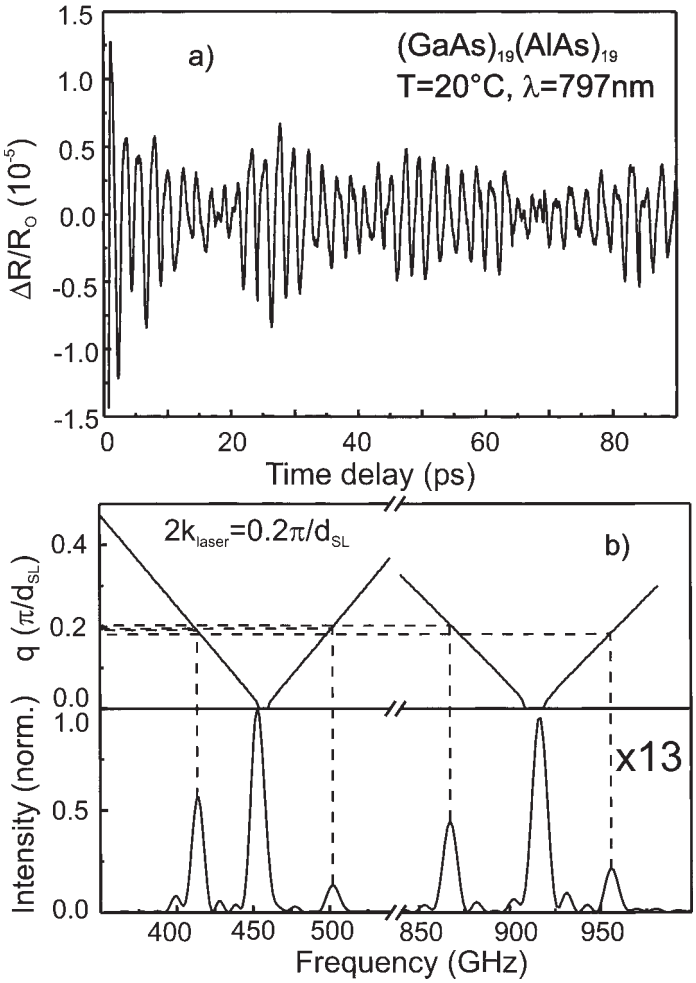

Figure 2.10: Coherent Folded acoustic phonons in a semiconductor superlattices. Adapted from [46, 44].

tic phonons are a combination of these two techniques; high wavevector coherent vibrations that have frequency components as large as 1THz.

Excitation of crystalline superlattices by an ultrafast optical pulse can cause the superlattice to vibrate coherently. The frequency of these coherent oscillations are given by the elastic response of the material and the multilayer periodicity. Frequencies as large as 1THz have been generated in standard superlattices (figure 2.10). Like optical phonon oscillations, it has been shown that vibrations within the multilayer are generated via ISRS[44, 45].

These coherent phonons have a complicated momentum structure. There are three prevalent modes; one corresponding to $q = 0$ and two corresponding to $q = \pm 2k_{laser}$. The large momentum phonon modes are attributed to Raman stimulation in a backscattering geometry [44]. The frequency of these large momentum sidebands is determined by the dispersion relation of the system:

$$\omega^2 = \frac{C_{11}}{\rho}(q + G)^2 \tag{2.24}$$

where G is the reciprocal lattice vector of the superlattice. Because these acoustic phonons are coherent, like the coherent optical phonons the relative motion and amplitude of the superlattice may be controlled[47, 48].

CHAPTER III

Theory of Dynamical Diffraction

The study of x-ray diffraction is spilt into two regimes; the kinematic regime where x-ray absorption is not important, and the dynamical regime where x-ray absorption must be taken into account. Kinematic diffraction uses the constructive interference of plane waves to predict diffraction patterns (see figure 3.1). Bragg's law can be derived from this constructive interference:

$$2d \sin \theta = \lambda \tag{3.1}$$

In many cases kinematic theory can correctly predict diffraction patterns. For the case of 'thick' perfect crystals, however, the diffraction patterns are governed by the theory of dynamical diffraction due to the non-negligible x-ray absorption. The mathematical formalism of dynamical diffraction theory is found by solving Maxwell's equations in a periodic medium.

3.1 X-ray Dispersion Surface

When an x-ray photon of certain momentum enters a periodic lattice, the x-rays will be deflected at an angle determined by the momentum of the crystalline

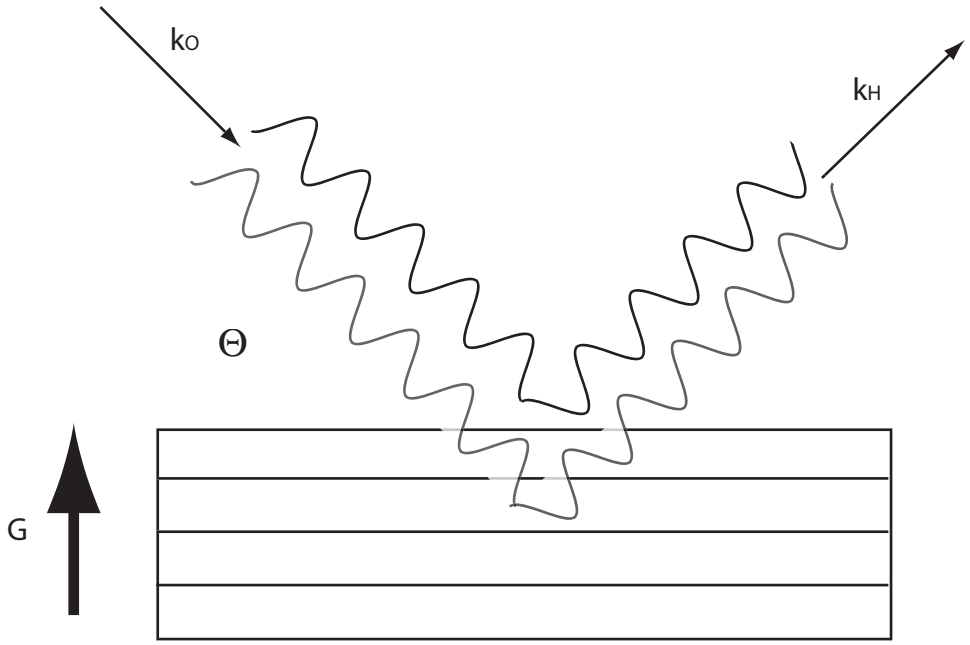

Figure 3.1: Kinematic diffraction

lattice (reciprocal lattice vector). Von Laue derived a scattering equation based on momentum conservation:

$$\mathbf{k}_H = \mathbf{k}_0 + \mathbf{G} \tag{3.2}$$

where $\mathbf{k}_{0,H}$ is the momentum of the incident and diffracted x-ray ray photon and $\mathbf{G} = \frac{1}{d}$ is the reciprocal lattice vector corresponding to a particular set of lattice planes. In the limit of elastic scattering, the Laue equation is an equivalent statement to Bragg's law but in 'reciprocal' space. In general, the incident and diffracted wave vectors are complex to account for absorption.

The Ewald construction is a graphical representation of the Laue equation[49]. A sphere is constructed of radius $2\pi/\lambda$ centered on a specific reciprocal lattice point 'O'(see figure 3.2). This sphere represents the possible momentum vectors of an x-ray photon of wavelength λ. The Ewald construction is completed by choosing a second

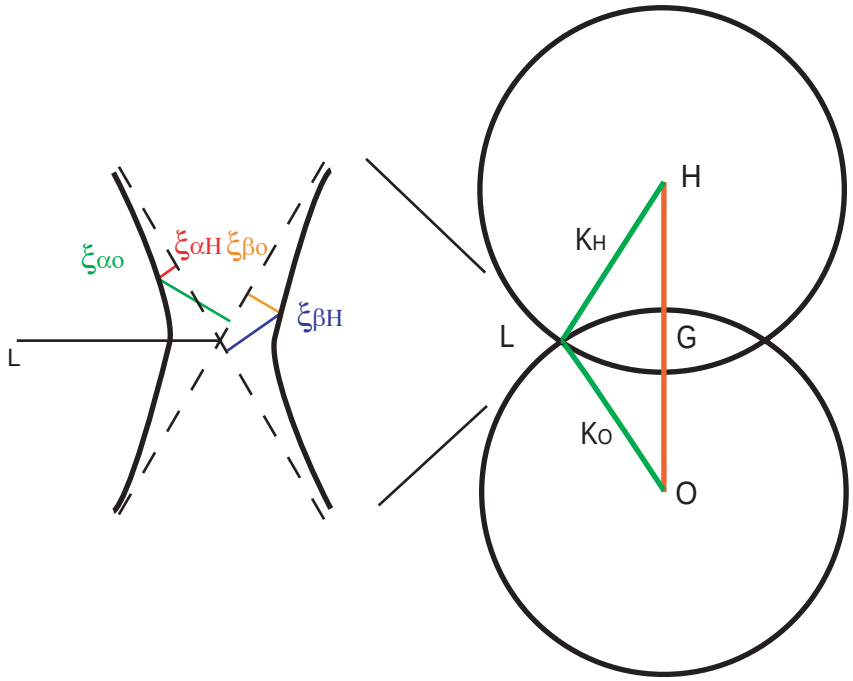

Figure 3.2: The Ewald construction and the X-ray dispersion surface.

reciprocal lattice point, 'H', and constructing another sphere of radius $2\pi/\lambda$. If $|4\pi/\lambda| \geq |\mathbf{G}|$ then the two spheres will intersect at the Laue point ('L') in reciprocal space. The triangle defined by the points O, H, and L graphically represent the Laue equation, where the lines $\overline{OL}$, $\overline{LH}$, and $\overline{OH}$ defines $\mathbf{k}_O$, $\mathbf{k}_H$, and $\mathbf{G}$ respectively.

The Ewald construction provides a simple, yet effective method of predicting the locations of x-ray reflections in reciprocal space. Near a diffraction peak, however, the Ewald construction is an incomplete physical description. To model the system accurately, the three dimensional periodicity of the atomic locations must be taken into account. The solutions to Maxwell's equations in a three dimensional crystal lattice will govern the wave propagation inside a crystal. Batterman and Cole[50] provide an efficient method of solving for the field amplitudes inside a crystal.

3.1.1 Solutions to the x-ray wave equation

Maxwell's equations for the propagation of electro-magnetic waves can be written in the form:

$$\nabla \times \mathbf{E} = -\frac{\partial \mathbf{B}}{\partial t} \tag{3.3}$$

$$\nabla \times \mathbf{H} = \frac{\partial \mathbf{D}}{\partial t} \tag{3.4}$$

where:

$$\mathbf{D} = \epsilon_0(1+\psi)\mathbf{E} \tag{3.5}$$

and where ψ is the complex dielectric constant of the material. Assuming the crystal has a spatially periodic index of refraction, the solutions to Maxwell's equations are Bloch functions [49, 39, 51, 52]:

$$\mathbf{A} = \sum_H \mathbf{A}_H e^{i\omega t - 2i\pi \mathbf{k}_H \cdot \mathbf{r}} \tag{3.6}$$

where $\mathbf{A}$ can be any of the components of the electro-magnetic field ($\mathbf{D}$,$\mathbf{E}$, or $\mathbf{B}$). The sum represents a sum over all reciprocal lattice points. Incorporating equation 3.6 into equations 3.3 and 3.4 a system of equations can be obtained (see appendix B):

$$\mathbf{k}_H \times (\mathbf{k}_H \times \mathbf{E}_H) = -\omega^2/(4\pi^2)\mathbf{D}_H \tag{3.7}$$

where equation 3.7 holds for all H.

If a single Laue point is excited, it is reasonable to assume that only two fields are dominant inside the crystal (the forward and deflected). If this assumption holds, equation 3.7 can then be reduced to a relatively simple quadratic equation

(see appendix B) .

$$\xi_0 \xi_H = \frac{1}{4} k^2 P^2 \psi_H \psi_{\bar{H}} \tag{3.8}$$

where:

$$\xi_0 \equiv (\mathbf{k}_0 \cdot \mathbf{k}_0)^{0.5} - k(1 + \frac{1}{2}\psi_0) \tag{3.9}$$

$$\xi_H \equiv (\mathbf{k}_H \cdot \mathbf{k}_H)^{0.5} - k(1 + \frac{1}{2}\psi_0) \tag{3.10}$$

where k is the wavevector of the incident light and P=1 for σ polarization and $P = \cos 2\theta$ for π polarization. Equation 3.8 is known as the dispersion surface.

The difference between the interior wave solutions and the incident wavevector (corrected for the average index of refraction) is $\xi_{0,H}$. $\xi_{0,H}$ can be represented as a function of incident x-ray angle (see appendix C):

$$\xi_0 = 0.5k|P||b|^{0.5}\Gamma[F_H F_{\overline{H}}]^{0.5}[\eta \pm (\eta^2 + \frac{b}{|b|^{0.5}})^{0.5}] \tag{3.11}$$

$$\xi_H = 0.5k|P|\frac{\Gamma}{|b|^{0.5}}[F_H F_{\overline{H}}]^{0.5}[\eta \pm (\eta^2 + \frac{b}{|b|^{0.5}})^{0.5}]^{-1} \tag{3.12}$$

where $b \equiv \frac{\gamma_0}{\gamma_H}$ ($b > 0$ Laue geometry, $b < 0$ Bragg Geometry), $\gamma_{0,H}$ represent the component of the incident and diffracted beam along the surface normal, and

$$\eta \equiv [b\Delta\theta \sin 2\theta + 0.5\Gamma F_0(1-b)]/\Gamma|P||b|^{0.5}\Gamma[F_H F_{\overline{H}}]^{0.5} \tag{3.13}$$

where θ represents the crystal angle, $\Gamma \equiv \frac{r_e \lambda^2}{\pi V}$, and $F_{0,H}$ is the structure factor for the forward and deflected waves. Physically η represents the angular deviation of the incident x-ray from the Bragg condition.

The structure factor represents the scattering power of the reflection. In a material with a periodic electron charge density, $\rho(r)$, the structure factor may be defined

as:

$$F_H = \int_V \rho_(r) e^{2\pi i \mathbf{G}\cdot r} dv \tag{3.14}$$

Assuming that the charge density can be represented as a small rigid sphere, the structure factor can be represented by a discrete sum:

$$F_H = \sum_n f_n e^{2\pi i \mathbf{G}\cdot r} \tag{3.15}$$

where f_n is the complex atomic scattering factor for the n^{th} lattice point. In the case of thermal vibrations the atomic scattering factor is modified by the Debye-Waller factor, $f_n \Rightarrow f_n e^{-M_n}$. Physically the structure factor represents the number of scattering electrons for a given reciprocal lattice vector, the larger the number of electrons the stronger the reflection. In a inversion symmetric crystal $F_H = F_{\overline{H}}$, however this is not generally the case.

The locus of points that satisfies equation 3.8 are represented by two hyperboloid sheets in reciprocal space called the dispersion surface (see figure 3.2). Since the crystal has a different average index of refraction than the vacuum, Snell's law dictates that the center point of the dispersion surface is not the vacuum Laue point ('L'). The magnitude of the shift is given by the average index inside the material. By convention, the sheet closest to the Laue point is called the α solution, while the other sheet is called the β solution. To determine the specific wave fields that propagate inside the crystal, the excited points of the dispersion surface must be known.

Figure 3.3 graphically demonstrates the method of determining the excited points on the dispersion surface. The vector $\overline{PO}$ represents the incident wave vector of

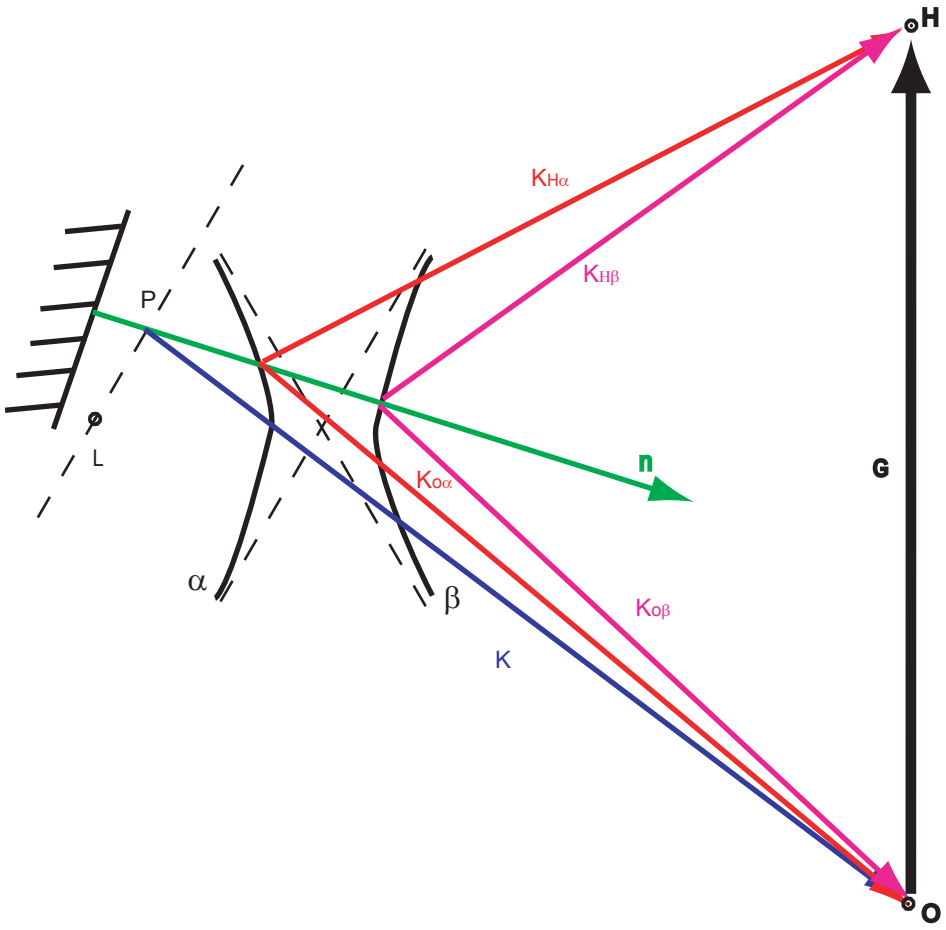

Figure 3.3: The X-ray dispersion surface in the Laue geometry

the x-rays and the value $|\overline{LP}|/k$ represents the angular deviation from the Bragg condition. A vector $\overline{n}$, defined as the crystal surface normal, is drawn through point P such that is slices through the dispersion surface. The excited points ('tie points') are the locations at which the vector $\overline{n}$ crosses the dispersion surfaces. The vectors connecting the tie points to the points O and H correspond to the allowed wavevectors for the two solutions, called α and β. These wavevectors will physically manifest themselves outside the crystal as a forward diffracted wave and deflected diffracted wave.

The α solution represents an x-ray standing wave in the transverse spatial direc-

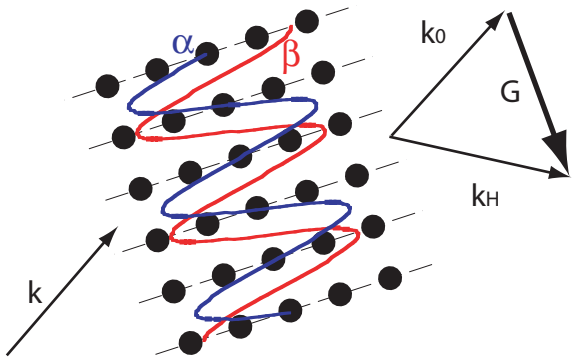

Figure 3.4: A graphical representation of the fields inside a crystal. The blue and red lines represent the α and β solutions respectively.

tion such that the nodes of the x-ray field lie on regions of high electron density (i.e. the lattice planes). The α solution does not experience much attenuation since the x-ray attenuation is dominated by photo-electric absorption. This solution represents x-ray anomalous transmission. The β solution is spatially phase shifted with respect to the α solution such that the anti-nodes lie on regions of high electron density (see figure 3.4). The β solution will be greatly attenuated and thus represents enhanced absorption. At the output of the crystal the α and β solutions spilt into the relevant ratio of the exterior solutions.

Along with the two exterior wave solutions, in the Laue geometry there exists a third transmitted beam (see figure 3.5). This beam corresponds to the 'real' transmission beam (a beam that is not deviated by the diffracting crystal). When the crystal is optically thick, the forward beam and the transmitted beam can be spatially separated.

The ratio of the exterior field amplitudes may be calculated after determining which tie points are excited . Using the definition of ξ and equation B.14 the following

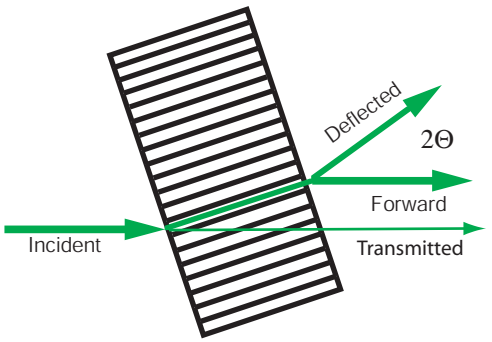

Figure 3.5: The flow of x-ray energy in a thick crystal.

relationship is derived:

$$\frac{E_H}{E_0} = \frac{-2\xi_0}{kP\psi_{\bar{H}}} = \frac{-kP\psi_H}{2\xi_H} \tag{3.16}$$

An analytic solution for the two propagating waves can be found by using equation 3.16 and implementing the relevant boundary conditions (see appendix C). In the Laue geometry ($b > 0$), the corresponding boundary condition is that all of the incident x-ray flux is in the forward direction:

$$\begin{aligned} E_0 &= E_{0\alpha} + E_{0\beta} \\ 0 &= E_{H\alpha} + E_{H\beta} \end{aligned}$$

where $E_{0\alpha}$,$E_{0\beta}$,$E_{H\alpha}$ and $E_{H\beta}$ are the incident and diffracted wave solutions in the α and β directions respectively. The resultant propagating solutions are:

$$E_{0\alpha} = CE_0 e^{-\nu} e^{-2\pi i((K'_{0\alpha}+iK''_{0\alpha})\cdot r)} \tag{3.17}$$

$$E_{H\alpha} = -CDE_0 e^{-2\pi i((K'_{H\alpha}+iK''_{H\alpha})\cdot r)} \tag{3.18}$$

$$E_{0\beta} = CE_0 e^{-\nu} e^{-2\pi i((K'_{0\beta}+K''_{0\beta})\cdot r)} \tag{3.19}$$

$$E_{H\beta} = CDE_0 e^{-2\pi i((K'_{H\beta}+iK''_{H\beta})\cdot r)} \tag{3.20}$$

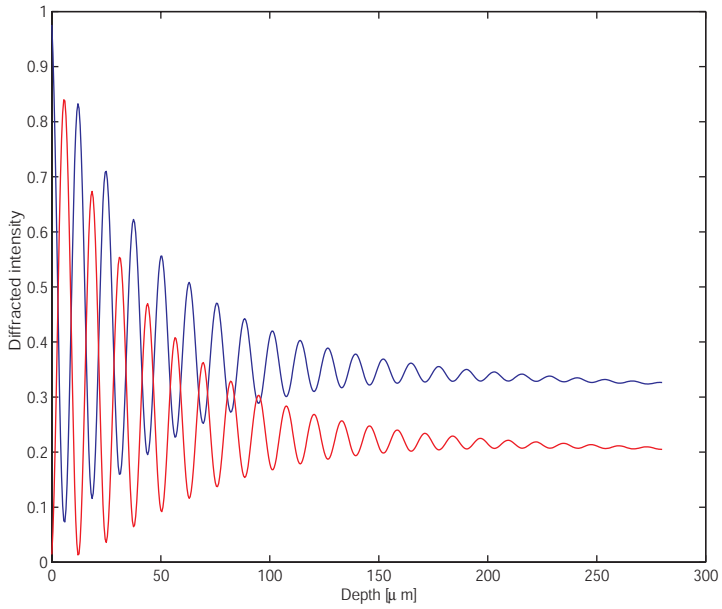

Figure 3.6: Diffraction efficiency of the forward (blue) and deflected (red) beams as a function of depth.

where:

$$C = \frac{e^{2\pi i v t}}{2\cosh\nu}$$
$$D = \frac{|P|}{P}|b|^{0.5}\frac{[F_H F_{\overline{H}}]^{0.5}}{F_H}$$

$K^{'}(K^{''})$ are the real (imaginary) components of the x-ray wavevector and $\sinh\nu \equiv \eta$.

3.1.2 The Pendellösung and Borrmann Effects

The intensity of a diffracted beam in the Laue geometry oscillates with a characteristic frequency as a crystal thickness changes (see figure 3.6). This is called the Pendellösung effect. The Pendellösung effect arises from the fact that the two solutions to x-ray dispersion surface (α, β) experience a slightly different index of refraction. As the crystal thickness increases, the phase accumulation between the α and β solutions changes causing a beating in both the transmitted and diffracted intensity. The characteristic beat frequency is directly related to the momentum

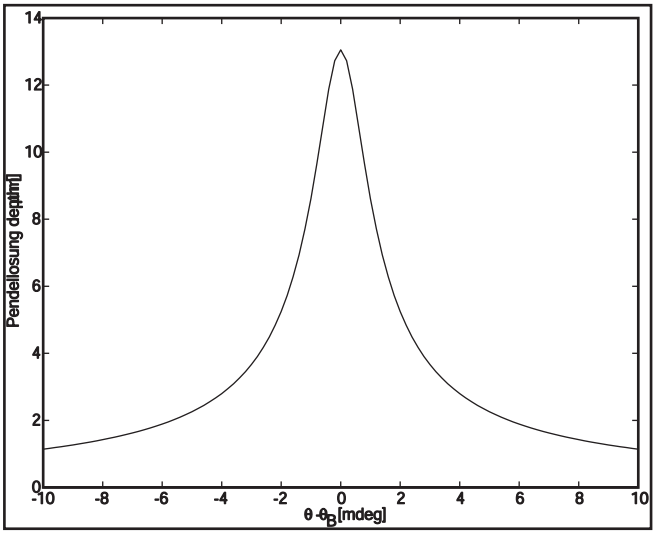

Figure 3.7: The Pendellösung depth as a function of crystal angle of the symmetric 220 reflection in Ge

difference of the two diffracted wave vectors, given by the inverse of the spacing between the tie points on the dispersion surface:

$$\Gamma = \frac{1}{\mathbf{K}_{0\alpha} - \mathbf{K}_{0\beta}} = \frac{\pi V \sqrt{\gamma_0 \gamma_H}}{r_e \lambda \sqrt{F_H F_{\overline{H}}} P \cosh \nu} \tag{3.21}$$

From equation 3.21 it is seen that the Pendellösung frequency changes as deviation from the Laue condition changes (see figure 3.7). The oscillations, however, decay rapidly as the crystal thickness grows (see figure 3.6). This decay is due to the enhanced absorption of the β branch. When the β branch has been completely absorbed, the oscillations cease, and only the diffracted x-rays from the α branch survive. This is x-ray anomalous transmission.

In figure 3.8 the field intensities of both the forward and deflected beams of the symmetric 220 reflection in a $280\,\mu m$ Ge [100] crystal are shown. As the crystal thickness is increased, the angular extent of the diffraction pattern shrinks due to absorption. The angular dependence of the x-ray anomalous transmission is given in

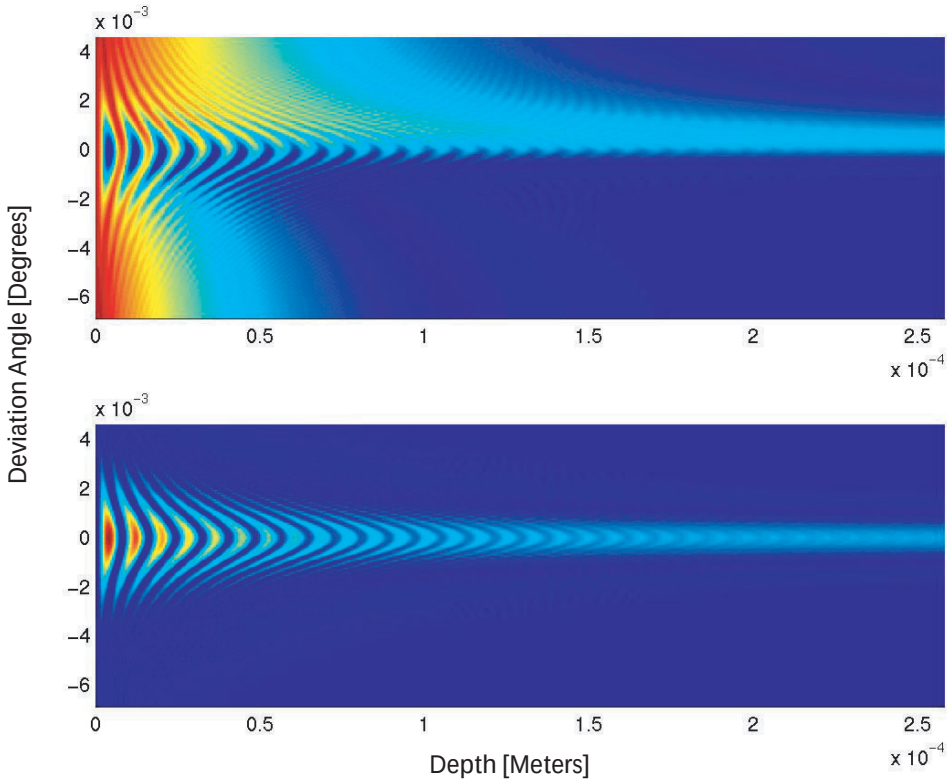

Figure 3.8: A two dimensional false color image of the calculated transmitted (top) and deflected (bottom) beams of a Ge [100] crystal as a function of diffraction angle and crystal depth.

the thick crystal case by[9, 50, 10]:

$$\frac{I}{I_0} = \frac{1}{4}\frac{1}{1+\eta^2} \tag{3.22}$$

For thick perfect crystals, the peak diffracted intensity is one quarter that of the input beam since one half of the input beam, the β solution, has been absorbed.

3.1.3 Bragg Geometry

In the Bragg geometry the interpretation of the x-ray dispersion surface changes slightly (see figure 3.9). This case it is possible to create an incident wavevector that does not cut through the dispersion surface. This physically means that a valid

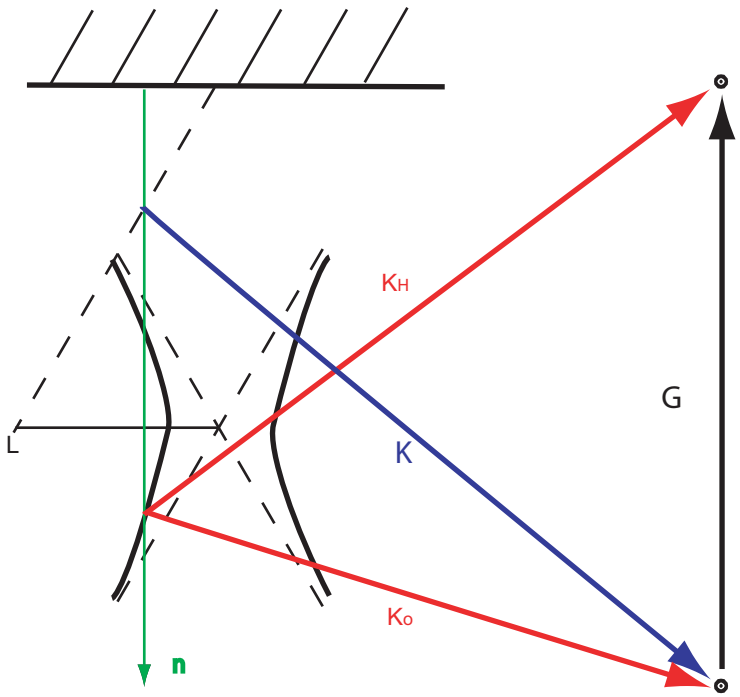

Figure 3.9: Dispersion surface in the Bragg geometry

interior wave solution does not exist and hence the x-rays do not propagate into the crystal. In the special case of zero absorption, these wavevectors will be completely reflected out of the crystal.

As the incident x-ray wavevector changes and starts to intersect the dispersion surface, the propagating wave solutions becomes a possibility. In general there are two excited tie points on the dispersion surface. One of the two tie points represents an interior wave solution that grows exponentially with distance. This is clearly not a physical solution leaving only one excited point on the dispersion surface[50]. The reflection coefficient in this regime is determined by using equation 3.16:

$$\left(\frac{E_H}{E_O}\right)^2 = \frac{\xi_O F_H}{\xi_H F_{\overline{H}}} = |b|(\eta \pm (\eta^2 - 1)^{.5})^2 \frac{F_H}{F_{\overline{H}}} \tag{3.23}$$

This is equivalent to the equation that Darwin determined for a perfect reflection (figure 3.10)[9]. The flattop response of the Bragg reflection is a consequence of the

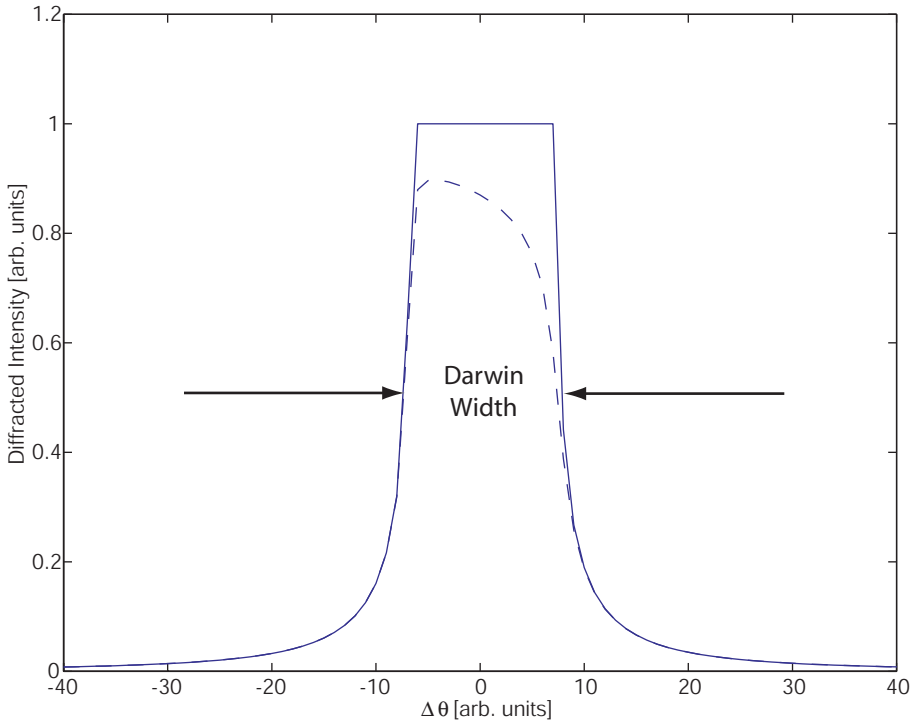

Figure 3.10: Darwin curve of Bragg reflection. (solid) no absorption, (dashed) absorption.

space between the dispersion surface and the lack of propagating wave solutions for those incident wavevectors. The full width half max of the Bragg curve is called the Darwin width (approximately equal to the spacing of the dispersion surface). In the real world, the incident x-rays experience attenuation. Since the α and β solutions experience different absorption coefficients, the diffraction pattern is slightly asymmetric.

3.2 Takagi-Taupin Equations

The analytical tools presented in the previous section are only valid in the special case of an unstrained perfect crystal. When a crystal has either defects or bulk strain, Maxwell's equations must be integrated numerically. The wave equation inside the

crystal is a second order differential equation making integration computationally intensive. Takagi[53, 54] and Taupin[55] independently simplified the second order equation into a set of two coupled first order equations in the case of small lattice strain.

As in the prior section, the Bloch solutions are propagated through Maxwell's equations. In the perfect crystal case, the phase term is relatively simple ($\sim \mathbf{k}_H \cdot \mathbf{r}$). The addition of a small lattice distortion changes this phase term:

$$\Phi_H = \mathbf{k} \cdot \mathbf{r} - \mathbf{G} \cdot \mathbf{u} \tag{3.24}$$

where $\mathbf{u}$ represents some local lattice distortion. If it is assumed that only two fields are present in the crystal and that the local distortions are not too large, an equation representing the displacement fields may be found. Keeping only the first order terms, the resultant coupled first order differential equations (see appendix D):

$$\frac{i\lambda}{\pi}\frac{\partial D_H}{\partial x_H} = \psi_0 D_H + \psi_H D_0 - \alpha_H D_H \tag{3.25}$$

$$\frac{i\lambda}{\pi}\frac{\partial D_0}{\partial x_0} = \psi_0 D_0 + \psi_H D_H \tag{3.26}$$

where

$$\begin{aligned} r &= x_0 s_0 + x_H s_H \\ s_0 &= \lambda K_0 \\ s_H &= \lambda K_H \\ \alpha_H &= 2(\Theta - \Theta_B)\sin(2\Theta_B) \\ \psi_0 &= -\frac{\lambda^2 r_e}{\pi V} F_0 \\ \psi_H &= -\frac{\lambda^2 r_e}{\pi V} F_H \end{aligned}$$

This set of equations is referred to as the Takagi-Taupin equations. In the special case of no strain, it has been shown that the Takagi-Taupin equations simplify to the x-ray dispersion surface [11].

In the Bragg geometry, the Takagi-Taupin equations can be simplified to a single first order differential equation. Defining the variable

$$X = \frac{D_H}{\sqrt{b} D_0} \tag{3.27}$$

Taupin[55] showed that the dynamical diffraction equations can be expressed as:

$$i\frac{dX}{dA} = (1+ik)X^2 - 2(y-ig)X + (1+ik) \tag{3.28}$$

where

$$\begin{aligned} A &= \frac{\pi |\psi_H^{'}| z}{\lambda \sqrt{|\gamma_0 \gamma_H|}} \\ \psi_{0,H} &= \psi_{0,H}^{'} + i\psi_{0,H}^{''} \\ z &= depth \\ g &= \frac{(1+b)\psi_0^{''}}{2|\psi_H^{'}|\sqrt{b}} \\ k &= \frac{\psi_H^{''}}{\psi_H^{'}} \\ y &= \frac{(1+b)\psi_0^{''} - b\alpha_H}{2|\psi_H^{'}|\sqrt{b}} \end{aligned}$$

This linear equation provides a method of quickly calculating the Bragg diffraction pattern as a function of crystal depth.

3.2.1 Strain Modelling

There are many different methods of computationally solving the Takagi-Taupin equations. One very elegant method is presented by Wie *et al* [56]. If the strain

is constant through one layer of thickness, $A - A_0$, equation 3.28 can be solved analytically. The scattering amplitude as a function of crystal depth is:

$$X(A) = \frac{sX_0 + i(B + CX_0)\tan s(A - A_0)}{s - i(C + BX_0)\tan s(A - A_0)} \tag{3.29}$$

where

$$\begin{aligned} X(A_0) &= X_0 \\ B &= -(1 + ik) \\ C &= y + ig \\ s &= \sqrt{C^2 - B^2} \end{aligned}$$

If the crystal substrate is a perfect unstrained crystal, X_0 becomes:

$$X_0 \equiv \frac{-B}{C - \sqrt{C^2 - B^2}} \tag{3.30}$$

This solution is mathematically equivalent to the Darwin equation with the addition of absorption (equation 3.23). Using equation 3.30 the diffracted intensity at any point in the thickness can be found.

Incorporating strain into this mathematical formalism is straight forward. Assuming the strain only changes the local Bragg condition the strain component can be introduced through the variable α_H[56, 57]. When a lattice is mildly strained this variable now becomes:

$$\alpha_H = -2(\Delta\theta_B - \eta \times \tan\theta_B)\sin 2\theta_B \tag{3.31}$$

Incorporating the modification into equation 3.29, the Bragg diffraction patterns of a perfect crystal with a strained surface layer can be calculated.

It is possible to calculate diffraction patterns for many types of strained crystals, including superlattices. The periodicity of the superlattice allows a recursion relation to be found such that the diffraction pattern due to the final layer is only dependent on the diffraction pattern in the preceding layers. The diffracted intensity due to the jth period of a 2 layer superlattice is given by [56]:

$$X_j = \frac{(P - iQ)X_{j-1} + (T - iR)}{(T + iR)X_{j-1} + (P - iQ)} \tag{3.32}$$

where

$$\begin{aligned} P &= (B_1B_2 - C_1C_1)\tan s_1A_1 \tan s_2A_2 + s_1s_2 \\ Q &= C_1s_2 \tan s_1A_1 + C_2s_1 \tan s_2A_2 \\ R &= B_2s_1 \tan s_2A_2 + B_1s_2 \tan s_1A_1 \\ T &= (B_1C_2 - B_2C_1)\tan s_1A_1 \tan s_2A_2 \end{aligned}$$

and $A_{1,2}$ are the thickness of the individual layers. Figure 3.11a shows the diffracted intensity as a function of angle (rocking curve) of a 200 layer superlattice.

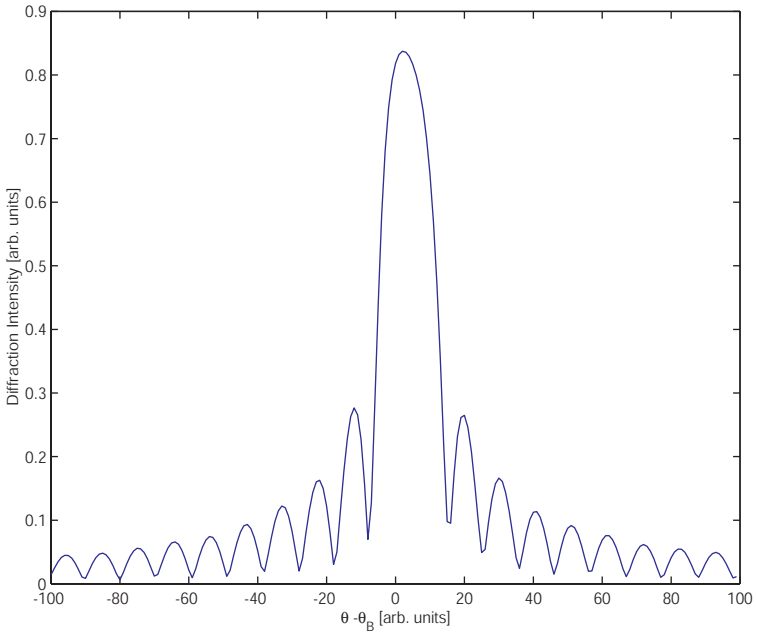

Figure 3.11: Bragg rocking curve due to a superlattice.

CHAPTER IV

Experimental Setup

The experiments described in this thesis were performed at the Michigan-Howard-Lucent Technologies Collaborative Access Team (MHATT-CAT) undulator beamline at the Advanced Photon Source (APS). Synchrotron sources, such as the APS, can provide very intense pulses of monochromatic x-rays which are necessary to measure lattice strain. The APS is comprised of 37 beamlines, with each beamline equipped with a bending magnet and an undulator (or wiggler) radiation source. The MHATT-CAT undulator beamline is comprised of four experiment hutches, each devoted to a specific type of experiment (see figure 4.1). In this thesis, experiments were performed in hutch 'D'.

4.1 The X-ray Source

Synchrotron sources produce radiation by the acceleration of charged particles. The generation and maintenance of these charged bunches (typically electrons) are the focus of many fields of physics and will be briefly touched upon here. A RF cathode produces a large number of electrons. These electrons are accelerated first by a linear accelerator to an energy of 200MeV and then by a booster ring to a final

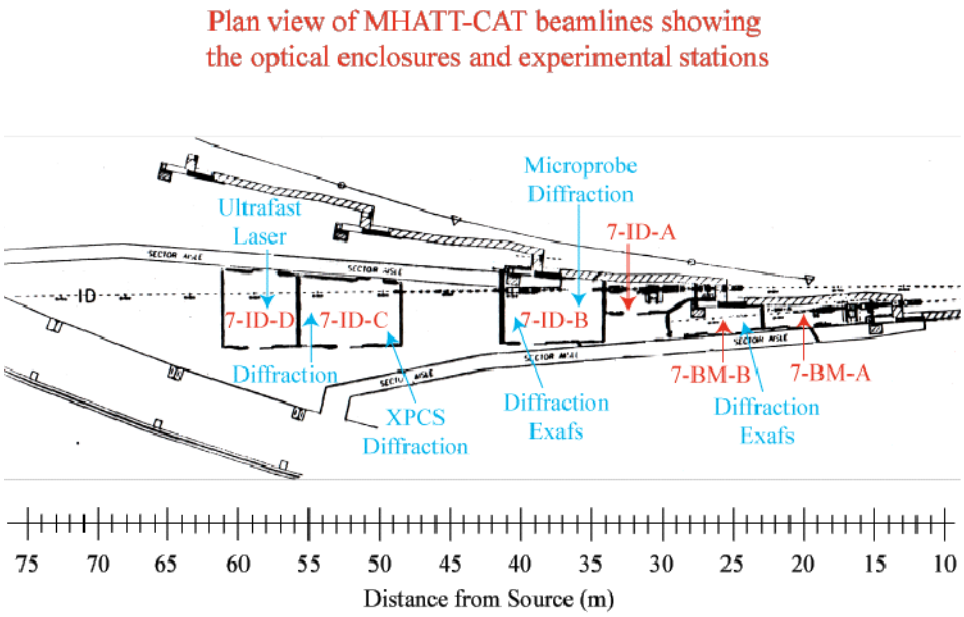

Figure 4.1: A schematic of the floorplan of the MHATT-CAT beamline. Image taken from www.mhatt.aps.anl.gov.

energy of 7GeV[58]. To maintain electron bunch structure in the storage ring, the bunches must be injected into the storage ring at a given frequency and phase with respect to the RF accelerating cavities. The structure of the x-ray bunch train is very important for time-resolved experiments.

4.1.1 Bunch Timing

To counter attenuation and dispersion of the electron beam, RF accelerating cavities compress and clean the spatial structure of each individual bunch while at the same time maintaining the temporal structure of the beam. The RF accelerating cavities run at a harmonic of the storage ring frequency ∼352MHz. For experiments that are sensitive to bunch timing, a signal is sent from the APS control room that is phase locked to the RF accelerating cavities. The timing jitter of this signal with respect to the electron bunch is ∼20ps.

Figure 4.2: An aerial photograph of the Advanced Photon Source. Image taken from www.aps.anl.gov.

Each trough of the RF cycle is called a bucket. During normal operations most buckets are not filled. The standard fill pattern is structured such that there are 22 individual electron bunches ('singlets') and a 'superbunch' made of 6 electron bunches each separated by a single bucket (see figure 4.3)(note: this superbunch has since been reduced to a singlet). Each electron bunch is separated by 52 buckets (or ∼150ns). At the end of the pulse train a gap of 300ns is incorporated to provide a method of counting individual revolutions of the storage ring. A signal which is locked to the superbunch ('P0'=272kHz) is relayed to the experiment hall so that time-resolved experiments may be synchronized to the revolution period of the synchrotron (see section 4.3.2).

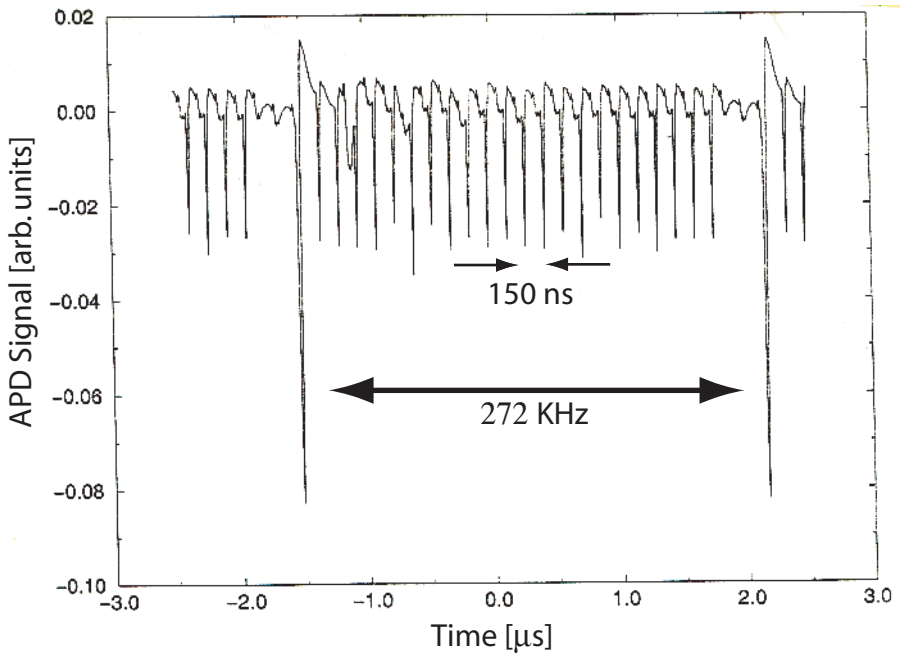

Figure 4.3: Synchrotron pulse train

4.1.2 Synchrotron Radiation

Synchrotron radiation is the classical electromagnetic effect of a charged particle emitting radiation upon changing direction. In these experiments an acceleration device called an undulator provides highly monochromatic x-rays. An undulator is made up of a set of permanent magnets spaced in a periodic array (figure 4.4). As an electron bunch travels through the periodic array, the bunch is accelerated by the static magnetic field. As the direction of the magnetic field is reversed, the electron bunches are accelerated in the opposite direction. If the periodicity of the array and the energy of the electron bunches are matched appropriately, the generated radiation will add coherently producing a very intense monochromatic x-ray beam.

Changing either the electron energy or the spacing of the magnets, the wavelength

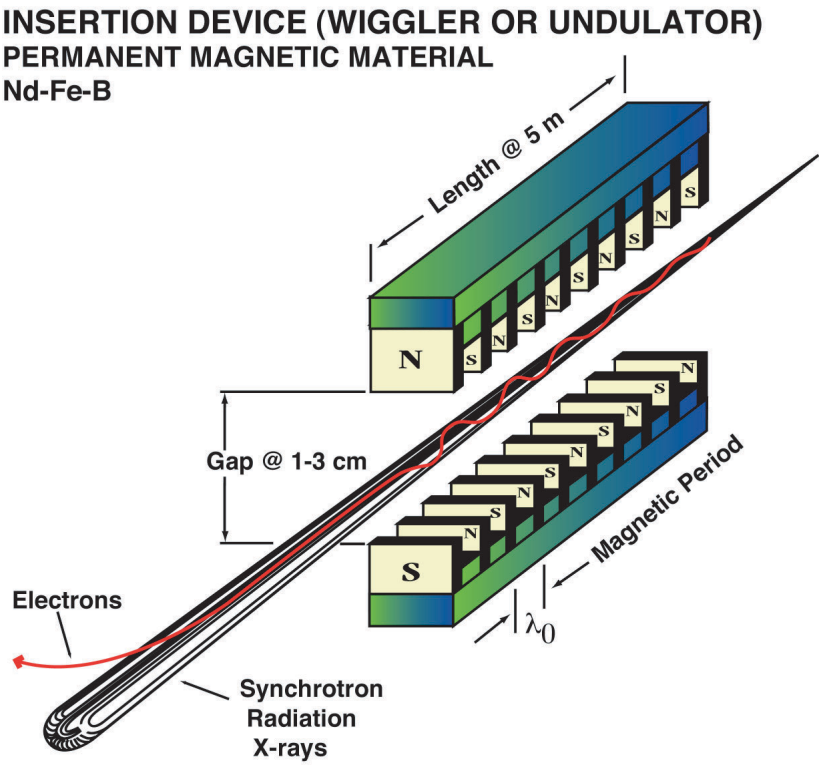

Figure 4.4: A representation of an undulator of the APS. Image taken from www.aps.anl.gov.

of the generated radiation will be modified.

$$\lambda_n = \frac{13.056\lambda_u[cm]}{E^2[GeV]n}(1 + K^2/2) \tag{4.1}$$

Where the deflection parameter, K, is:

$$K = 0.934\lambda_u[cm]B_0[T] \tag{4.2}$$

where λ_u is the periodicity of the undulator, B_0 is the magnetic field of the undulator, and E is the energy of the electron beam[59]. The efficiency of the undulator changes with energy of the radiation. Figure 4.5 shows the peak brilliance (intensity per angular divergence per 0.1%bandwidth) of the output of the undulator as a function of x-ray energy. The bandwidth of the generated radiation is determined by the number of poles in the undulator:

$$\frac{\delta\lambda}{\lambda} = \frac{1}{nN} \tag{4.3}$$

where n is the harmonic number. At the MHATT-CAT beamline the number of poles is 72. The natural pulse width of the x-rays is determined by the pulsewidth of the electron bunches, in this case ∼70ps[58]. The effective pulse length of the x-rays is stretched to ∼100ps since the 352MHz reference RF is locked to the output x-ray pulse to only ±20ps.

4.1.3 Beamline Layout

The x-ray pulses emitted from the undulator possess significant spatial divergence and spectral bandwidth. To measure strain accurately with x-ray diffraction, the incident x-rays should be very close to the plane-wave limit. To ensure the incident x-rays are monochromatic, the introduction of some simple x-ray optics is necessary.

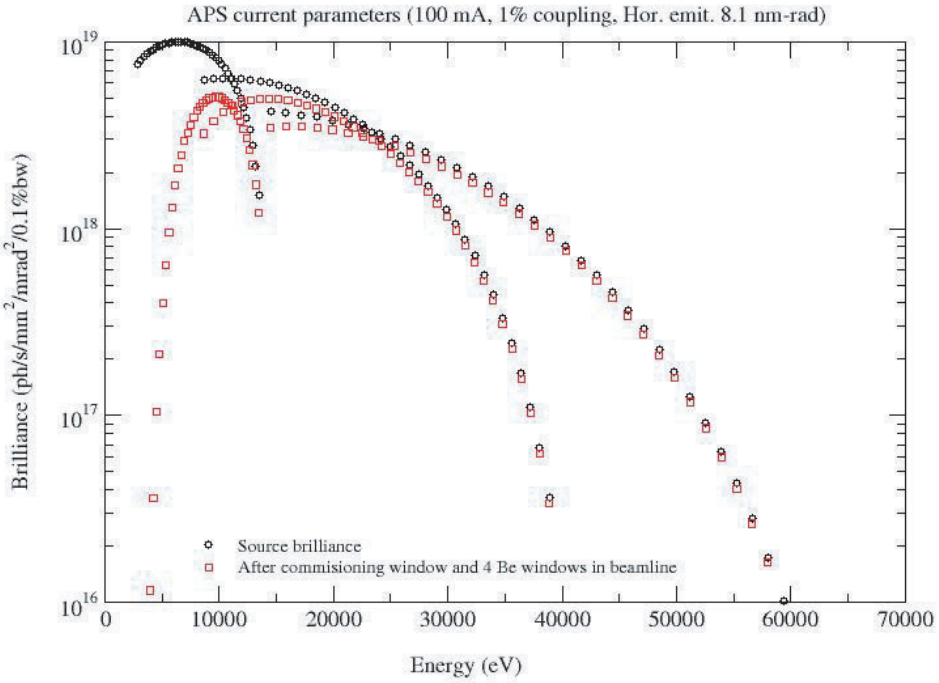

Figure 4.5: Intensity versus wavelength of the MHATT-CAT undulator beamline. Adapted from www.mhatt.aps.anl.gov.

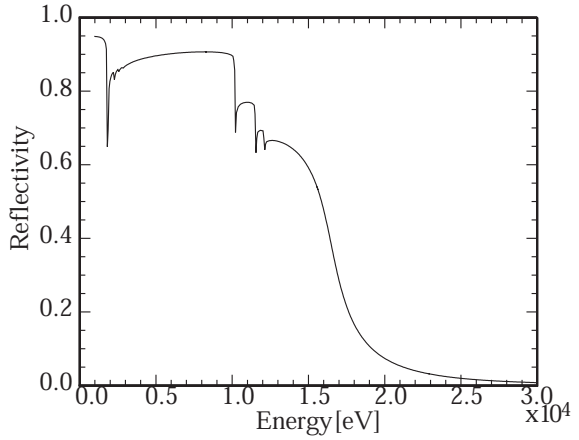

Figure 4.6: The x-ray reflectivity of a tungsten mirror. Adapted from www-cxro.lbl.gov

Immediately after the undulator a set of water cooled slits spatially restricts the beams to 400x400μm^2. This spatial restriction limits the spatial divergence and the spectral bandwidth. To clean the x-rays spectrally, a cryogenically cooled double crystal Si [111] x-ray monochrometer is used. The bandwidth exiting the monochrometer is limited by the width of the diffraction peak ($\sim$1.4 eV). At 10k eV, there are $\sim 10^{12}$ x-ray photons per second emitted to the experiment. To limit the attenuation a helium flight tube is used to transport the beam. Even using the helium flight tube, only about 5% of the 10keV photons survive to the experiment due to random air interfaces and imperfect flight tubes.

Diffraction conditions of the monochrometer do permit a significant amount of third harmonic of the undulator to propagate to the experiment ($\sim$ 10% of the fundamental). To remove the third harmonic a grazing incident tungsten mirror is used 30 meters downstream from the monochrometer. The reflectivity of the tungsten mirror reduces the third harmonic by a factor of 100 at a grazing angle of 0.28 degrees (figure 4.6). The mirror is also used to coarsely steer the x-ray beam.

Even with the water cooled slits there is still a significant amount of spatial divergence. The experiments are performed ∼55 meters from the source (see figure 4.1). At this distance the x-ray beam has diverged to 1x4mm^2. A second pair of slits is used to clean up the spatial divergence. The typical x-ray spot size at the crystal sample is ∼ .1x.2mm^2.

At the experiment, the target crystal is supported by a 4 circle goniometer. The goniometer allows full control of the angular orientation of the crystal as well as control of the angular position of the detector with up to 0.2mdeg resolution.

4.2 Detectors

Ultrafast time-resolved diffraction measurements require x-ray detectors that can differentiate between individual x-ray bunches emitted by the synchrotron. Non-invasive slow detectors are also useful in measuring average x-ray flux. There are several x-ray detectors that are used in x-ray scattering experiments. In the experiments described here only three methods are implemented.

4.2.1 Ionization Chamber

Ionization chambers are perhaps the easiest tools to measure average x-ray flux. As x-rays propagate through a gaseous medium, the photon energy may be great enough to ionize the surrounding gas. Two metal plates, held at a constant high voltage, surround the path of the x-ray beam. As the x-rays ionize the gas, the emitted charged particles are pulled to the metal plates causing a current to propagate in the charging lines. This current is measured by a high gain ammeter, the output of which is directly proportional to the intensity of the x-ray beam.

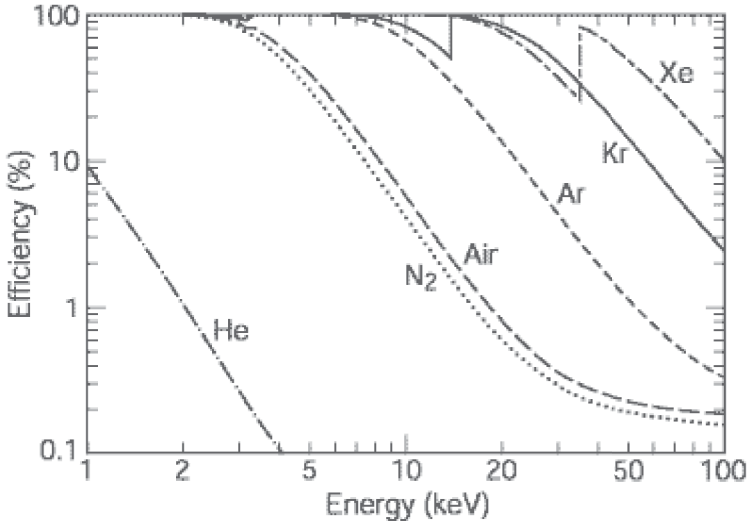

Figure 4.7: Efficiency of a 10-cm long gas ionization chamber for different gasses at normal pressure. Adapted from [59].

Calibrating the intensity of the beam is straightforward if the ionizing gas and the geometry of the charged plates is known. Figure 4.7 shows the ion chamber efficiency as a function of x-ray energy for some typical buffer gases and assuming the plates are 10cm long.

4.2.2 APD

To temporally resolve the emitted bunch pattern a silicon Avalanche Photodiode (APD) is used. The basic functionality of the APD is very similar (if not identical) to a regular optical photodiode[60]. X-rays that illuminate a biased piece of silicon, cause bound electrons to be promoted from the valance band to the conduction band. These highly energetic electrons continually excite other valance band electrons causing a cascade effect to occur. The cascaded electrons are then detected as a time-resolved current.

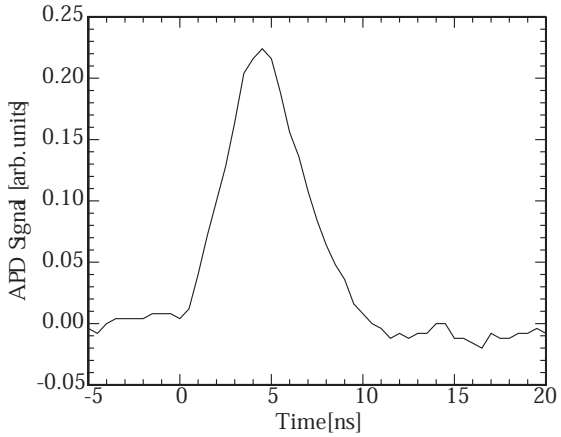

Figure 4.8: Temporal response of the APD.

The advantages of this device are three fold: the efficiency, gain, and speed. If the silicon is thick, the quantum efficiency of the APD will be close to unity. The inherent gain of the system can be many orders of magnitude depending on the bias voltage. But the most important trait of the APD (at least for these experiments) is the rise time of the detector is on order of 3-5ns (figure 4.8). This rise time is fast enough to temporally resolve the singlet spacing of the emitted x-ray bunches (figure 4.3). The detector is then gated to measure the average intensity of any given x-ray bunch.

Although the APD has substantial gain, to detect small changes in x-ray intensity external amplifiers are needed. These amplifiers have two requirements; high gain and speed. The amplifier must be fast enough that single x-ray bunches separated by 150ns can be individually gated. 40MHz (or faster) amplifiers accomplish this task adequately. After amplification it is possible that a single x-ray photon will register as a single volt at 50 ohms impedance.

Although APD's can distinguish between individual bunches emitted from a syn-

chrotron, the time-resolution is still limited by the x-ray pulse width. To measure dynamics on the picosecond time scale using synchrotron radiation, it is necessary to measure the x-ray pulse shape as a function of time. One device for performing this task is an x-ray streak camera.

4.2.3 Streak Camera

X-ray streak camera uses the generation of electrons of an x-ray photocathode to measure the time-intensity distribution of the x-ray pulse [61, 62, 30]. The photocathode (typically CsI) generates a large number of primary electrons upon x-ray excitation (typical efficiencies $\sim$10% [63, 64]). The primary electrons cause a cascade of secondary electrons (energy spread $\sim$1.5eV) to be emitted which are accelerated towards the anode.

As the electrons are accelerated, they enter a region surrounded by two field plates. During non-streaking operation, these plates are held at a constant voltage causing the electron beam to be perturbed. During the streak mode, the bias on these plates changes over time such that electrons emitted at different times experience a different field. This causes the electron beam to spatially spread along one spatial axis. The amount of spatial dispersion depends on the x-ray pulse length and the speed of the bias switch. The trigger for this sweeping voltage is generated by a photoconductive switch turned on by the ultrafast laser. The advantage of the photoconductive switch is that the voltage pulse is locked to the laser which generates the time-dependent fluctuation in the x-ray beam.

The streaked electron beam strikes a multichannel plate causing a cascade of

electrons. This cascade irradiates a phosphor screen causing the exposed area to emit visible light. Since the electron beam has been spatially dispersed, the light that is emitted follows the electron beam and thus appear to be a streak. The light is collected using a CCD array.

To calibrate the time dependence of the streak, an ultrafast ultraviolet (uv) pulse is used to generated the electrons on the photocathode. As the uv pulse is optically delayed with respect to the photoconductive switch, the generated electron pulse will change with the phase of the voltage pulse. By mapping the position of the electron bunch as a function of delay, a correlation between CCD pixel number and time delay is achieved (see figure 4.9). The increase of the streak voltage changes the sweep speed, effectively changing the streak camera resolution. Streak cameras have been demonstrated to have time resolutions of 0.5ps and 3ps using the single shot and averaged modes respectively[30]. In the setup used in these experiments the time resolution $\sim$5ps.

4.3 Ultrafast Laser system

The generation of large coherent strains on a picosecond timescale requires a laser system that is capable of producing pulse widths shorter than the product of optical penetration depth and the speed of sound. To generate large strains ($> 10^{-3}$), optical fluences in excess of 10 $\frac{mJ}{cm^2}$ are desirable (see chapter 2.2). Commercial laser systems are now available which provide stable high power ultrafast optical pulses. The general layout of the laser system is well known[65], and it will be discussed briefly in section 4.3.

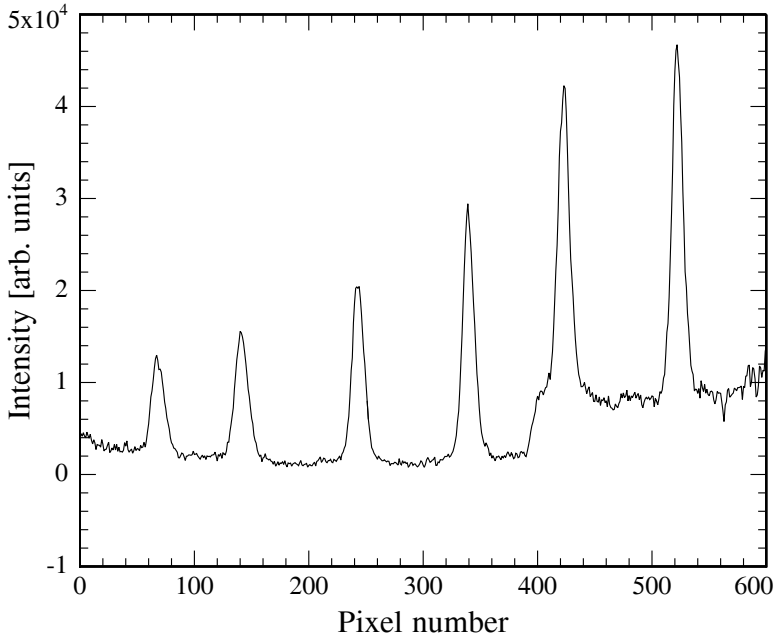

Figure 4.9: Streak camera data of 6 uv pulses separated by 30ps

4.3.1 Ti:sapphire oscillator

A short pulse is required to create very high peak intensities. To generate the shortest pulse, the phases of all of the cavity modes must be locked with respect to each other, i.e. modelocked. To induce modelocked operation in a laser cavity, typically a loss mechanism is introduced into the cavity such that only optical light with high peak powers is chosen. The mechanisms are distributed into two distinct classes, active and passive. Passive modelocking (the method that is presented here) uses the components permanently installed in the laser cavity to induce pulsed operation. Nonlinear effects in the gain medium is the passive component which induces modelocking for these experiments. The general optical layout is shown in figure 4.10.

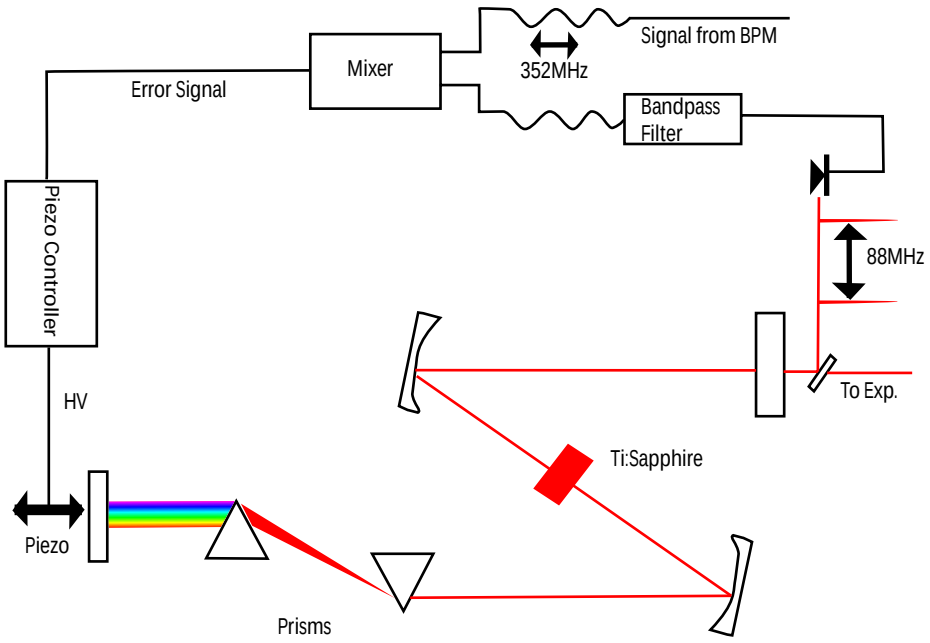

Figure 4.10: A schematic for the laser oscillator

Titanium doped Sapphire (Ti:sapphire) modelocked oscillators have become the standard for producing ultrashort and ultra stable optical pulses. The large gain profile of the Ti:sapphire (greater than 300nm) makes it possible to generate sub-100fs optical pulses using a relatively simple design[65]. The optical non-linearity used in the Ti:Saphire oscillator is called the Kerr-Lens effect. Ti:sapphire has a refractive index that changes with optical intensity ($n = n_0 + n_2 I$). If this optical light is focused into a crystal, the intensity of the light may change in the index enough such that the effective focal length in the crystal changes causing continuous wave operation to be unstable. A pair of prisms are introduced to compensate for the dispersion inside the cavity. If the intra-cavity intensity is large enough, self-focusing may occur allowing higher peak intensities to see a stable cavity. Thus the cavity itself selects short pulsed operation over CW operation.

The Ti:sapph oscillator that is used in these experiments is a Kapteyn-Murnane

Labs oscillator pumped by a cw diode laser. To insure that the output of oscillator is phase locked to the x-ray pulse train, the cavity has been modified slightly to allow locking to a reference RF source which is locked to the accelerator cavities of the synchrotron. Because of spatial constraints, the pulsing frequency of the optical oscillator is set to the fourth sub-harmonic of the RF reference, 88MHz.

To control the pulsing frequency the cavity length must be adjusted with very high precision. To achieve this high precision, active feedback is used to control the cavity length. The back mirror is mounted on a small piezoelectric crystal. This piezo changes the cavity length (and thus the oscillator frequency) when a voltage is applied. At the output of the oscillator a fast photodiode samples the pulsing frequency (see figure 4.10). The output of the photodiode is sent to a 352MHz bandpass filter and then mixed with the reference RF. The mixer creates a DC error signal which represents the phase difference between the RF reference and the oscillator. The error signal sent to a feedback loop which adjusts the voltage on the piezo in the attempt to zero the error signal. If the piezo does not have the dynamic range to compensate for the phase error, a mechanical stepper motor can make macroscopic changes to the cavity length to get within the piezo's dynamic range. The feedback loop has sufficient bandwidth to lock the oscillator to the RF to better than 20 ps and can respond to exterior noise sources up to 1kHz.

4.3.2 Chirped Pulse Amplification

Modelocked oscillators produce optical pulses with energies $\sim 5nJ$. To generate large amplitude lattice vibrations fluences of greater than $10\,\frac{mJ}{cm^2}$ are need, which

not practically possible with the output of the oscillator alone. Using a method optical amplification method called chirped pulse amplification (CPA) [66, 65], these ultrafast optical pulses may be amplified the several orders of magnitude needed to generate very large lattice strains.

CPA has become the standard method of generating high power ultrashort pulses. A general diagram of the CPA setup is given in figure 4.11. The trick to CPA is to make a short pulse into a long pulse, thereby reducing the peak intensity. Transmitting a transform limited pulse through a dispersive medium, will cause the different fourier components (i.e. colors) to travel at different velocities thus 'stretching' or 'chirping' the pulse. Using a grating stretcher, the optical pulse can be chirped in a controlled fashion, such that colors will come out of the stretcher with a definitive phase relationship. At the output of the stretcher, the once 50fs optical pulse is stretched to $\sim$25ps reducing the peak intensity by almost 3 orders of magnitude.

To generate the milliJoule pulse energies that are required, a laser is needed which can supply at least that amount of energy to the amplifier crystal. A 1kHz Q-switched Nd:YLF laser is used to provide 12 W of power to the amplifier crystal. The repetition rate is in contrast to the 88MHz pulse rate of the modelocked oscillator. To match the pump rate, the 88MHz pulse train is reduced to 1kHz without destroying the spectral components of the optical pulse. The most common method is to use a Pockels' cell. A SRS535 digital delay generator controls the Pockels' cell firing sequence as well as the firing time of the Nd:YLF laser.

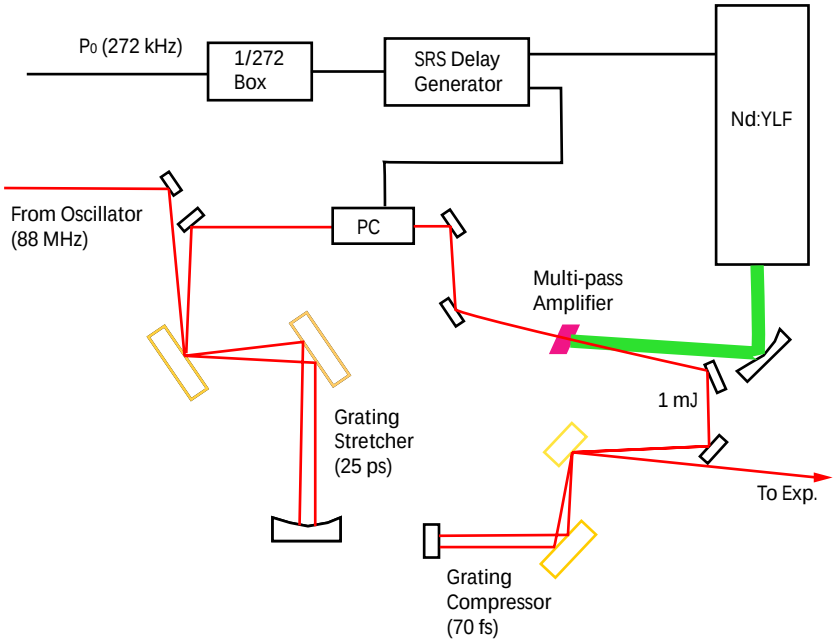

Figure 4.11: A general schematic for the ultrafast optical pulse amplifier.

After a particular pulse has been selected, the chirped pulse is directed into an 8 pass amplifier. After 8 passes, the optical pulse energy has increased ∼60dB while still maintaining a 25ps pulse width. To reconstruct the short pulse, the fourier components of the optical pulse must be 'unchirped', that is all of the fourier components will possess a relative phase such that a transform limited pulse is created. This is accomplished in a grating compressor. The final compressed and amplified pulse is ∼70fs, ∼0.5mJ. With minimal focusing the fluence can easily exceed 100 $\frac{mJ}{cm^2}$ meeting the requirements to generate large coherent lattice vibrations.

4.4 Laser/X-ray Timing

Insuring that the ultrafast laser pulse and x-ray pulse arrive at a given time delay is imperative in performing time-resolved diffraction studies of laser driven processes. Using some digital electronics and the APD, the laser and x-ray pulse

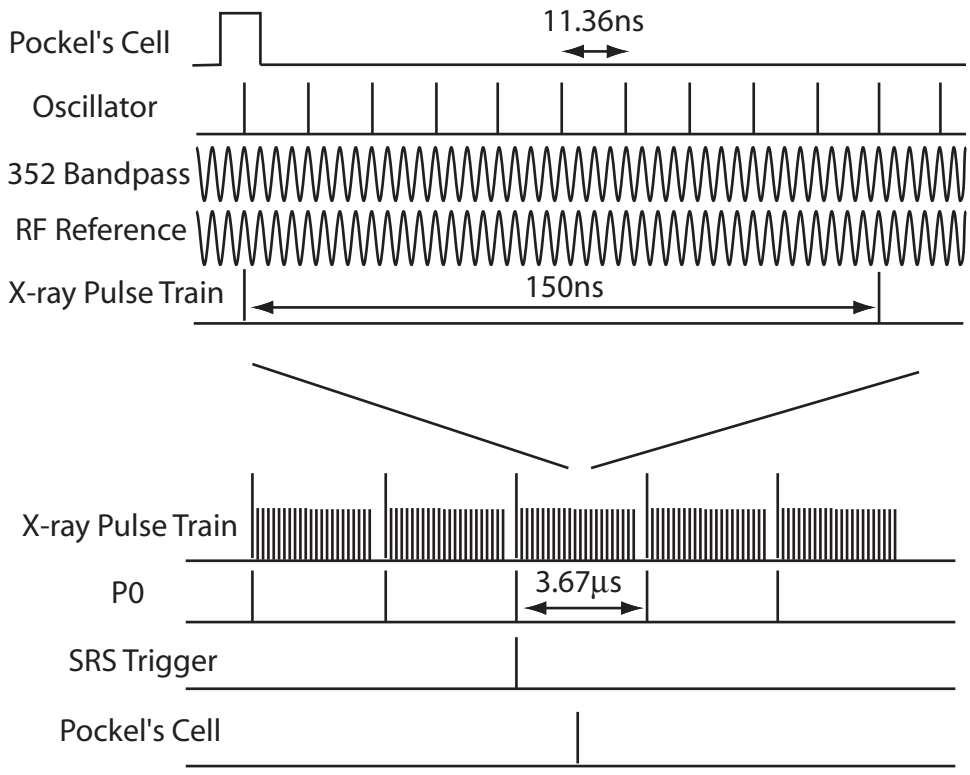

Figure 4.12: Flow diagram of the Pump-probe setup

can be engineered to arrive at the correct phase (figure 4.12). The APD is very sensitive to optical light, so the APD can detect the optical light and the x-ray source simultaneously. This gives a method of detecting the relative time delay between a specific x-ray pulse and the ultrafast laser. It is very unlikely that the relative time delay between the x-ray and laser pulse is completely matched. The ability to manually adjust the delay is necessary in the pump-probe geometry. Changing the relative time delay is implemented by using a simple digital phase shifter.

By slowly adding phase to the reference RF, the relative delay of the laser and the x-ray source can be controlled. The feedback loop recognizes that the phase is not correct and adjusts the laser cavity accordingly. This in effect will change the relative timing between the optical pulse and the x-ray pulse by the amount of phase

that was added to the reference RF. The resolution of the phase shifter is limited to 19ps, while not great, is well within the effective x-ray pulse length. The maximum delay that the phase shifter can impart is 4.75ns.

This method of pulse delaying, while effective in the study of relatively short phenomena, does not allow the continuous following of long lived crystalline strains. To study the evolution of picosecond crystalline strains requires picosecond precision through many microseconds of delay. Traditional optical scattering experiments would require kilometers of optical paths to achieve microsecond delays, which in most circumstances is impractical. However, these experiments utilize two independent light sources for the pump-probe geometry. Digital electronics can be used to adjust the relative locations of the x-ray and laser pulses.

A SRS535 digital delay generator will generate an arbitrary delay line for the optical pulse. This delay box controls when the amplifier is fired and oscillator pulse is amplified. When used in conjunction with the digital phase shifter, delays of -1ms to 1ms are achievable with 19ps resolution. By following a specific x-ray pulse with the boxcar integrator an $\sim$80dB dynamic range of the timing delay is possible.

CHAPTER V

Time-Resolved X-ray Bragg Diffraction

The study of picosecond ultrasonics has been well documented using optical scattering techniques [1, 2, 3]. These optical techniques, however, can only provide frequency and relative phase information about acoustic pulses. Time-resolved x-ray Bragg diffraction can measure the amplitude and frequency spectra of the acoustic pulse simultaneously.

A phonon, of wavevector $\pm q$, will generate sidebands on a Bragg rocking curve. The positions of the sidebands are determined by momentum conservation: $\mathbf{k} + \mathbf{G} \pm q = \mathbf{k}_H$ (see figure 5.1). Bragg's law implies that the generated phonon wavevector determines the location of the diffraction sidebands.

$$q = \Delta\theta |\mathbf{G}| \tan\theta_B \tag{5.1}$$

To resolve small phonon wavevectors ($\sim 1\mu m^{-1}$), Bragg rocking curves must have an angular extent very close to the Darwin width. Crystals with diamond or zinc blende structure (e.g. Ge, GaAs, or InSb) can be grown with very few crystalline defects so that the experimental x-ray rocking curves are limited only by the x-ray bandwidth.

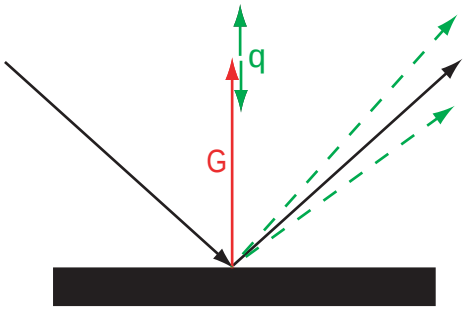

Figure 5.1: Wavevector matching in the Bragg geometry.

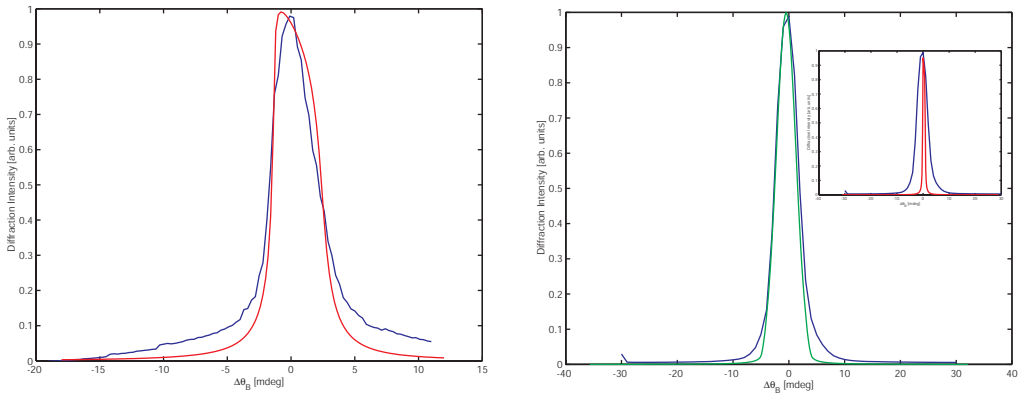

Figure 5.2: (a) Rocking curves of the symmetric 111 Bragg reflection in InSb. Data (blue curve) taken with an ion chamber and calculation (red curve) by integration of the Takagi-Taupin equations. (b) Rocking curves of the 400 symmetric Bragg reflection in Ge. Data (blue) Takagi-Taupin with an added angle convolution (Green). Inset: Data (blue) pure Takagi-Taupin (red).

X-ray rocking curves of an unstrained 111 InSb crystal measured at the MHATT-CAT undulator beamline are very close to the Darwin width (see figure 5.2). The 004 reflection in Ge is much narrower than the InSb reflection, implying that the angular resolution of this reflection is limited by the x-ray bandwidth (10keV±1.4eV). The calculated Darwin curve convolved with the x-ray bandwidth correctly predicts the observed diffraction patterns. The small wings apparent on both the experimental rocking curves correspond to either the static strain induced from the mounting of the crystal and/or the non-gaussian spectral profile of the x-rays.

5.1 Time-Resolved X-ray rocking curves

To generate an ultrafast strain pulse with a large wavevector, an ultrafast light source is needed to illuminate a material with a small penetration depth. In these experiments, an 840 nm 70 fs laser pulse illuminates a 111 InSb or a 001 Ge single crystal. The optical penetration depth (η) for 840 nm light is ∼100nm and ∼220nm for InSb and Ge respectively. This very shallow penetration depth allows the generation of large surface strains with a peak acoustic wavevector of $\sim \frac{1}{\eta}$. The x-rays are able to sample the laser induced strain directly in these two systems since the x-ray extinction depth ($\sim 1\,\mu m$) is significantly larger than the optical penetration depth.

InSb is an ideal crystal to begin the study of acoustic phonon generation due to its small optical penetration depth and relatively slow sound speed (∼3400m/s in the 111 direction). Upon laser excitation (fluence $\sim 10\,\frac{mJ}{cm^2}$), a significant fraction of the incident laser energy is absorbed in the crystal causing an increase in the average surface temperature. The laser fluence is not enough to cause surface melting, though over many repeated heatings surface scarring is visible. This scarring did not affect the x-ray diffraction patterns indicating that damage was only on the surface. Spectroscopic data indicate that the repeated heating causes a simple oxidation on the crystal surface, which leads to the observed surface scarring.

The rise in surface temperature causes the average spacing of the crystal lattice to increase. Since the location of the diffraction peak is directly related to the lattice spacing, the laser heating will shift the diffraction pattern (figure 5.3). Using the Bragg equation, the lattice parameter is inferred to have expanded by ∼0.007%

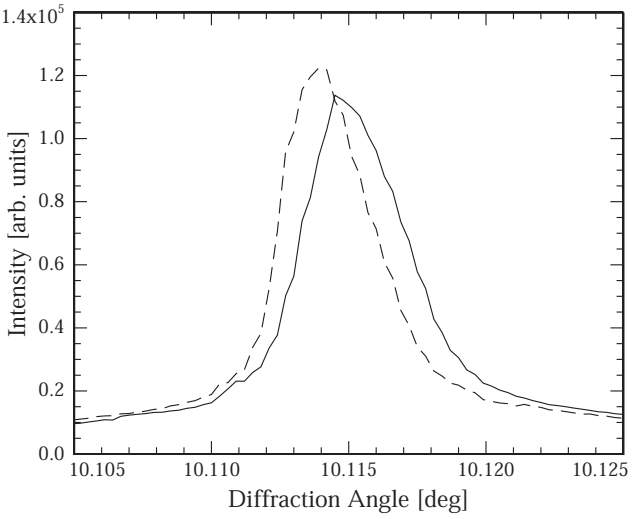

Figure 5.3: Rocking curve of the heated (dashed) and the unstrained 111 symmetric reflection in InSb measured with an ionization chamber.

($\sim$0.26mÅ). Assuming a linear expansion coefficient of $4.7\times10^{-6}K^{-1}$ [67], the crystal temperature increases by $\sim 15°$K upon laser exposure.

Although this temperature rise is approximately constant, the strain is significantly larger at the time of laser excitation. The time dependence of the strain is measured using a 'fast' avalanche photodiode (APD). The plotted signal of the APD and the ionization chamber (which samples every x-ray pulse) is slightly different due to photon counting statistics and electronic noise (figure 5.4). Sidebands on either side of the diffraction peak are visible 100 ps after laser excitation (figure 5.5).

In the limit of kinematic diffraction, the existence of sidebands on the diffraction peak indicates that there are three regions inside the crystal; unstrained, compression (positive sidebands), and rarefaction (negative sidebands). In less than 1ns the shape of the diffraction pattern has almost returned to normal, though the diffraction peak has shifted $\sim$3mdeg indicating a transient strain has propagated out of the detecting region leaving a residual heated layer at the surface. Assuming a linear expansion

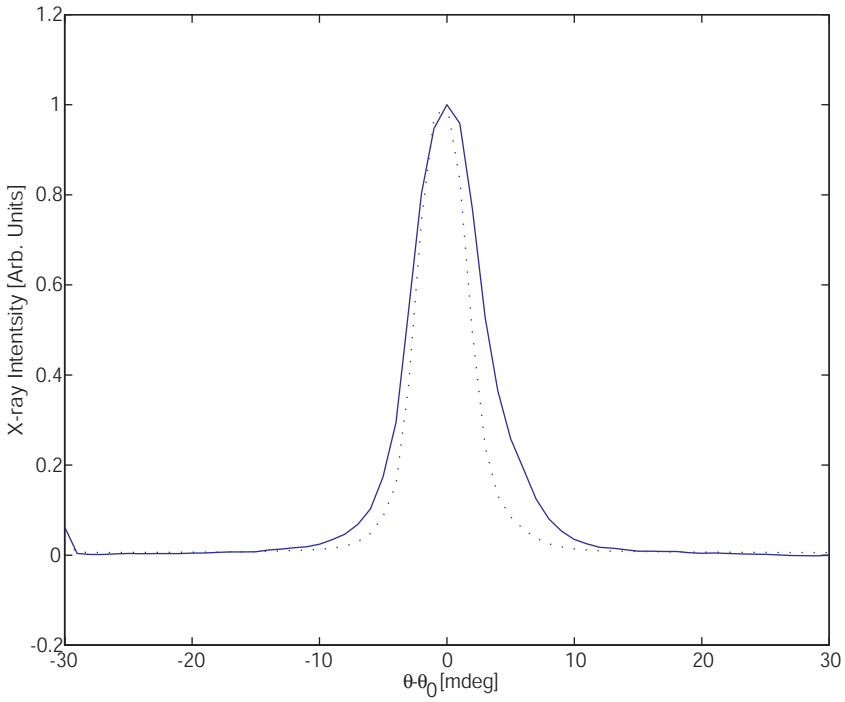

Figure 5.4: Angular response of the APD (solid) and Ionization chamber (dashed).

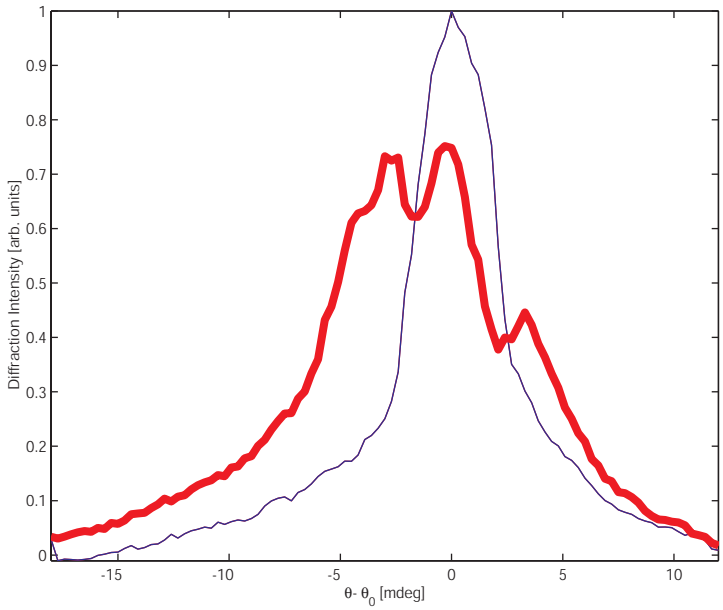

Figure 5.5: The diffraction patterns of the 111 InSb at time delays of -100ps and 100 ps

coefficient of $4.7 \times 10^{-6} K^{-1}$, the static thermal layer at the crystal surface has risen at least $\sim 60°$K.

By measuring individual rocking curves at different relative time delays, a time-resolved picture of the strain begins to develop (figure 5.6). At zero time delay sidebands are immediately apparent on the main Bragg peak. The positive sidebands only remain for ∼400ps indicating the compression layer only exists within the x-ray extinction depth for that amount of time. Oscillations on the rarefaction sidebands, however, are apparent for ∼500ps and show time-dependent oscillations. At each discrete angle a Fourier transform of the time axis is preformed (figure 5.6b). This demonstrates that as the crystal angle deviates from the Bragg condition the central frequency of the oscillations changes linearly. Since the deviation from the Bragg condition is a measurement of phonon momentum, the time-resolved x-ray diffraction is a graphical representation of the the acoustic dispersion relation, $\omega = ck$.

Data taken with the symmetric 004 reflection in single crystal Ge shows qualitatively similar features to the InSb data(figure 5.7). There are two distinct differences from the InSb and the Ge cases. The most apparent difference is the global increase in diffraction efficiency at positive time delays. This is due to the small Darwin width of the Ge reflection. By distorting the crystal, the x-ray reflectivity rises due to the increased coupling of the finite x-ray bandwidth. The second difference is the lack of time dependent modulations on either side of the diffraction peak. This is due to the faster sound speed (∼4800m/s) and the larger Bragg angle which makes the time-dependent oscillations faster than the x-ray pulse width.

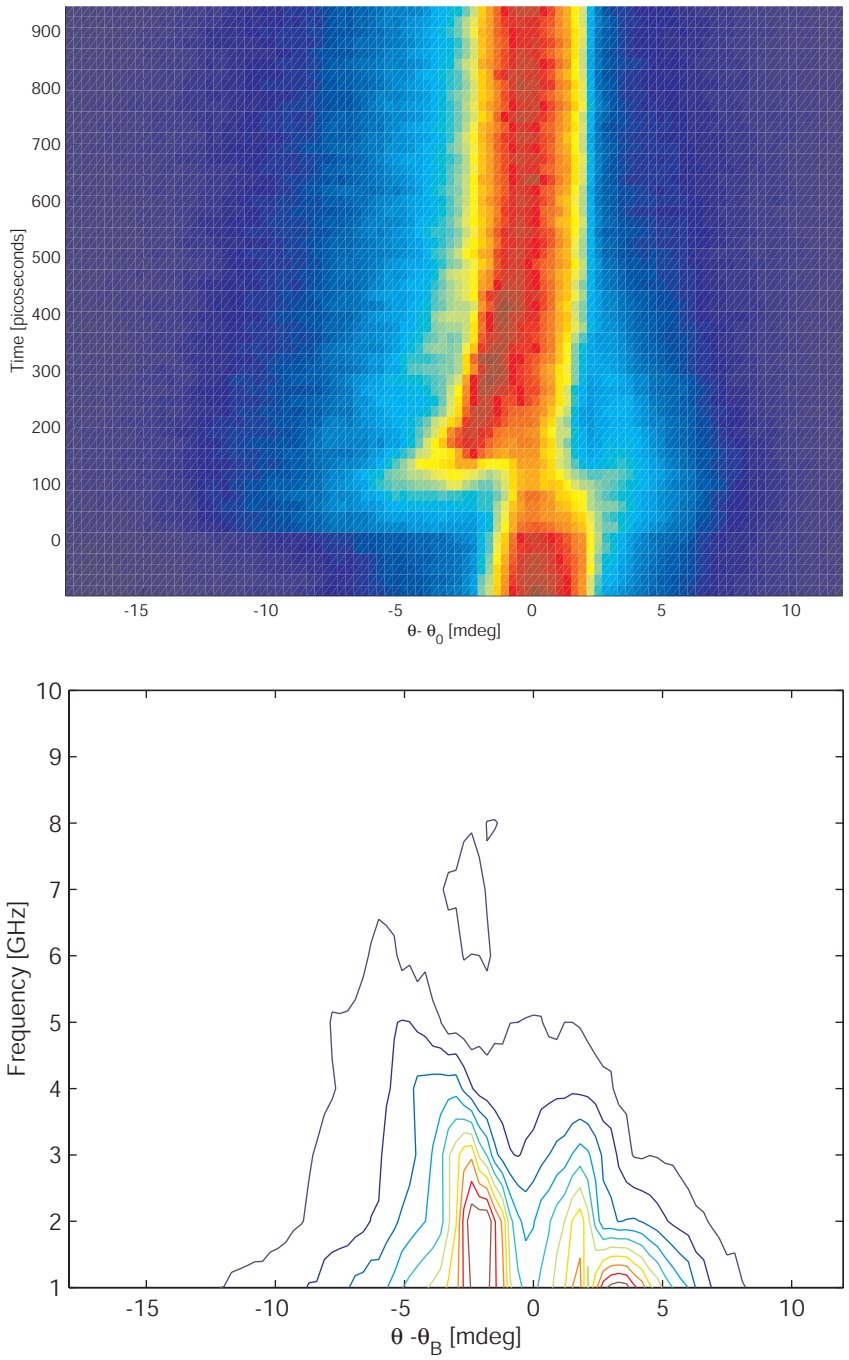

Figure 5.6: (a)Time-Resolved Bragg diffraction curves of the symmetric 111 reflection in laser strained InSb. Adapted from [68] (b) Fourier transform of the Time-Resolved Bragg Diffraction. The solid line has been added for emphasis.

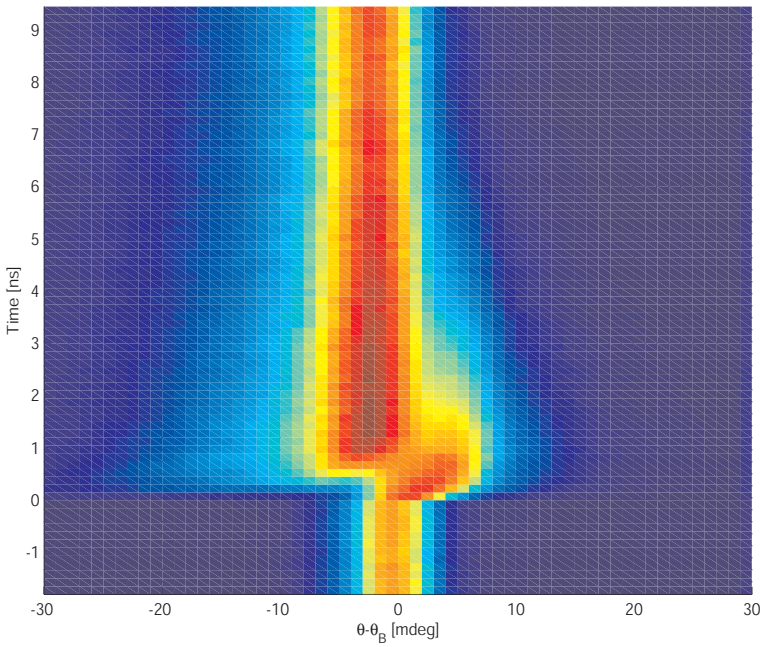

Figure 5.7: Time-Resolved Bragg diffraction curves of the symmetric 400 reflection in laser strained Ge.

5.2 Comparison: Experiment vs. Theory

To simulate these data, we assume that the generated strain is governed by the Thomsen model (see section 2.2) and that the incident optical radiation does not permanently change the diffraction patterns. We have simulated the diffraction patterns using the Thomsen model in conjunction with dynamical diffraction theory (the MATLAB code is shown in appendix E). To account for the added sidebands seen in figure 5.2 the dynamical diffraction calculations have included a static gaussian background.

Figure 5.8a shows the calculated TRXD picture for the symmetric 111 reflection in InSb assuming that the x-ray pulse is perfectly monochromatic and infinitely short. The time dependent oscillations observed in the data are accurately predicted

in the simulation. These oscillations change frequency linearly as a function of angle representing the acoustic dispersion relation (figure 5.8b). The simulation for single crystal Ge shows qualitatively similar results.

The incorporation of 'real world' constraints (i.e. x-ray bandwidth of 1.4eV and 100ps pulsewidth) requires a two-dimensional convolution on the simulation (see figure 5.9). The general structure of the InSb and Ge data are well represented by the simulations. In the case of InSb the time dependent oscillations as well as the lifetime of the sidebands is correctly predicted. In the case of Ge, the increase in diffraction efficiency and the existence of an interference fringe of the compression side is correctly predicted. Although these general features are maintained, there are distinct differences between the accepted theory and the experiments.

5.2.1 Changes to the Thomsen Model

The direct comparison of the data with the Takagi-Taupin calculations can shed light on the deficiencies of the Thomsen model. The experimental diffraction patterns and the calculated diffraction patterns highlights the difference in the symmetric 111 reflection of InSb. Figure 5.10 shows the calculation and data at a laser time delay of 100ps. It is clear that the Thomsen model underestimates the strain in both the compression and rarefaction sidebands. At time delays >500ps the Thomsen model accurately predicts the residual thermal layer.

The data indicate that the relative partitioning of the two components of the Thomsen model (the static heated layer and the propagating phonon pulse) is not accurate. Increasing the relative partitioning of phonon to heating by a factor of two

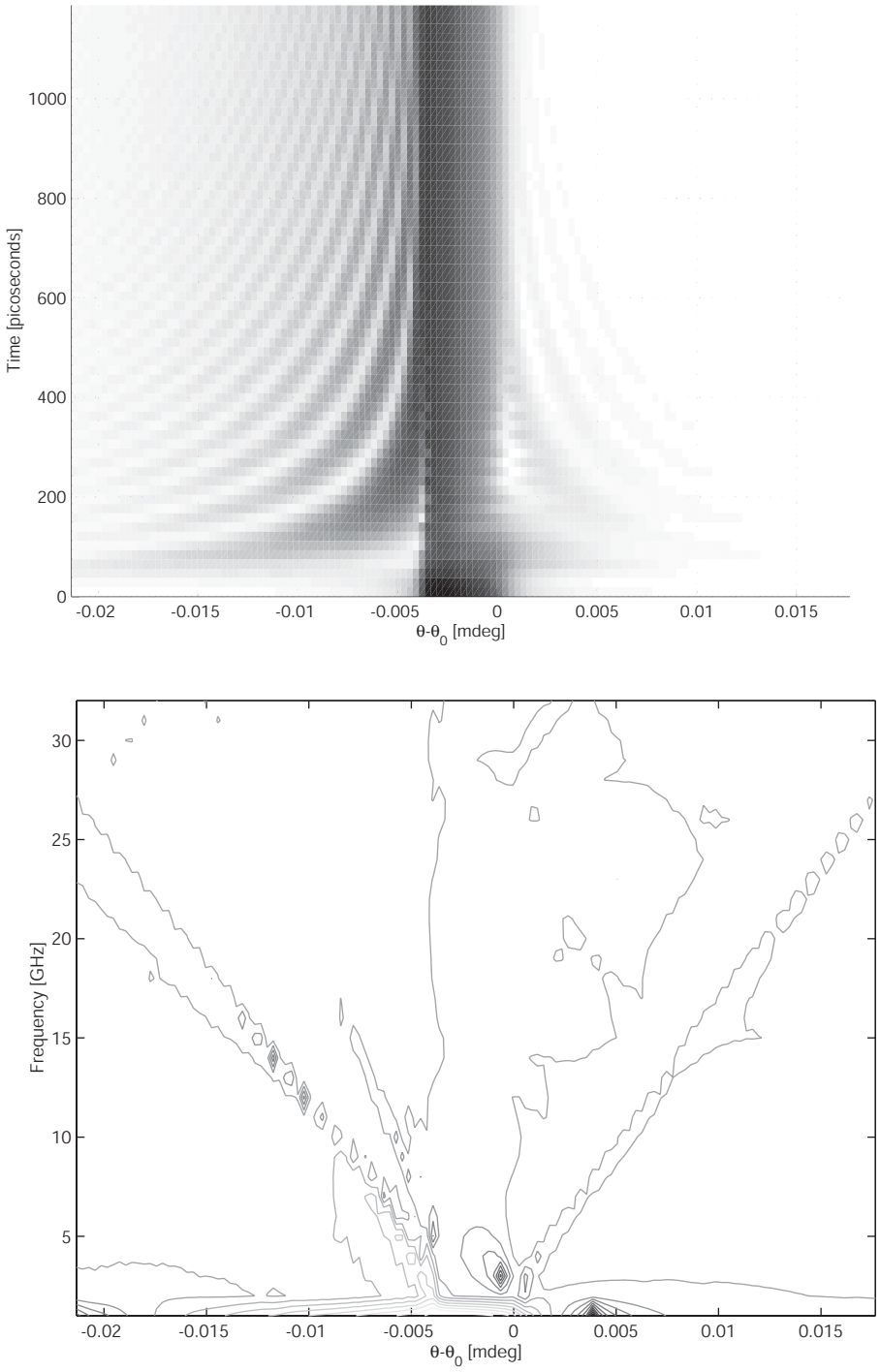

Figure 5.8: (a) Time-resolved x-ray diffraction of the symmetric 111 reflection in InSb calculated using the Thomsen model of strain generation. Adapted from [68].(b) Fourier transform of the time-resolved diffraction calculation. The contours are on a log scale.

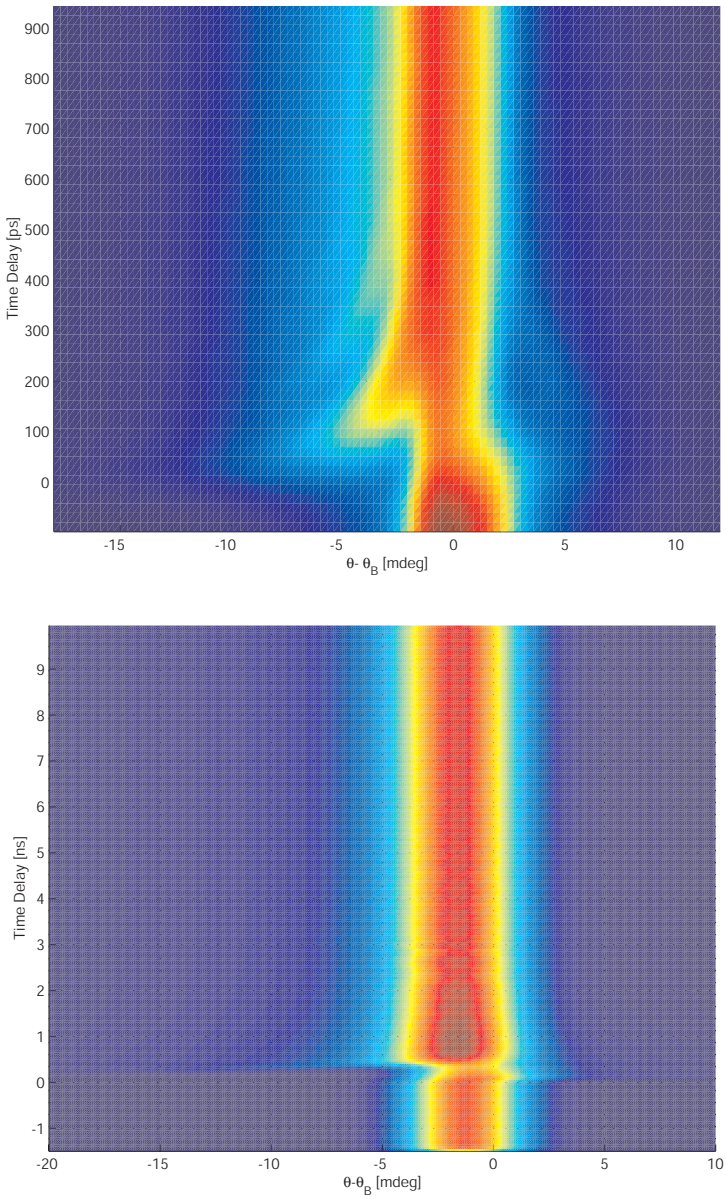

Figure 5.9: (a)Time-resolved Bragg diffraction of InSb using the Thomsen model of strain incorporating 'real world' constraints. Adapted from [68]. (b)'Real world' simulation of Time-resolved Bragg diffraction using the 400 reflection in Ge.

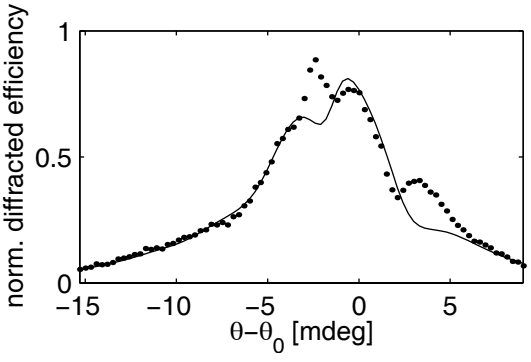

Figure 5.10: InSb data and simulation using the Thomsen model at a time delay of 100ps. Adapted from [68].

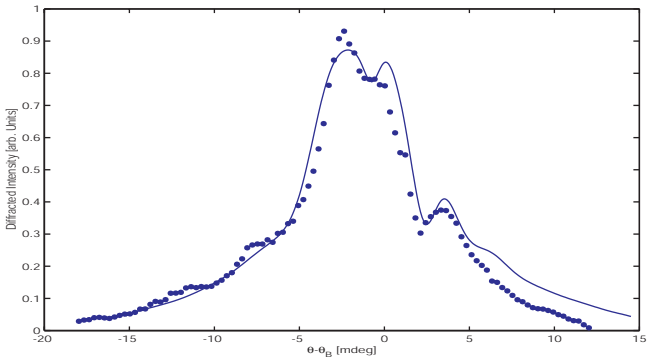

Figure 5.11: InSb data and simulation incorporating the best fit partitioning of energy.

appears to minimize the error between the simulation and the experiment (figure 5.11) [68].

The Ge data also demonstrate that the Thomsen model is not accurate. The compression sideband is visible long after the prediction of the Thomsen model. Cavalleri *et al.* [26] deduced that ultrafast carrier diffusion modified the depth where the strain is generated in Ge. It was claimed that the strain in Ge was initially produced up to $1\,\mu m$ in depth, 5 times the optical penetration depth. The simulation displayed in figure 5.12 assumes a $2\,\mu m$ penetration depth and is the best fit to the data. The discrepancy between Cavalleri *et al.* and this work could be due

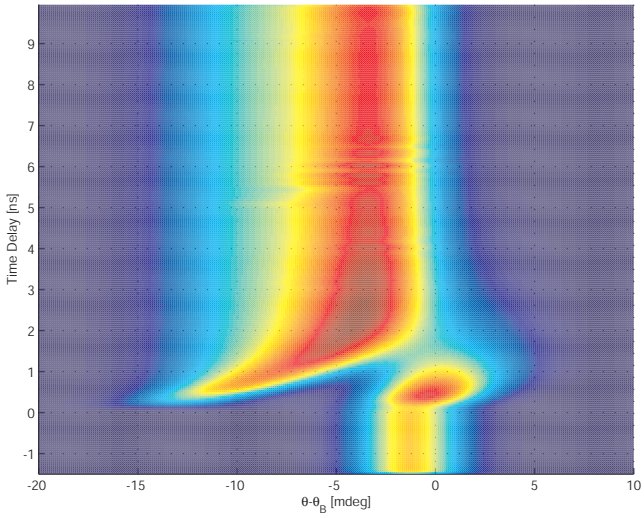

Figure 5.12: Simulation of the time-resolved strain in Ge assuming the strain was generated in a $2\,\mu m$ depth

to the fluence dependence of the ultrafast carrier diffusion [43].

5.3 Transparent materials

In transparent materials the Thomsen model is no longer valid. The ultrafast laser cannot generate a large surface stress and thus an acoustic pulse can not be generated by the ultrafast laser. ZnSe possesses an electronic band gap of 2.6eV[67], making the direct photo absorption with the 840nm laser pulse impossible. ZnSe also possesses very good crystalline quality, making this material ideal for the study of laser induced strain in transparent materials. A TRXD experiment was performed on the symmetric 004 reflection in ZnSe, to study the strain generated using an ultrafast laser (see figure 5.13).

After time zero the peak of the rocking curve appears to have shifted by ∼0.6mdeg. There do not appear to be any sidebands indicating that the crystal lattice undergoes a simple expansion. Assuming a thermal expansion coefficient of $\sim 7.1 \times 10^{-6} K^{-1}$

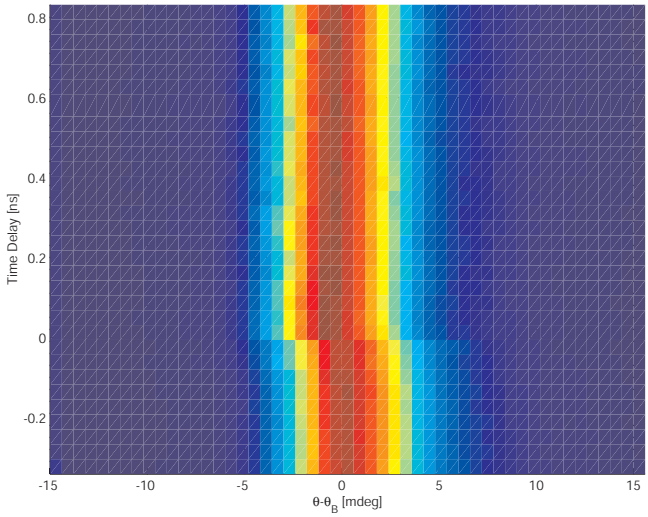

Figure 5.13: Time-resolved Bragg diffraction of the symmetric 400 reflection in ZnSe.

[67], the instantaneous temperature increase is inferred to be about 30 degrees Kelvin. The laser fluence that would need to illuminate the surface, assuming that the absorption takes place throughout the entire crystal, is $\sim$180 $\frac{mJ}{cm^2}$, which is much larger than the experimental value of $\sim$10 $\frac{mJ}{cm^2}$. This observation indicates that heating through a single photon processes is unlikely. The most likely explanation is the two photon absorption due to surface second harmonic generation.

5.4 Acoustic Pulse Evolution

The previous experiments were limited to the study of acoustic pulse propagation within the x-ray extinction depth. For allowed Bragg reflections, this length scale is $\sim$1 micron. A quasi-forbidden reflection, however, can probe depths as large as the incoherent x-ray absorption depth, which can be orders of magnitude greater than the x-ray extinction depth of the strong Bragg reflection. The TRXD data for the quasi-forbidden 222 reflection in InSb is shown in figure 5.14. At zero time delay

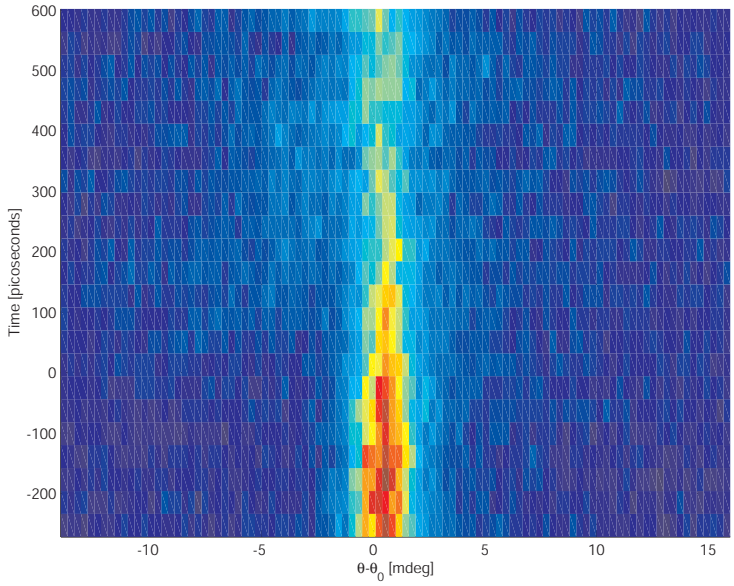

Figure 5.14: Time-Resolved Bragg diffraction of the quasi-forbidden 222 reflection in laser strained InSb. Adapted from [68]

the main diffraction peak reduces in intensity very quickly at the same time weak sidebands are visible[68].

5.4.1 Acoustic Reflections

The diffraction efficiency of a quasi-forbidden reflection is very small making precise measurements of the strain very difficult. Acoustic reflections can extend the effective detection distance inside the crystal. Since acoustic pulses are relatively large wavelength, their dispersion characteristics are such that the acoustic wavepacket should not disperse over many meters (see section 2.2). X-ray Bragg diffraction can then be used to study acoustic pulse evolution over long times.

If the crystal surfaces are highly polished, the impedance mismatch at a crystal/air interface will allow a reflection of an acoustic pulse. At the reflection, the acoustic pulse will experience a π phase shift since the impedance of the air at the

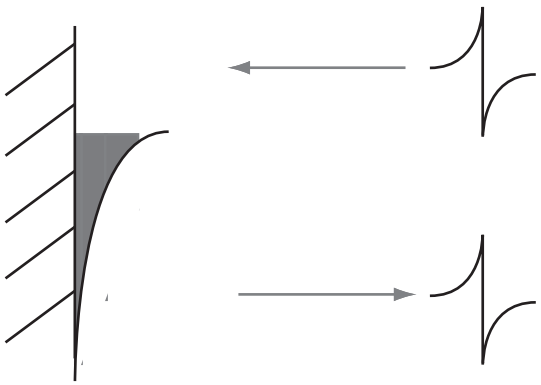

Figure 5.15: Acoustic pulse dynamics upon a reflection

crystal surface is approximately zero[69, 3]. This means that at the time of acoustic collision, the strain at the crystal surface is double the amplitude of the acoustic pulse (see figure 5.15).

An acoustic pulse generated in a $280\,\mu m$ thick piece of single crystal 2 side polished 001 Ge. Measuring the diffraction efficiency of the symmetric 004 reflection, it is seen that at regular intervals (period 110ns) the x-ray intensity increases dramatically for a period $\sim$3ns (figure 5.16). The characteristic frequency associated with the increase in diffraction efficiency is due to the propagation of an acoustic pulse travel time through a $550\,\mu m$ crystal. The time dependent background is due to the static heating of the crystal lattice which diffuses into the crystal bulk. The diffusion time constant is about 150ns.

5.4.2 Acoustic Dispersion

Figure 5.17 shows the time-resolved x-ray diffraction measurement of the first and tenth returns of the acoustic pulse. The first revival corresponds to the acoustic pulse travelling $\sim 550\,\mu m$ while the tenth revival corresponds to an acoustic pulse $\sim$5.55mm travel distance.

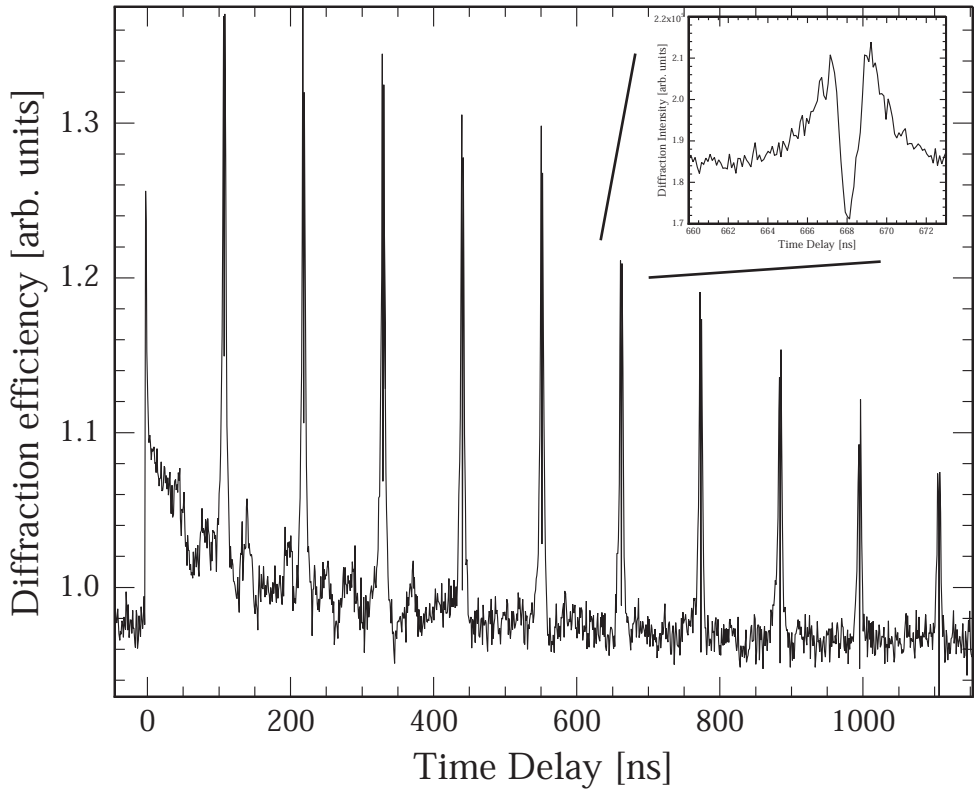

Figure 5.16: Diffracted x-ray intensity as a function of time delay on the rarefaction side of the x-ray rocking curve.

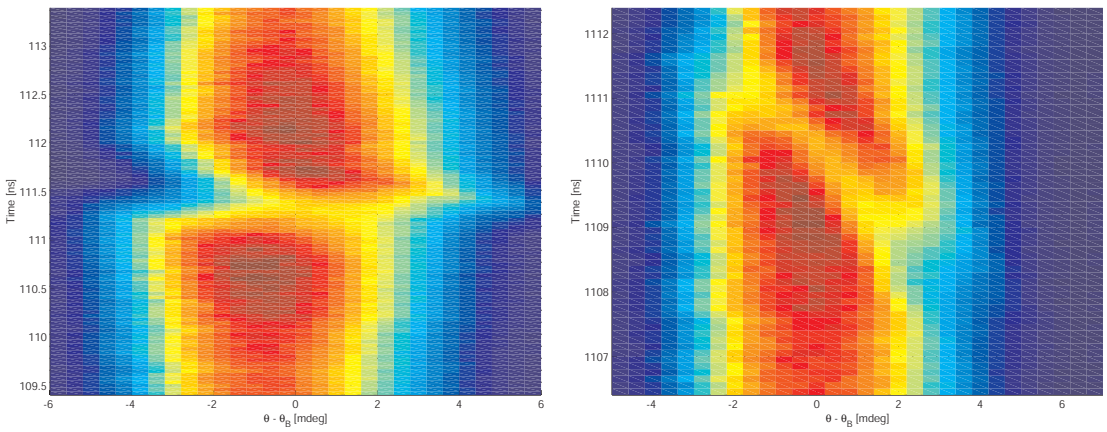

Figure 5.17: Time-Resolved diffraction at an acoustic reflection (a)First revival, (b) tenth revival.

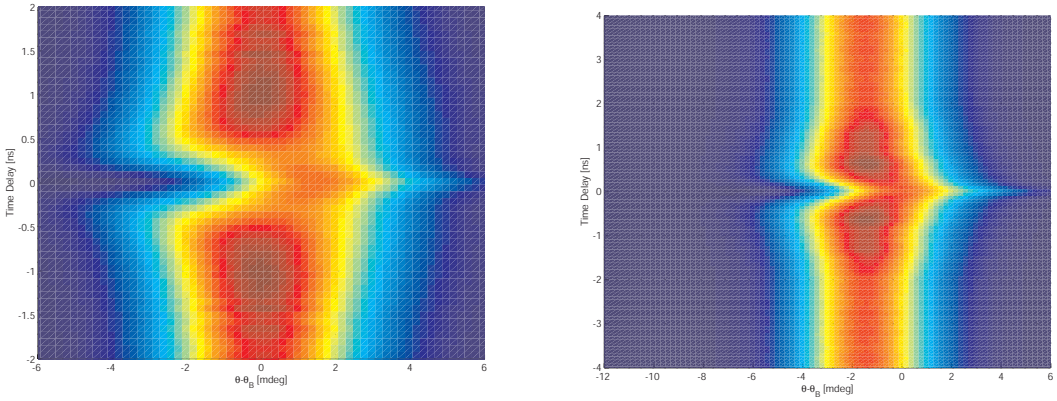

Figure 5.18: Simulation of an acoustic pulse reflection from a Bragg reflection surface. (a) Static heated layer included (b) heated layer not included

To simulate the data, it is assumed that the penetration depth of the laser is 1 μm. During the first revival it is assumed that the static heated layer has decreased in amplitude by a factor of 4, while the tenth revival does not have a heated layer. The laser fluence was a floating variable so that the simulation would fit the data accurately.

During the first revival the diffraction peak appears to be consistent with the Thomsen model (figure 5.18). The compression sideband appears to have increased due to the doubling of the strain at the crystal surface. At the same time, the rarefaction sideband is diminished due to an acoustic pulse interference.

Later reflections, however, do not appear to follow the Thomsen model. The large momentum components seem to have disappeared leaving only the low frequency components of the acoustic pulse. The interference fringe that crosses the diffraction peak changes as the acoustic pulse experiences more reflections. During the first revival, the interference fringe takes half a nanosecond to cross the entire diffraction peak which is consistent with the Thomsen model. In the tenth revival

the interference fringe crosses the entire diffraction peak in about 3ns. This indicates that the acoustic pulse has spatially broadened by over 10 μm.

Assuming that the interference fringe is due to a spatial dispersion of the acoustic pulse, the rarefaction components travel about 0.5% faster than the compression components. By modifying the Thomsen pulse with an added spatial dispersion, qualitative similarities begin to appear. The equations given in chapter 2.2 predict that the amount of dispersion should be on order of an Ångstrom for an acoustic pulse with a 1 μm spatial extent. The exact cause of this dispersion is not yet known, though there are a few possible explanations.

First, the crystal faces may not be perfectly polished. If there are crystal surface variations that are on order of the acoustic wavelength, the acoustic pulse will not experience a perfect reflection due to wave diffraction effects. Because of the nature of diffraction, the high frequencies will diffract much faster than the low frequencies leading to a spatial broadening of the acoustic pulse. The second possible reason is the non-linear frequency attenuation of the crystals. It is quite likely that the attenuation length is different for different frequencies, leading to a dispersed acoustic pulse.

5.4.3 Background free measurements

In all of the previous measurements the direct observation of the phonon component of the strain was distorted by the background of the static heated layer. Changing the diffraction geometry can overcome this problem. If the laser excites the back surface of the crystal, the acoustic pulse will propagate into the diffraction

region with out a static heated layer to interfere with the measurement. After a time corresponding to the crystal thickness divided by the sound speed the acoustic pulse will collide with the front crystal surface. Assuming the crystal is thick when compared to the x-ray extinction depth, the Bragg diffraction will not be sensitive to the static heated surface on the backside of the crystal. The corresponding time-resolved diffraction pattern will only change with the presence of additional crystal momentum components.

Data taken with the backside excitation of Ge demonstrates the observational power of this method (see figure 5.19a). As before, at times preceding the collision with the crystal surface, the peak diffraction efficiency increases. As the acoustic pulse approaches the crystal surface, sidebands on both the compression and rarefaction sides are apparent indicating the existence of high wavevector components. The existence of large expansion sidebands at the collision point indicates the effective doubling of the surface strain due to the π phase shift upon acoustic reflection. Assuming a $1\,\mu m$ strain depth, the data appears to correspond quite well with the Thomsen model (figure 5.19b).

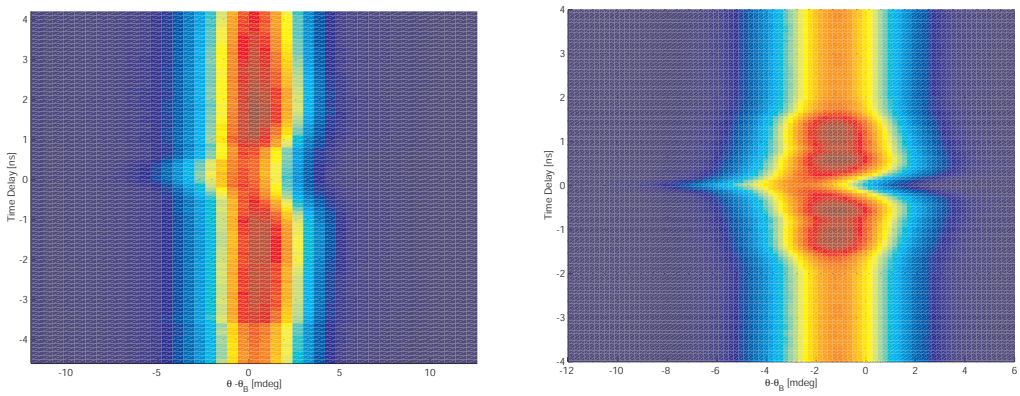

Figure 5.19: Time-resolved X-ray Bragg diffraction due to the backside laser excitation of 001 Ge.

CHAPTER VI

Time-Resolved X-ray Laue Diffraction: The Symmetric Reflection

Although the x-ray Bragg diffraction is an effective tool for studying time dependent strains, the small extinction depth of the diffracting x-rays does not allow the continuous monitoring of a propagating strain in thick crystals. Laue diffraction can circumvent this problem due to the fact that the x-rays will now diffract throughout the bulk of the crystal.

In the symmetric Laue geometry, a laser generated strain is perpendicular to the reciprocal lattice vector. This geometry allows the study of transverse strains and/or novel phonon coupling to x-ray diffraction. Asymmetric Laue diffraction can provide complementary information since the generated strain will have a component along the reciprocal lattice vector and will be discussed in the next chapter.

Traditional Laue diffraction is typically limited to very thin crystals ($<10\ \mu m$) or very large x-ray energies (>20 keV). Though thick crystals can be probed with high energy x-ray photons, the generation and detection of these photons makes time-resolved experiments difficult (APDs and photocathodes are not efficient detectors of $>$ 20keV photons). Nevertheless, coherent acoustic phonons with MHz frequencies

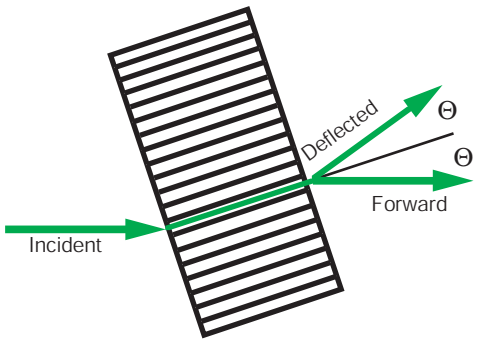

Figure 6.1: The symmetric Laue geometry.

have been studied using 30keV x-rays in the Laue geometry[15].

There is, however, a diffraction effect which extends the probe depth of x-rays regardless of the photon energy, x-ray anomalous transmission (see chapter III). Utilizing x-ray anomalous transmission, a.k.a the Borrmann effect, crystalographers have studied lattice dislocations and crystal defects in crystals that are much deeper than the incoherent absorption depth [11]. Studies using the Borrmann effect in the time-domain have been extremely limited[70, 71]. This chapter reports data on novel time-resolved experiments using x-ray anomalous transmission.

6.1 Data

In the symmetric Laue geometry the lattice planes are oriented such that the reciprocal lattice vector is perpendicular to the surface normal (figure 6.1). A 001 Ge single crystal is oriented to diffract from the symmetric 220 diffraction plane with 10keV x-rays. An ultrafast laser impulsively heats the crystal surface, generating a large surface strain. At large fluences ($> 5\,\frac{mJ}{cm^2}$) the generated thermal gradient strains the crystal to such an extent that the x-ray anomalous transmission is destroyed (figure 6.2). As the laser heats the sample the diffraction efficiency disappears

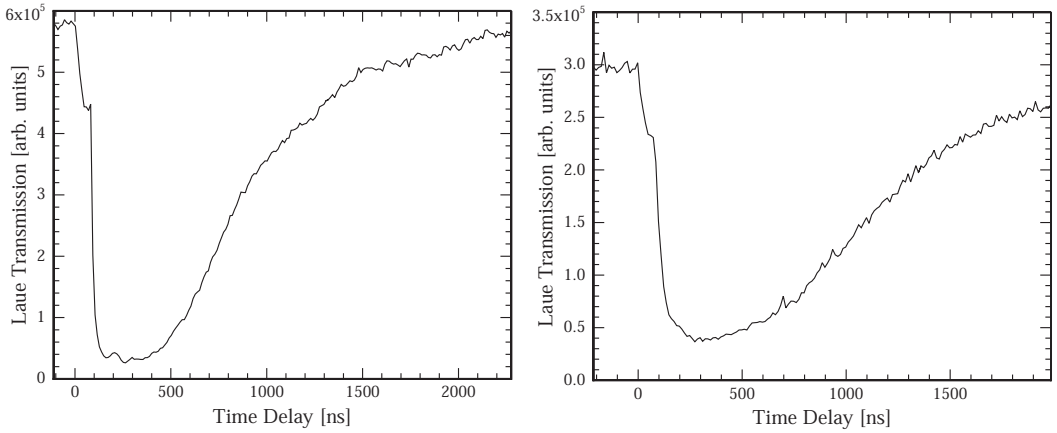

Figure 6.2: Time-resolved anomalous transmission after intense laser excitation. 220 reflection (left) and 440 reflection (right)

in ∼100ns. As the crystal reaches a thermal equilibrium, the wave guide is restored and the anomalous transmission recovers. However, if the laser pulse melts the material (fluences >50 $\frac{mJ}{cm^2}$) repetitive laser heating ($\sim 10^6$ laser shots) can permanently strain the crystal through imperfections in the recrystallization process. This induced static strain slowly reduces the average efficiency of the Borrmann effect to zero.

The loss of x-ray anomalous transmission when a crystal experiences a thermal gradient was observed in Borrmann's original experiments [72]. Borrmann observed that a thermal gradient of only 0.6 degrees Celsius is sufficient to destroy the anomalous transmission. He determined that the thermal gradient generates a static stress such that the x-ray wave guide is destroyed causing massive absorption. Experiments performed in the Bragg geometry have indicated that ultrafast laser absorption can cause a temperature rise at the crystal surface equaling many tens of degrees. This evidence indicates the reduction in diffraction efficiency is due to the temperature gradient generated by the laser pulse.

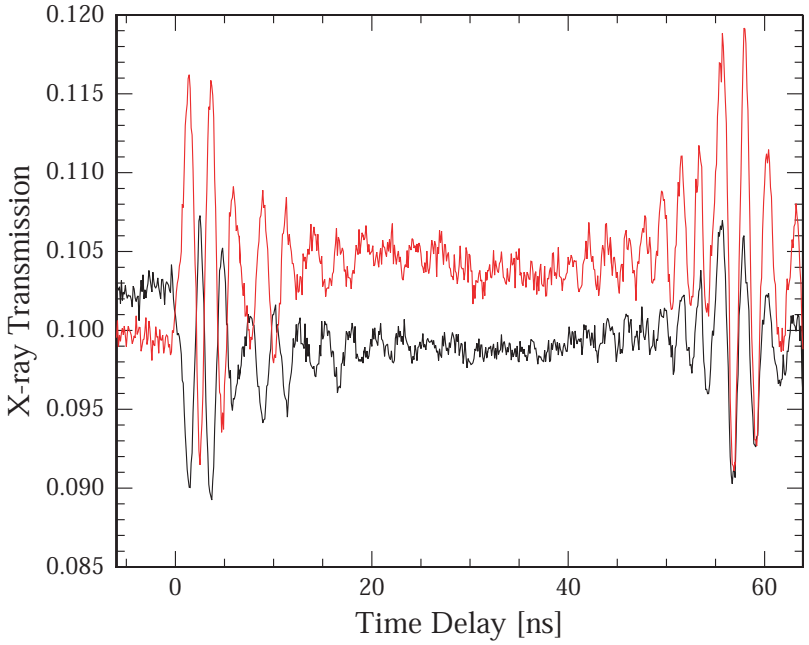

Figure 6.3: X-ray transmission for the 220 symmetric reflection in 001 Ge as a function of time delay.

Reducing the incident laser fluence reduces the temperature gradient allowing the observation of long term changes in the x-ray transmission. Figure 6.3 shows the diffracted intensity of the forward and deflected beams as a function of time delay (incident fluence $\sim 1\,\frac{mJ}{cm^2}$). Immediately after the generation of the acoustic pulse, the intensities of the two diffracted beams begin to oscillate. As the time delay increases, the intensity of the forward and diffracted beams oscillate out of phase with a period of $\sim$ 1.7ns. The amplitude of oscillations decreases with a decay constant of $\sim$10ns.

When the time delay exceeds 27ns (after the acoustic pulse crosses the midpoint of the crystal) the oscillations return. The oscillations grow in amplitude with the same time constant and period that was observed at earlier time delays. However, the observed modulations in the diffracted beams now oscillate in phase. At a time

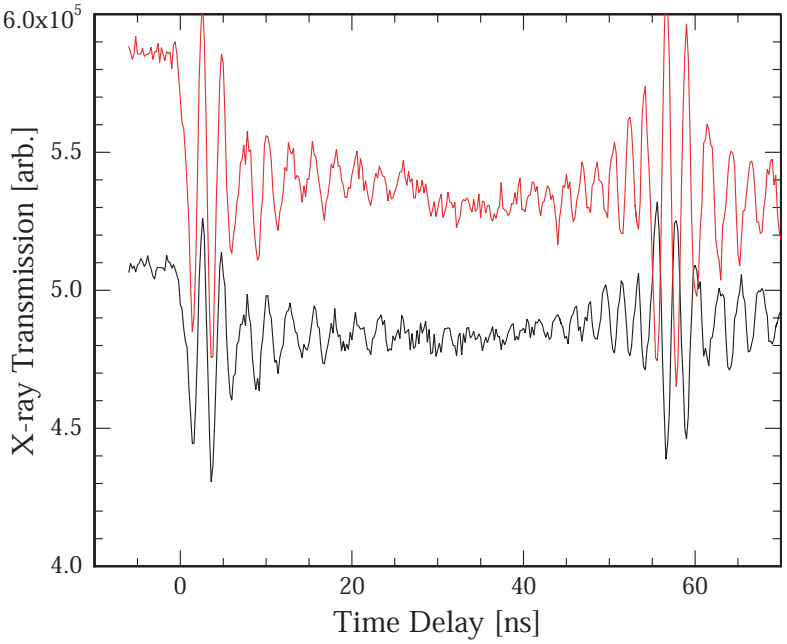

Figure 6.4: Time-resolved diffraction of the symmetric 220 reflection, front side excitation.

delay of 55ns the amplitude of the oscillations reaches a maximum. This time delay corresponds to the traversal time of the acoustic pulse through the 280 μm thick crystal.

Similar features are observed when the acoustic pulse starts at the input face of the crystal (figure 6.4). The only obvious difference is that the relative phase of the two diffracted beams changes. At times close to zero time delay the beams oscillate in phase while at delays ∼55ns the beams oscillate out of phase. The relative phase of the oscillations appears to be completely dependent on the location of the acoustic pulse. A clear explanation of the observed data is provided by the x-ray dispersion surface.

6.2 Predictions using a Rotation of Basis

For crystals in the Laue geometry, the x-ray dispersion surface predicts that as the crystal thickness changes, the forward and deflected beams will oscillate (the Pendellösung effect). Dividing the Pendellösung period by the sound speed of Ge, the observed period of oscillation is found. A simple model is presented below which accurately predicts the observed data.

6.2.1 Two Crystal Model

As described in chapter III there are two linearly independent solutions to the x-ray wave equation inside a perfect crystal, α and β. Due to the strong absorption of the β solution, the exterior wave solutions will change in magnitude as the crystal thickness changes. Localized static strains or crystal defects can rotate the $(\alpha \ \beta)$ basis causing a change in the relative amplitude of the forward and deflected beams [11]. Since the sound speed is much less than the group velocity of the x-rays, the acoustic pulse will appear to be a static strained layer. If the spatial dimension of the acoustic pulse is much less than that of a Pendellösung depth, this situation can be described fairly well as two crystals separated by a very thin strained interface (see figure 6.5).

To simulate this effect,the strained interface is treated as a simple rotation of the α, β basis [73]:

$$\begin{bmatrix} \cos\Theta & -\sin\Theta \\ \sin\Theta & \cos\Theta \end{bmatrix} \begin{pmatrix} \alpha \\ \beta \end{pmatrix} \tag{6.1}$$

After the x-rays interact with the strained region, the transmitted x-ray fields evolve

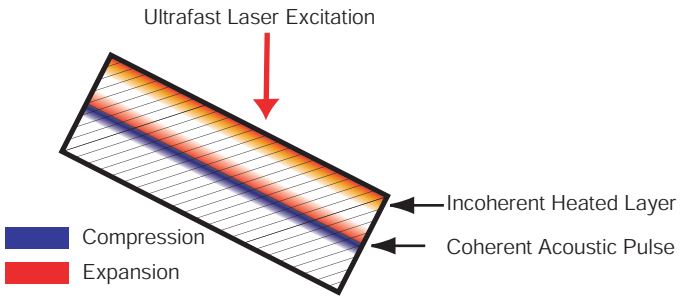

Figure 6.5: A schematic representation of the two crystal model.

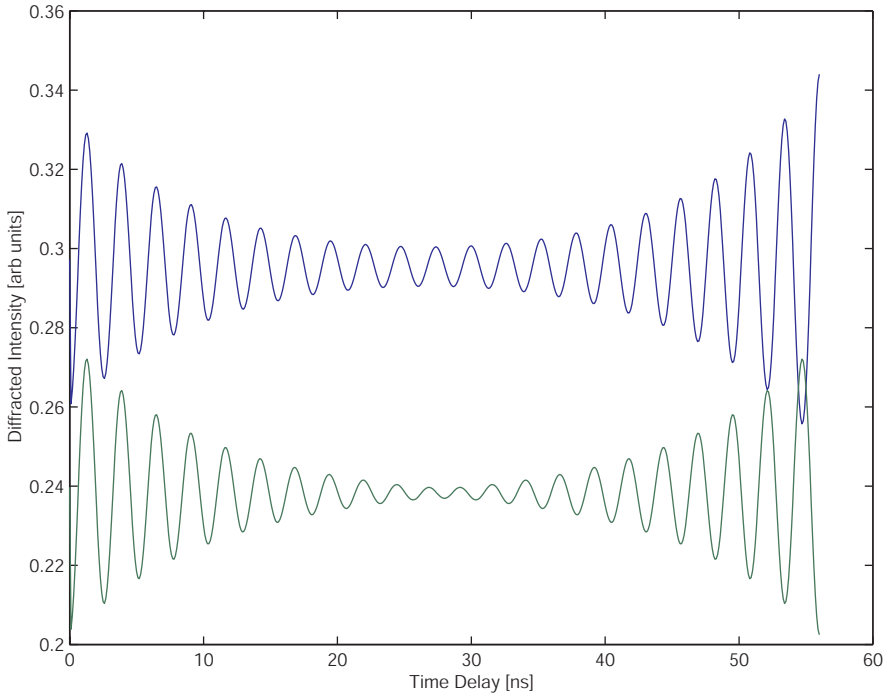

Figure 6.6: A simulation of the two crystal model.

as governed by the theory of dynamical diffraction. Figure 6.6 shows the result of this calculation assuming that the acoustic disturbance moves from the output face anti-parallel to the x-ray poynting vector. The amount of rotation used in the simulation is $\pi/40$ radians.

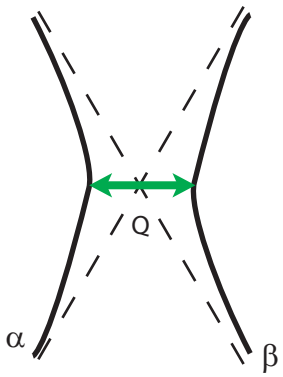

Figure 6.7: This x-ray dispersion surface coupled with a phonon wavevector Q.

6.2.2 Mechanism

Although the simple rotation of basis appears to correctly predict the observed modulations, the exact mechanism of the transfer is not immediately obvious since the phonon wavevector, q, is perpendicular to the reciprocal lattice vector. Again the x-ray dispersion surface provides clues to determining the mechanism of the effect. In the symmetric Laue geometry, q is in the direction of the spacing of the dispersion surfaces (figure 6.7). If the generated acoustic pulse has enough bandwidth to include the momentum spacing of the two dispersion surfaces, the phonon can bridge the α and β branches of x-ray dispersion surface causing a coherent transfer of population. This effect has been observed in the frequency domain using narrow band acoustic phonons[13].

When the acoustic pulse is close to the output face, the x-rays that interact with the strained layer are completely dominated by the α solution since the β solution has long since been absorbed. In the presence of the acoustic pulse the β solution can be repopulated. Since this interface propagates, the effective crystal thickness following the strained region changes over time. The diffracted intensities will then

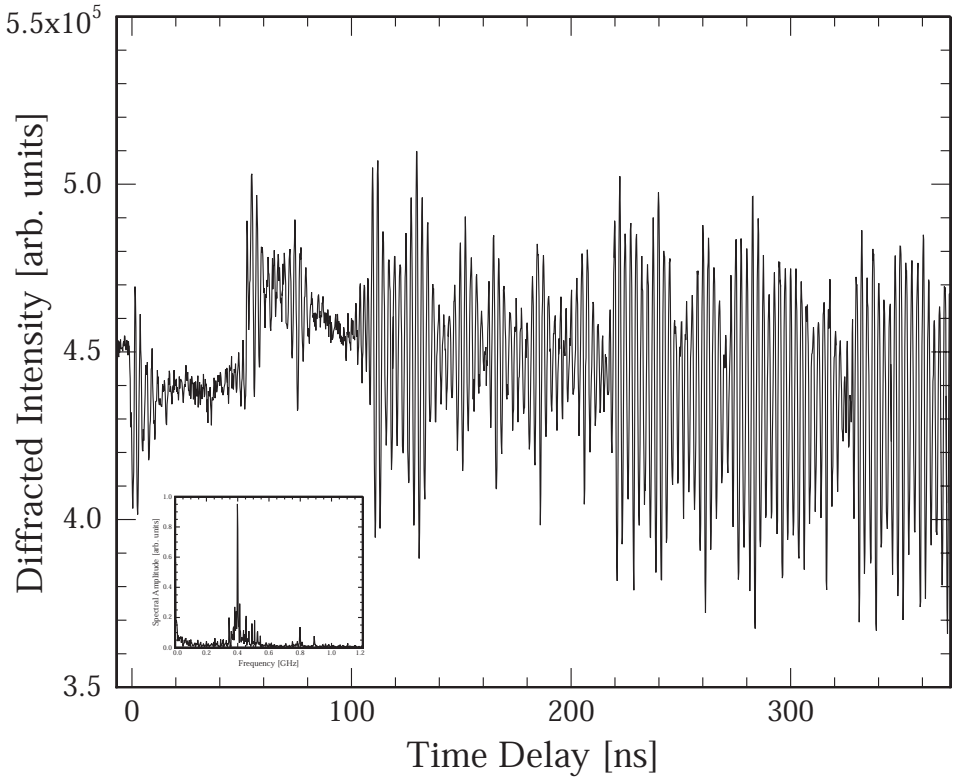

Figure 6.8: Time-dependent intensity oscillations of the forward 220 reflection is Ge. Inset: the Fourier transform of the oscillations

beat against each other as a function of time via the Pendellösung effect[73].

If the acoustic disturbance is located closer to the input side, however, both the β and α solutions are populated approximately equally prior to the interaction with the strained layer. The strained layer will simply remix the solutions causing the amount of population in each solution to change as a function of depth. Since there is a large undisturbed crystal following the strained layer the β solution will be absorbed quickly leaving only the α solution. Since α is the only solution to exist, the beams will be modulated equally.

6.3 Long Time Delays

After one round trip the two crystal model appears to break down(see figure 6.8). Unlike the Bragg case, there does not appear to be a correlation between the peaks of the transmission and the location of the acoustic pulse. The main feature of the Fourier transform continues to be the wavevector of the dispersion surface. However, other wavevectors are also apparent in the spectrum, such as the second harmonic. The second harmonic may be due to the fact that at a crystal interface the acoustic pulse propagates in both directions and that there are some two phonon processes associated with the rotation of basis, but the exact nature of these other spectral components is unclear.

As before, at certain time delays the forward and deflected beams oscillate out of phase. The difference signal between the two diffracted intensities highlights this fact (figure 6.9). Initially the two crystal model correctly predicts the x-ray transmission. After a single round trip of the acoustic pulse, however, the oscillations in the x-ray transmission becomes erratic until the difference signal almost becomes a continuous wave.

Again, like the raw signal, the reason for the continuous Pendellösung oscillations is not entirely clear. Although, the data reported in the previous chapter may lead to an answer. As the pulse propagates through the crystal, it was seen that there was significant dispersion to the acoustic pulse. This dispersion may allow components of the acoustic pulse to redistribute the population of the α, β basis for an extended period of time. Another possibility is that the static heated layer is interacting

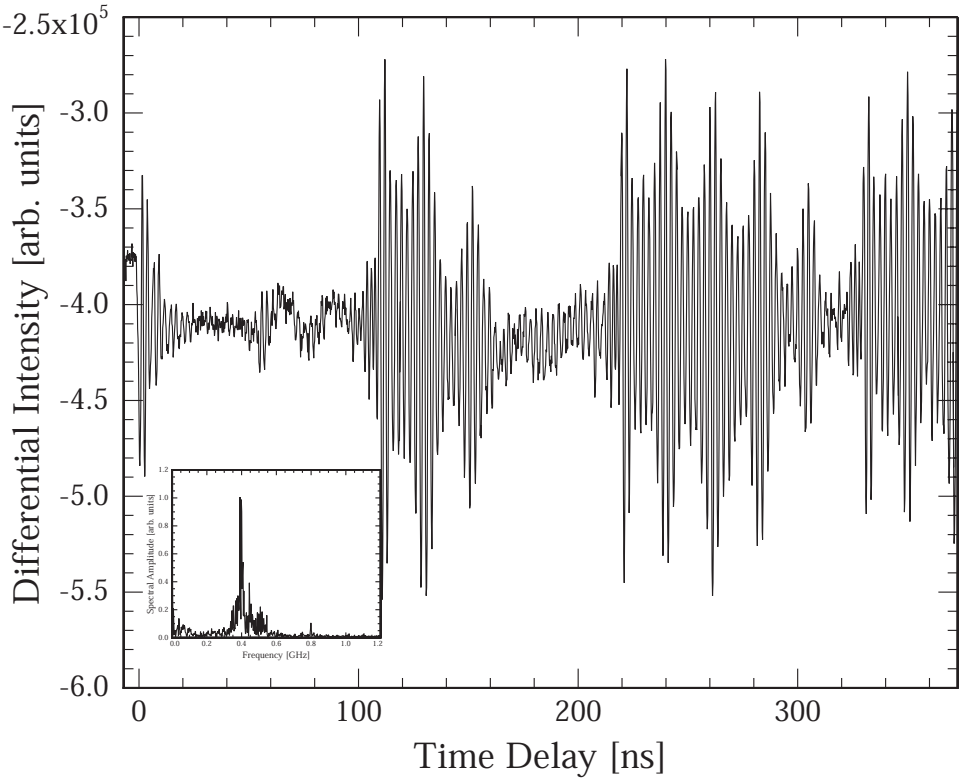

Figure 6.9: Difference of the forward and deflected intensity of the 220 reflection in Ge. Inset: Fourier transform of the oscillations

with the reflecting acoustic pulse. It is known from the Bragg data, that the static heated layer will diffuse slowly into the crystal bulk. This static layer may distort the crystal enough to either couple the x-ray dispersion surface and/or change the boundary conditions of the acoustic pulse reflection.

CHAPTER VII

Time-Resolved X-ray Laue Diffraction: The Asymmetric Reflection

The previous two chapters demonstrated the ability of time-resolved x-ray diffraction to study strain propagation. X-ray Bragg diffraction and symmetric x-ray Laue diffraction, however, have conflicting limitations. X-ray Bragg diffraction can provide a precise study of strain, but x-ray probe depth is limited to the x-ray extinction depth (or the x-ray absorption depth). Symmetric x-ray Laue diffraction can detect crystalline strain very deep within crystals, but due to the direction of the reciprocal lattice vector, symmetric Laue diffraction is unable to precisely measure a laser induced strain. Asymmetric Laue reflections can overcome these problems.

Unlike the symmetric Laue geometry, an asymmetric Laue reflection is one where the reciprocal lattice vector is not perpendicular to the surface normal. Therefore, a laser generated strain has a component along the reciprocal lattice vector, making the strain detectable. At the same time, x-rays that diffract from an asymmetric Laue plane can propagate via the Borrmann effect. These two facts make an asymmetric reflection an ideal probe for strain pulses propagating through very thick crystals.

A new experimental problem arises due to the crystal asymmetry. The laser

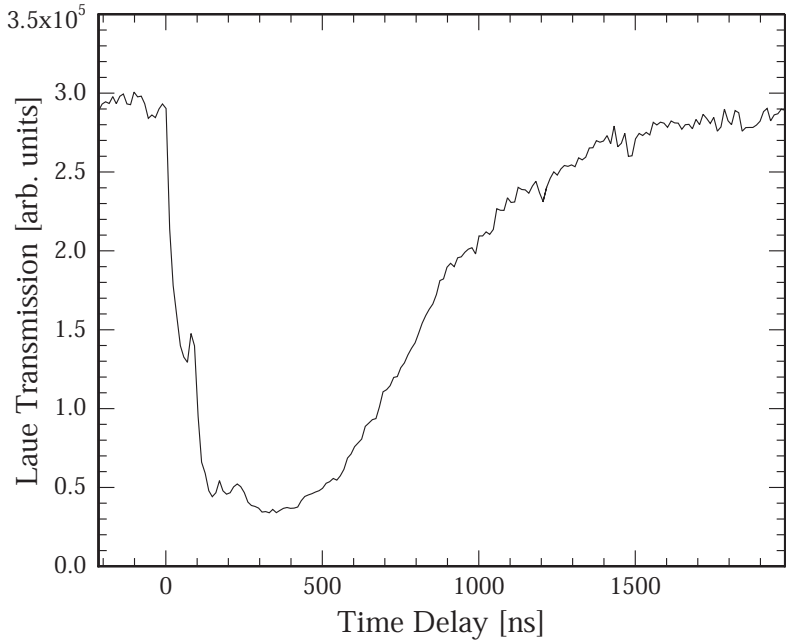

Figure 7.1: $20\overline{2}$ diffraction efficiency under intense laser excitation.

generated acoustic pulse will not travel anti-parallel to the Poynting vector of the diffracting x-rays. To compensate for this potential difficulty, the optical pulse illuminates a relatively large surface area. This provides a large spatial profile to the propagating acoustic pulse and thus the spatial walk off between the acoustic pulse and the x-ray probe is assumed to be negligible.

7.1 Experiment

A Ge 001 crystal is oriented to diffract from the $20\overline{2}$ diffraction plane. The asymmetry angle is 45 degrees for this reflection, midway between a symmetric Bragg reflection and a symmetric Laue reflection. An ultrafast optical pulse generates an acoustic disturbance on either face of the crystal.

7.1.1 APD Data

Like the symmetric data, under intense laser excitation the diffraction efficiency of the asymmetric reflection goes to zero for an extended period of time (see figure 7.1). Unlike the symmetric geometry, as the laser fluence is reduced the diffraction efficiency of the forward beam does not recover. In figure 7.2 the peak diffraction intensity of both the forward and deflected beams of the Ge crystal is shown as a function of time delay. In this case the acoustic pulse was initially generated on the output face of the crystal.

Immediately after the laser absorption (fluence $\sim 5\,\frac{mJ}{cm^2}$), the intensity of the two diffracted beams changes rapidly. The forward beam decreases while the deflected beam increases by the same amount, indicating a coherent transfer of energy. Up to 70% of the x-rays are coherently transferred between beams. The time dependence of this phenomenon is comparable to the x-ray pulse width indicating the switching mechanism is at least as fast as the 100ps x-ray pulse width.

The population transfer for diffraction from the $\overline{2}02$ diffraction plane (asymmetry -45 degrees) is the mirror image of $20\overline{2}$ case. The diffracted intensity of the forward beam now decreases while deflected beam increases (figure 7.3). Again, the time-scale for transfer appears to be limited by the x-ray pulse width.

The fast phenomenon does not appear to have an angular dependence. This may be due to the wavevector selectivity of the Borrmann effect. In the strained region, like the Bragg case, sidebands on the diffraction peak are generated. The modified Laue condition cannot be satisfied, however, becasue of the wave vector selectivity of

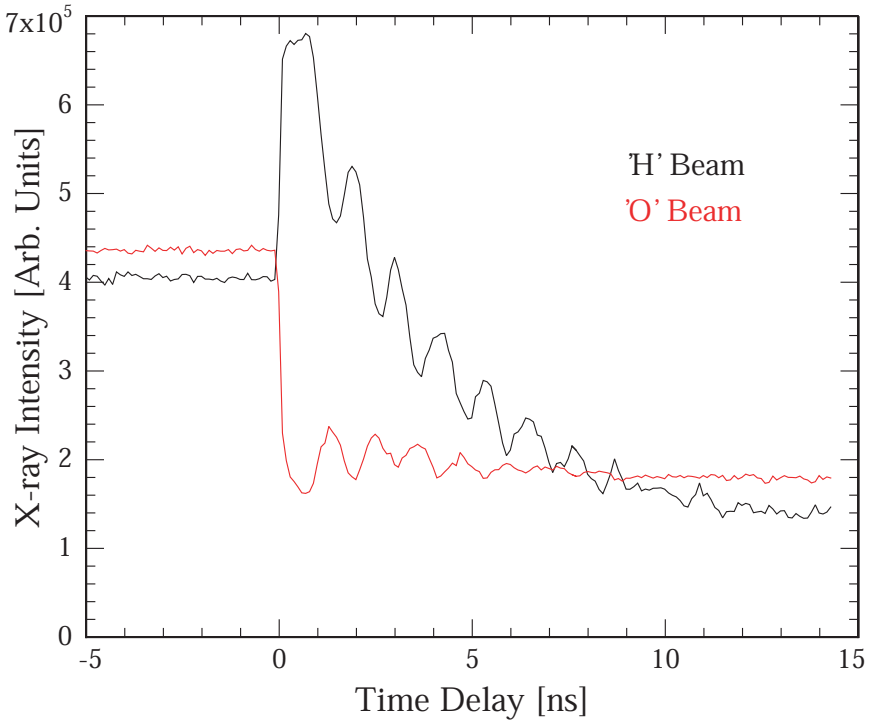

Figure 7.2: The peak diffraction efficiency of the asymmetric $20\overline{2}$ Laue reflection as a function of Laser/X-ray time delay.

the Borrmann effect. So unlike the Bragg case where sidebands are easily observed, in the Borrmann geometry only those wave vectors which satisfy the Laue condition propagate through the crystal.

Following the rapid population transfer, oscillations in the diffracted intensity are visible. These oscillations are due to the bridging of the x-ray dispersion surface. Following the method described in the preceding chapter, the acoustic pulse redistributes the relative population of the α, β basis causing the onset of Pendellösung oscillations.

The generation of an acoustic pulse on the input face of the crystal displays similar features. As in the symmetric case, when the acoustic pulse is generated on the input face both diffracted beams initially behave identically (see figure 7.7).

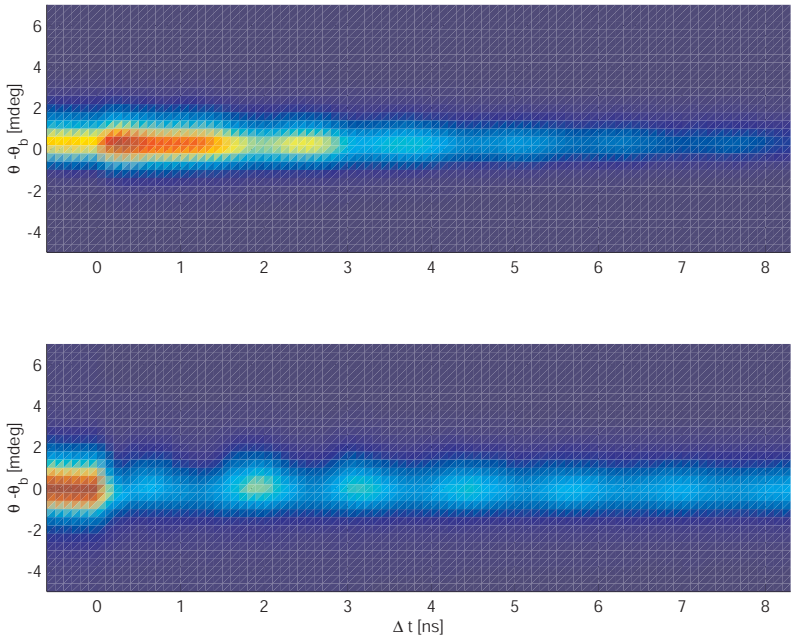

Figure 7.3: X-ray transmission as a function of angle and time delay for the asymmetric $\bar{2}02$ Laue reflection. (top) forward beam, (bottom) deflected beam. Adapted from [73].

Again this is due to the fact there is a large unperturbed region beyond the strained crystal layer.

As the incident fluence changes, the efficiency of the fast transient changes as well. As stated above, the maximum transfer appears to be $\sim 70\%$. As the fluence is reduced, however, the efficiency of the switch changes but the resultant Pendellösung oscillations appear to be unaffected (see figure 7.5). At low fluences ($<1\,\frac{mJ}{cm^2}$), the Pendellösung oscillations and the fast transient start with the opposite phase. The exact mechanism controlling this physical effect is unclear, but it could indicate the length scale associated with the fast mechanism.

The last observed effect is that the decay constant of the increased beam changes with incident fluence. The other beam, however, does not benefit from this decrease

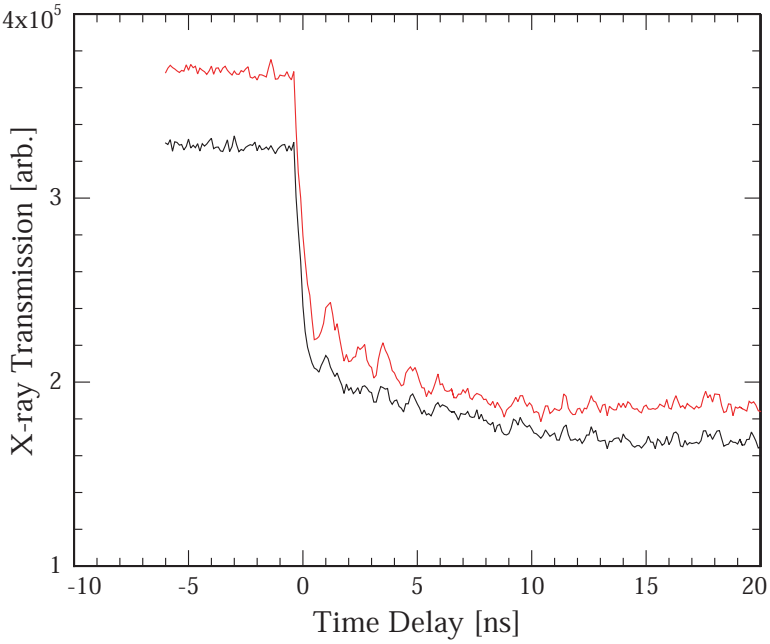

Figure 7.4: X-ray transmission as a function of optical pulse time delay of the asymmetric $\overline{2}02$ Laue reflection. The acoustic pulse is generated on the input side of the crystal.

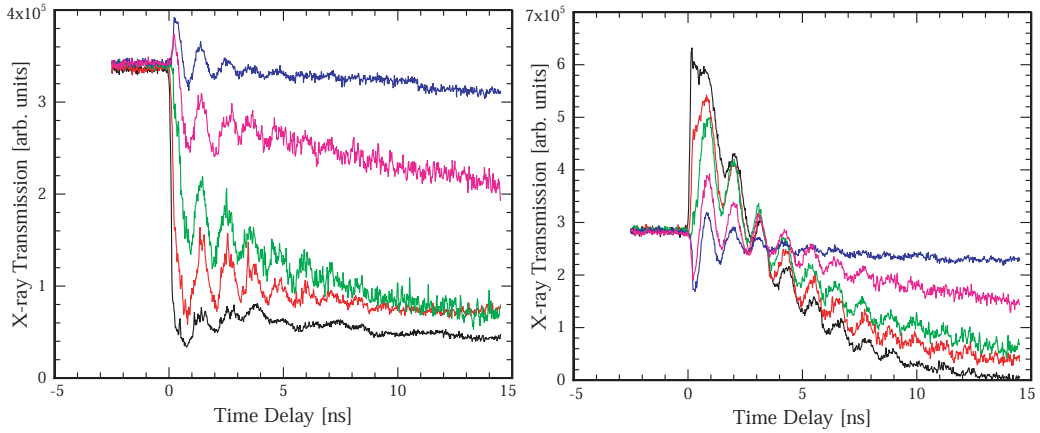

Figure 7.5: The time dependent diffraction efficiency as a function of optical fluence. black: 10 $\frac{mJ}{cm^2}$, red: 7 $\frac{mJ}{cm^2}$, green: 5 $\frac{mJ}{cm^2}$, purple: 3 $\frac{mJ}{cm^2}$, blue: 1 $\frac{mJ}{cm^2}$

diffraction efficiency, indicating this loss is not a unitary transfer of population. This decay in diffraction efficiency is probably due to the strain components along the direction of the reciprocal lattice vector. The x-rays that enter the strained region can be diffracted out of the x-ray channel and absorbed by the remaining substrate. As the fluence increases (and thus the magnitude of the strain) the fraction of the incident x-rays that are ejected from the x-ray waveguide increases and thus the amount of decay rises.

7.1.2 Acoustic Reflections

As the acoustic pulse approaches the opposite crystal face of the crystal, a 'Borrmann revival' is observed. As the transmission returns, Pendellösung oscillations in the diffracted intensity are seen. Like the symmetric case, as the acoustic pulse approaches the input face the oscillations in the two beams are in phase (figure 7.6). As the acoustic pulse collides with the input face of the crystal, the intensity of the forward beam is about 2.5 times that of the static crystal case or greater than the sum of the two diffracted beams of an unstrained crystal.

This dramatic increase in the diffraction efficiency can be explained by the two crystal model. In the static crystal case the sum of the output intensities can be no larger than one half of the original input intensity due to the strong absorption of the β solution. In the best case scenario the amount of increase in one beam due to the rotation of the α, β basis on the output face of the crystal is only a factor of 2. However, if the basis rotation occurs on the input face, the entire initial β population can be transferred to the α solution, increasing the output of one beam

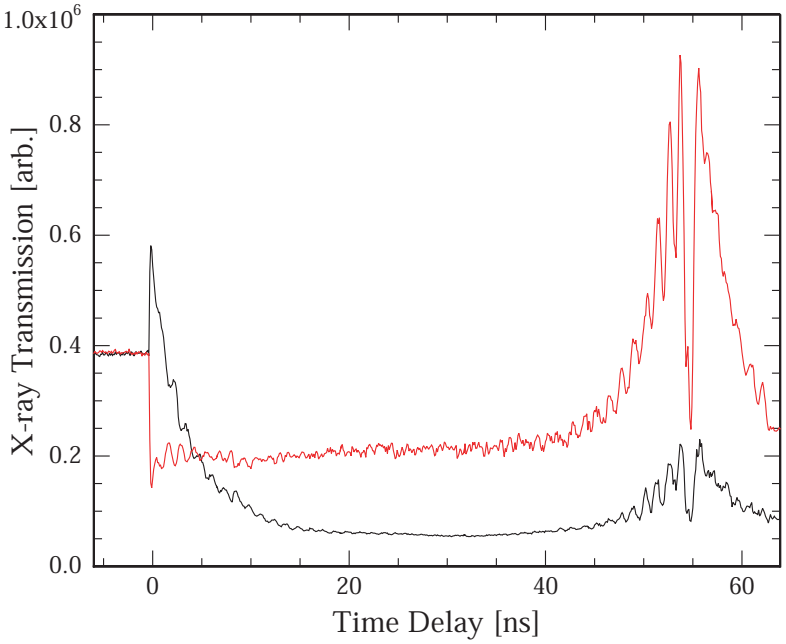

Figure 7.6: X-ray transmission as a function of acoustic pulse time delay. The acoustic pulse is now approaching the input face of the Ge crystal. Adapted from [73].

by upto a factor of 4. If the acoustic pulse originates from the front side of the crystal, a similar diffraction revival is seen (figure 7.7). The observed Pendellösung oscillations during the revival are now out of phase and the sum of the two diffracted beams is ∼50% that of the unstrained crystal case, consistent with the two crystal model.

These Borrmann revivals provide information on the partitioning of energy between the acoustic pulse and static heated layer predicted in the Thomsen model. Although the strain generated by the static heated layer is in the same direction as the acoustic pulse, the Borrmann revivals indicate that the static heated layer does not play an important role in the diffraction experiments. This may indicate, as in the Bragg experiments, that the static heated layer is considerably over estimated in

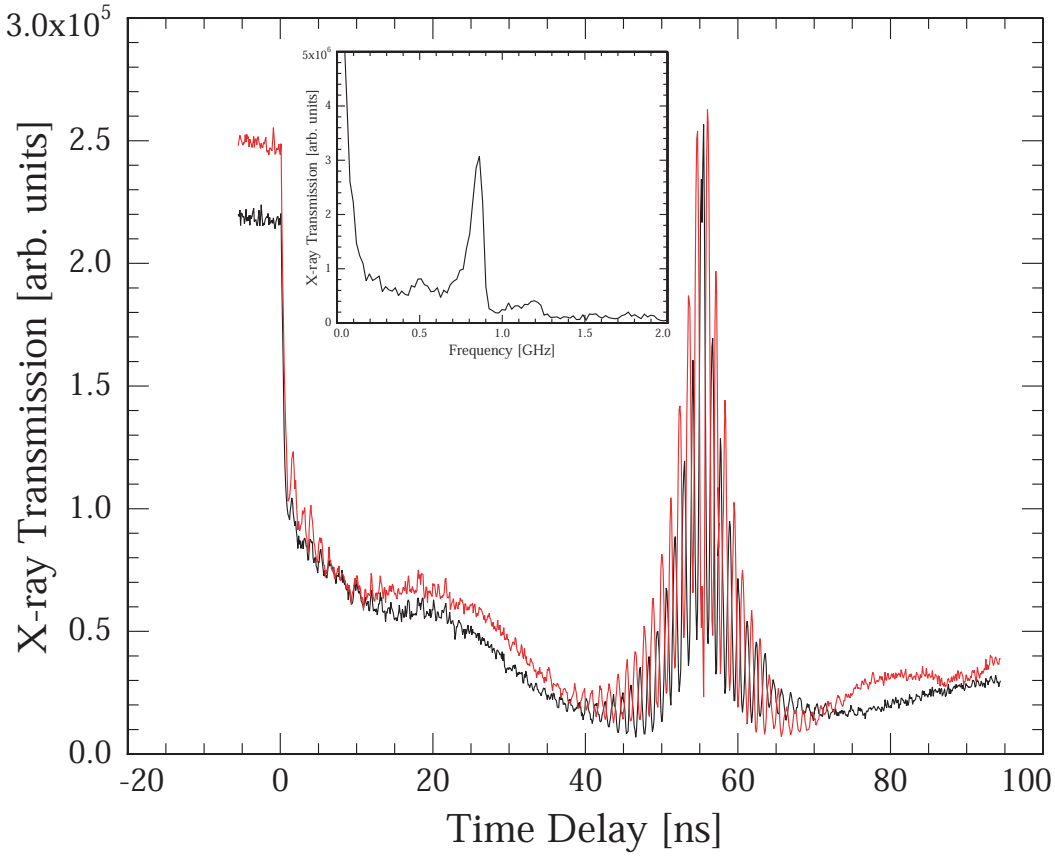

Figure 7.7: X-ray transmission as a function of optical pulse time delay of the asymmetric $\overline{2}02$ Laue reflection. The acoustic pulse is generated on the input side of the crystal.

the Thomsen strain model.

An attempt was made to explore the optical properties of the fast effect (figure 7.8). The incident optical light was frequency doubled using a non-linear crystal. The optical penetration depth of the 420nm radiation in Ge (∼15nm) is significantly less than the 840nm radiation (∼225nm).

The fast transfer of energy is not visible with ultraviolet radiation. This may be due to the relatively low optical fluence and thus the acoustic strain amplitude is also small. The other obvious fact is that there is no observation of a Borrmann revival. This is probably due to the large wavevector of the acoustic pulse. In this case

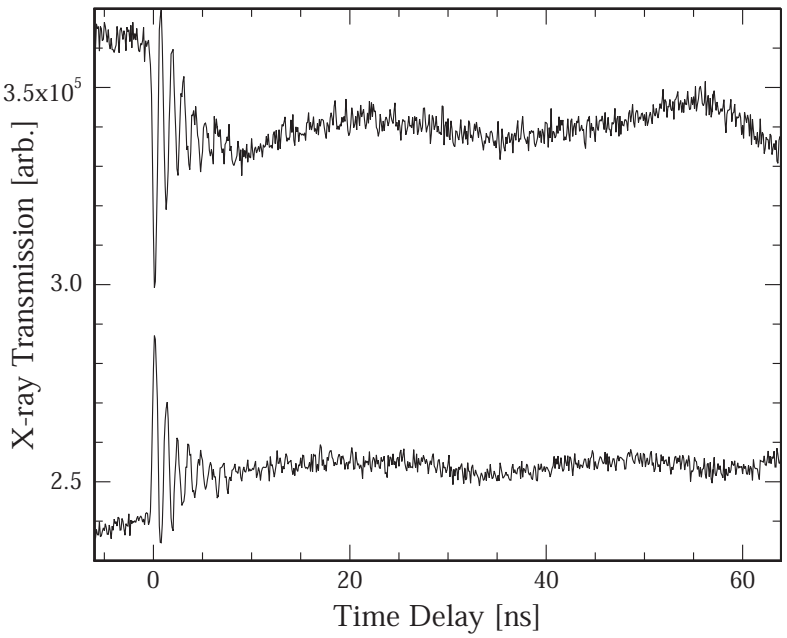

Figure 7.8: Time-Resolved diffraction of the asymmetric $20\overline{2}$ reflection illuminated using a 420nm optical pulse.

the acoustic pulse dispersion and absorption is significant. At the opposite crystal face the remaining frequencies of the acoustic pulse are not be able to bridge the dispersion surface.

As in the Bragg geometry, upon each acoustic pulse reflection a Borrmann revival is observed (figure 7.9). Unlike the Bragg geometry, the efficiency of the Borrmann revival is not static. When the acoustic pulse reflects from the input face, the peak diffraction efficiency increases dramatically. As the acoustic pulse reflects from the output face the peak diffraction efficiency is relatively weak, due to the absorption of the β solution.

Upon closer inspection, the behavior of the generated Pendellösung oscillations are not static over time. Figure 7.10 shows a time-resolved blow up of the acoustic pulse after 1, 1.5, 6.5, and 7 round trips in the crystal. During the early bounces, the

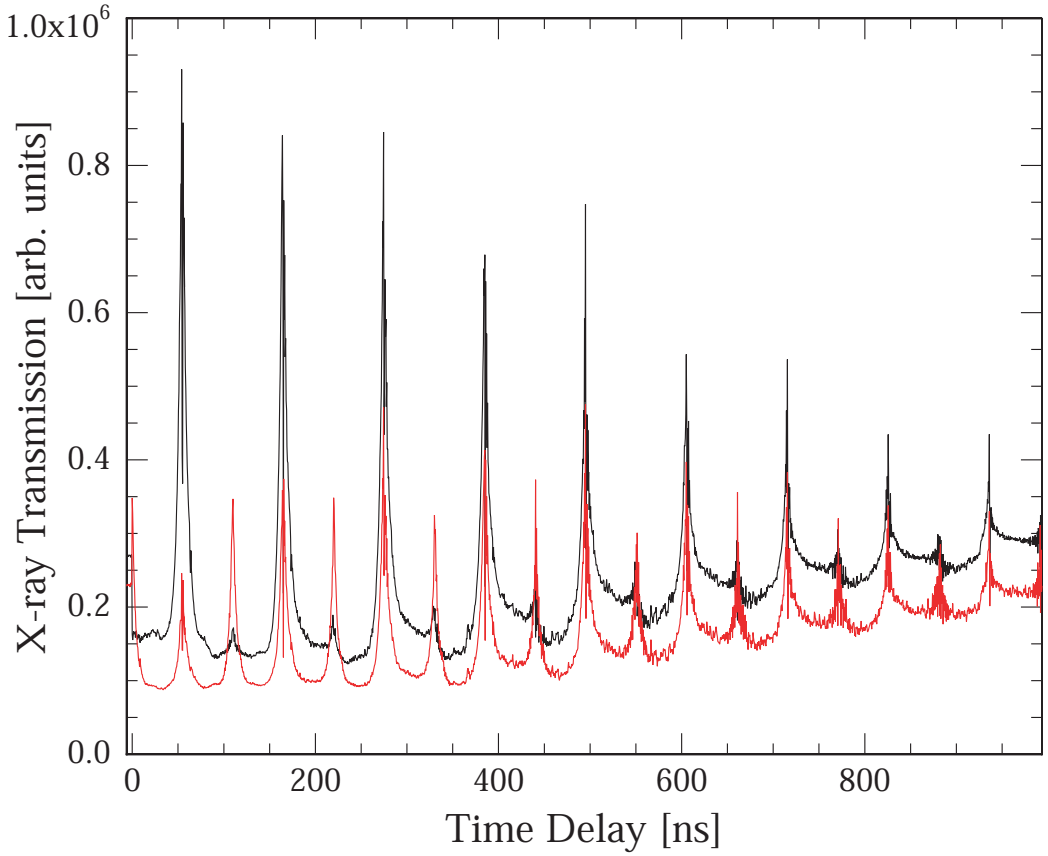

Figure 7.9: The Time-resolved Borrmann probe of an acoustic pulse launched from the output face of the Ge.

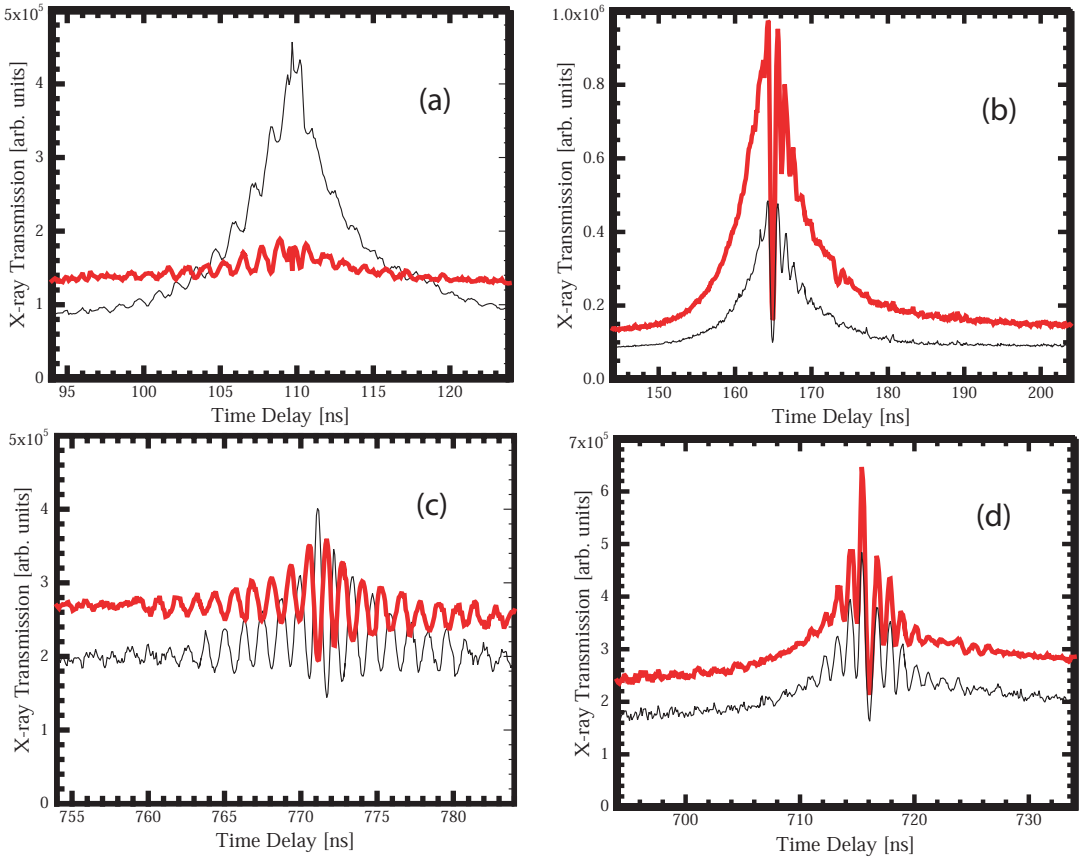

Figure 7.10: (a) temporal response after 1 round trip (b) 1.5 round trips (c) 7 round trips (d) 6.5 round trips.

observed Pendellösung oscillations do not appear to have great contrast as well as some temporally sharp features at the acoustic pulse reflection time. As the acoustic pulse undergoes many reflections, the contrast of the Pendellösung oscillations increases and the temporally sharp features are not observed. These two observations may have a number of causes, some physical some experimental.

First, the Bragg experiments revealed that the spectral components of the acoustic pulse appear to disperse over many bounces, leading to the attenuation of the high frequency components of the pulse. This dispersion of the acoustic pulse could possibly lead to an increased coupling of the dispersion surface due to the extended

spatial extent of the acoustic pulse, leading to larger Pendellösung oscillations. The dispersion could also reduce any 'fast' effects in the diffraction patterns since the high frequency components are severely attenuated.

Second, this effect could possibly be explained by the spatial walk off of the acoustic pulse. If the two crystal faces are not parallel, after many reflections the acoustic pulse could have travelled a significant distance in the transverse direction making a direct detection of the acoustic pulse by the x-rays impossible.

7.1.3 Acoustic Collisions

Although the x-rays diffract through the entire bulk of the crystal, the observational power of the asymmetric Laue reflection is limited by the absorption depth of the β solution. In Ge, this limitation prevents the direct observation of the strain pulse at depths deeper than $\sim 25\ \mu m$. The repopulation of the β solution deep within the bulk of the crystal can circumvent this problem. In static crystals, buried interfaces or lattice dislocations can repopulate the β solution after many absorption depths[11]. Launching a second acoustic pulse, counter-propagating with the first, a transient interface may allow the observation of a transient strain deep within the crystal bulk.

In figure 7.11 two counter propagating acoustic pulses are generated simultaneously from opposite faces. As expected, immediately after the initial lattice expansion an ultrafast energy transfer has taken place which decays quickly as the acoustic pulses travel into the center of the crystal. At a time delay of $\sim$ 27.5ns a Borrmann revival is seen. This time delay corresponds to the acoustic pulses travelling half way

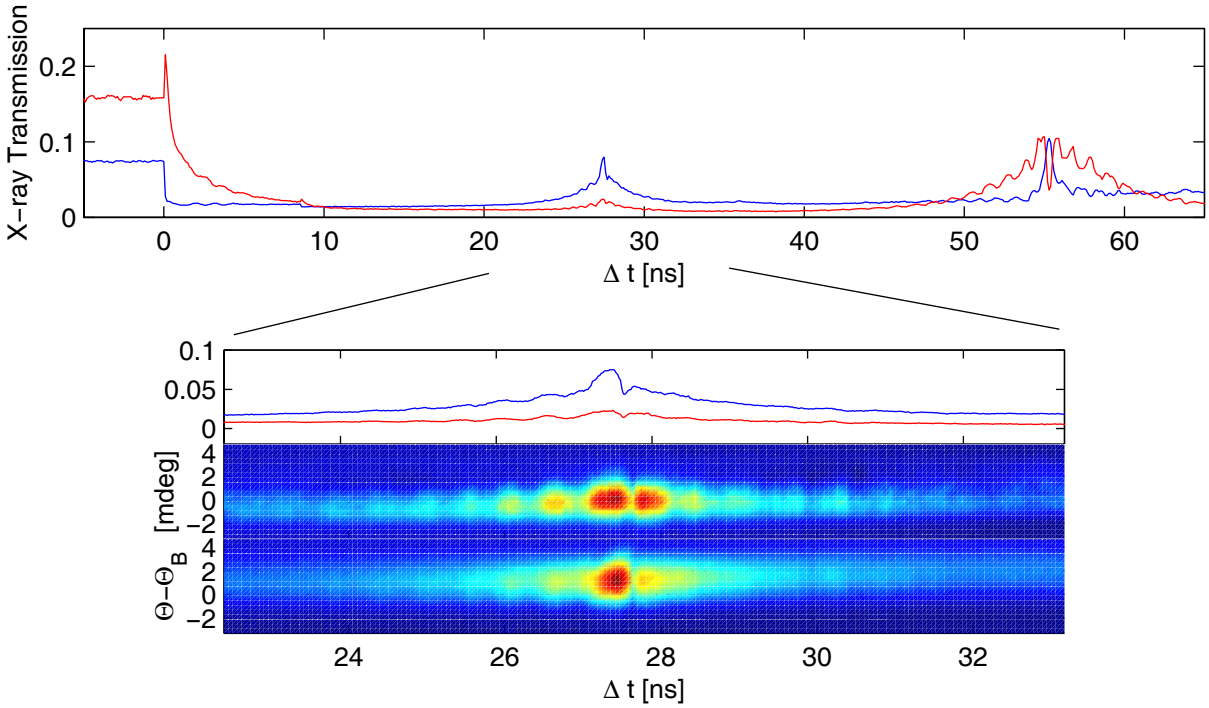

Figure 7.11: Time-resolved diffraction of the $20\overline{2}$ reflection in Ge. The angular blow up is the collision of two counter-propagating acoustic pulses. Adapted from [73].

through the crystal bulk[73].

Like before, the Borrmann revival has oscillations associated with the increase in x-ray transmission, however in this case the oscillation period is twice as frequent as compared to the single acoustic pulse excitation. The reason for the frequency doubling is because unlike the two crystal model introduced with the single acoustic pulse, there now is a three crystal model (figure 7.12). The three crystals are a single thin crystal contracting (expanding) at twice the speed of sound, sandwiched between two thick crystals expanding (contracting) at the speed of sound. Since the thin crystal is changing its thickness by twice the sound speed the Pendellösung oscillations oscillate at twice the frequency.

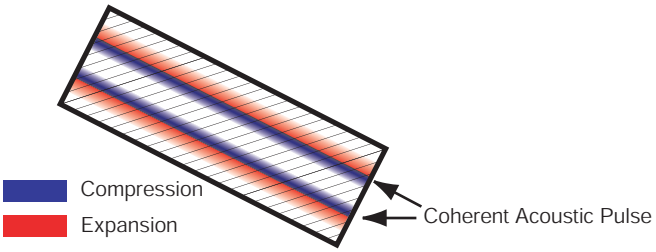

Figure 7.12: The three crystal model

7.2 What is the fast Mechanism?

In dynamical diffraction, the scale length of diffraction is given by the Pendellösung depth. The fast coherent transfer of energy, however, does not appear to correspond to acoustic pulse traversing the Pendellösung depth and thus is an unexpected physical phenomena. The use of other crystal species in the Laue geometry may shed light on the mechanism on the ultrafast transfer of x-ray energy. GaAs and InSb are ideal candidates due to their perfect crystal structure and their capability to generate large strain pulses with an ultrafast optical pulse. The major difference between the three semiconductors is the optical penetration depth; 100nm, 220nm, and $1\,\mu m$ for InSb, Ge, and GaAs respectively. In theory this will determine the central wavevector of the acoustic pulse.

7.2.1 Different Materials

The experiment was repeated using a $400\,\mu m$ thick piece of a 001 GaAs. Figure 7.13 shows data repeating the experiment using the $\overline{2}02$ reflection in GaAs. Like the Ge experiment, the acoustic pulse is generated on the output face of the crystal. Immediately after the acoustic pulse generation, a coherent transfer of energy is observed. The speed of the coherent switch is clearly longer than the x-ray pulse,

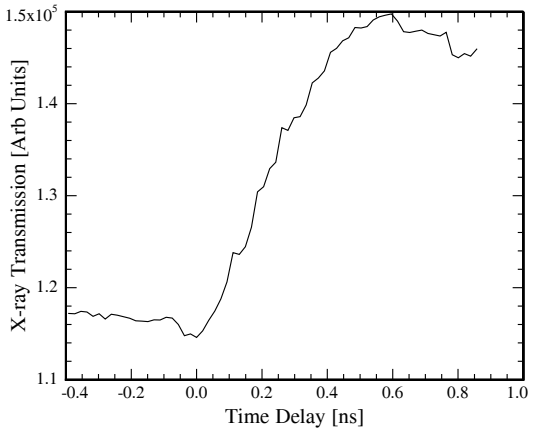

Figure 7.13: X-ray transmission as a function of optical pulse time delay of the $\overline{2}02$ asymmetric reflection in GaAs

$\sim$300ps.

The experiment was repeated with a $400\,\mu m$ 001 InSb (figure 7.14). Due to experimental constraints the acoustic pulse was generated on the input face of the crystal. Again as the acoustic pulse is generated x-rays are coherently transferred from one beam to another. However, like the Ge sample, the speed of the switch appears to be less than the x-ray pulse width.

A simple calculation of the timescale of x-ray diffraction using an acoustic impulse raises some questions of the mechanism of the ultrafast transfer of energy. The Pendellösung depth of all three materials is $\sim 5\,\mu m$ where the speed of sound is 4725m/s, 3400m/s, and 4820m/s for GaAs, InSb, and Ge in the 001 direction respectively. At the output face of the Ge and GaAs the propagating x-rays are purely α type. Due to boundary conditions, if an acoustic pulse is generated on the output face, the acoustic pulse must travel at least one quarter of a Pendellösung depth to have full transfer of energy from one beam to another. If the acoustic pulse

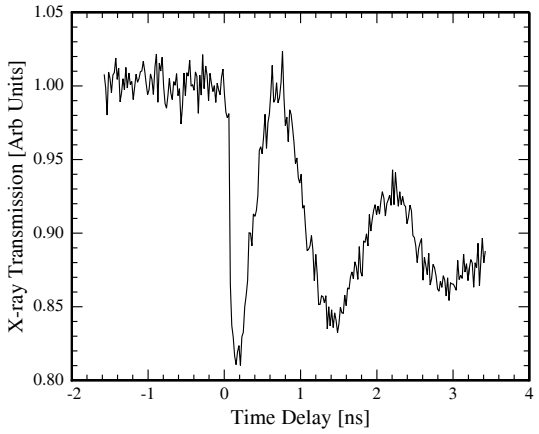

Figure 7.14: X-ray transmission as a function of optical pulse time delay for the $20\overline{2}$ asymmetric reflection in InSb.

is generated on the input face, as in the InSb case, the x-ray solution is an even distribution of α and β type. This means that the acoustic pulse must travel one half a Pendellösung depth to achieve a full transfer of energy.

In the GaAs case the propagation of the sound pulse through a quarter Pendellösung depth is consistent with the measured time scale. The Ge and InSb data, however, are not consistent with the sound speed and Pendellösung depth. This appears to indicate a supersonic transfer of energy.

7.2.2 Streak Camera Data

To properly diagnose the fast mechanism, an x-ray streak camera is used to detect picosecond changes in the diffracted x-ray intensity. The sweep speed of the streak plates limited the timing resolution to ∼5ps. Due to experimental constraints, the streak camera is only able to sample the forward diffracted beam. Using the $20\overline{2}$ reflection, the drop speed is measured for Ge and InSb single crystals.

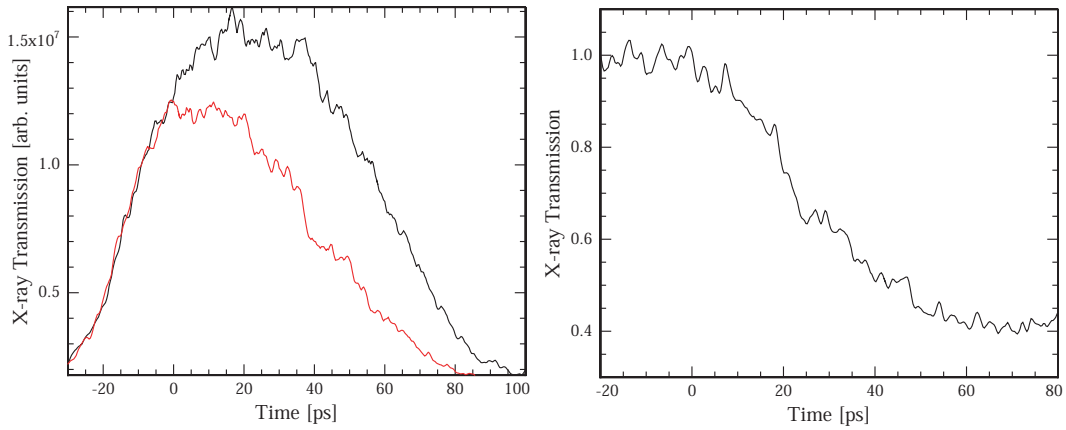

Figure 7.15: X-ray streak camera data of the transmission efficiency of the asymmetric $20\overline{2}$ reflection in Ge. The blue (dotted) curve is the undisturbed crystal, the red (solid) curve is the laser heated crystal.

Figure 7.15a illustrates the laser induced switching of the Ge single crystal on a sub bunch timescale. The black curve represents the temporal shape of the x-ray pulse through an undisturbed crystal. The red curve is the x-ray transmission signal through a crystal undergoing laser illumination. When the laser pulse arrives an immediate transfer of energy is apparent in the transmitted beam. The ratio of the two streaks illustrates the time dependence of the fast switch (figure 7.15b). Within 60 ps of illuminating the sample, 60% of the transmitted x-ray intensity is switched. The fall time of this process appears to be ∼25ps which, if we assume that the disturbance moves at the sound speed, represents a depth of ∼125nm or 2% of a Pendellösung depth. Diffracting from the opposite asymmetry, the rising edge of the population transfer can be measured. The rising edge appears to take place in a time consistent with the falling edge (figure 7.16).

As the incident optical fluence increases, the switching efficiency increases correspondingly (figure 7.17). This observation indicates that the efficiency of the fast

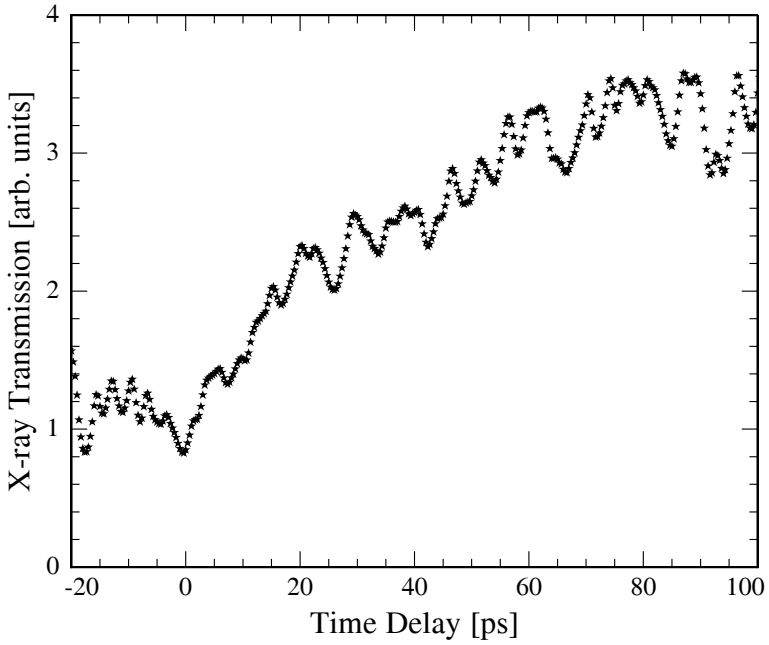

Figure 7.16: Streak camera data of the $\overline{2}02$ reflection in Ge.

switch is directly related to the amplitude of the generated strain.

The experiment was repeated for the $20\overline{2}$ reflection in InSb. Figure 7.18 shows the ratio of the laser induced effect to the undisturbed x-ray transmission. It is clear that the laser induced effect is significantly faster than the Ge sample though the efficiency is $\sim 30\%$. The x-ray transfer now appears to take place in $\sim$15ps. Again assuming that the transfer is due to an acoustic pulse, this would represent a crystal depth of $\sim$60nm or 1% of a Pendellösung depth.

It must be noted that in this case the drop is due to the front side excitation. In the Pendellösung model, when compared to the back side excitation, the acoustic pulse must travel twice as far to get a full rotation of the α, β basis. This could imply that if InSb was excited on the output face, the drop time could be as fast as

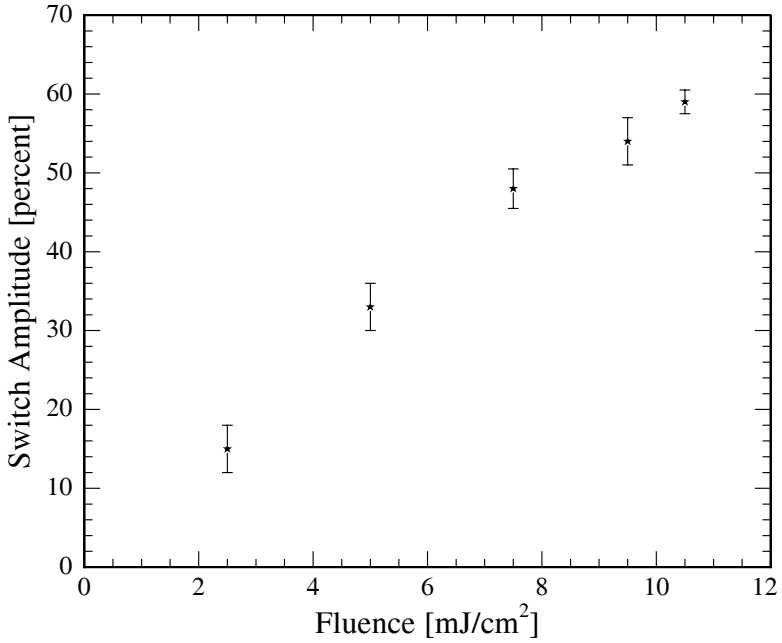

Figure 7.17: Switching efficiency as a function of optical fluence.

7ps.

If the fast switch can be described with dynamical diffraction, the switching mechanism must be related to the Pendellösung depth. For this to occur, the driving mechanism of the fast switch must be one or more of the following; the Pendellösung scale changes dynamically with the laser induced strain, a supersonic strain is generated at the time of the acoustic pulse, or strain depth is significantly different from the generally accepted values.

7.2.3 Change in Pendellösung depth

Dynamical diffraction predicts that the Pendellösung depth changes with the diffraction angle. Changing the diffraction condition dynamically will change the Pendellösung period over time. The Thomsen strain can effectively change the Laue

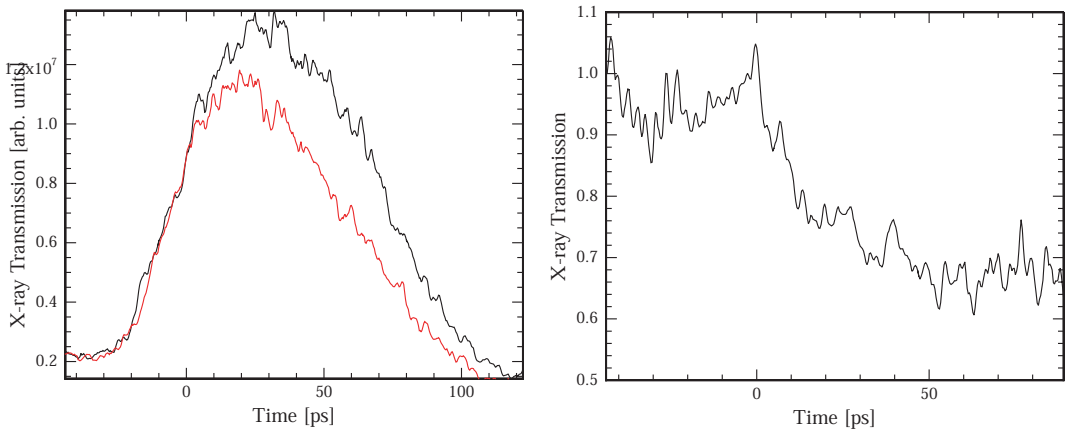

Figure 7.18: The ratio of the laser heated and undisturbed streak camera data using the asymmetric $20\overline{2}$ reflection in single crystal InSb.

Material	q (μm^{-1})	$\Delta\theta$[mdeg]	Effective Pendellösung	Speed
InSb	10	25.4	.48 μm	15 ± 5ps
Ge	4.5	11.6	.98 μm	25 ± 5ps
GaAs	1.2	3.1	3.9 μm	300 ± 50ps

Table 7.1: The change in the Pendellösung depth as a function of acoustic wavevector for InSb, Ge, and GaAs.

condition at the surface and thus the Pendellösung depth since the strain is parallel to the reciprocal lattice vector. There is some experimental evidence for this mechanism. The simple scattering relation $\Delta\theta \sim q/G \tan\theta_B \cos(\phi)$ shows that that the deviation of the diffraction angle is directly related to the momentum transfer. Assuming q is related directly to the optical penetration depth the position of the sideband can be calculated (table 7.1). There appears to be a relationship between the phonon wavevector and the drop speed.

However, there a few problems with this explanation. First, it was shown in chapter V that the effective initial strain depth in Ge is a couple of microns. This indicates that the central phonon wavevector is actually $0.5\,\mu m^{-1}$ rather than $4.5\,\mu m^{-1}$. This implies that the momentum of the acoustic pulse does not provide enough

change in the diffraction condition.

Second, in the Thomsen model of strain there is a stationary heated component that resides on the crystal surface. The stationary strain possesses the same wavevector components as the acoustic pulse, which could indicate that the heated region would change the diffraction condition enough to produce the necessary effect. However, after the acoustic pulse has propagated through one crystal thickness a Borrmann revival is observed. This implies that the wavevector components are not enough to change the diffraction condition to diffract out of the waveguide.

Finally, as the angle deviates from the Laue condition the efficiency of the transfer via the Pendellösung effect changes. Assuming a 10mdeg deviation from the peak of the rocking curve less than 10% of the x-ray energy is transferred from one beam to the other. This is in direct conflict with the observed transfer of up to 70% of the transmitted x-ray energy.

7.2.4 Shockwave

Another possible mechanism is the generation of a supersonic acoustic wave. Previous experiments have shown that an optical pulse with enough intensity can produce acoustic shocks in semi-conductors and metals. The generation of an acoustic shock could produce a strain wave a quarter Pendellösung period into the bulk within 20ps.

There is a significant problem with this mechanism. The Bragg geometry is sensitive to the arrival of any transient strain. The presence of a supersonic shock wave would be apparent by the change in the Bragg condition at a time not correspond-

ing to an integral number of acoustic round trips. The time dependent diffraction efficiency in the Bragg geometry does not show the effects of a supersonic acoustic wave.

7.2.5 Large Strain depths

The final possible method is the generation of acoustic strains at depths much larger than the optical penetration depth. This could be possible by the supersonic expansion of a dense electron-hole plasma. An ultrafast optical pulse has the ability to generate large dense electron-hole plasmas at the surface of semi-conductor crystals. This plasma would evolve on the timescale of diffusion, which if the plasma were dense enough, could explain the fast transfer of x-ray energy.

There is some experimental evidence to support this explanation. The time resolved Bragg diffraction in Ge appears to indicate the existence of the electron hold diffusion generating a very deep strain (see [25] and chapter V).

However, there is significant evidence which discounts this possibility. First, since the diffusion constant is directly related to the plasma density, the initial strain depth would be related to the optical fluence[43]. If the electron-hole plasma were very dense (which would be required to reach the Pendellösung scale) the strain depth is proportional to optical fluence. This would indicate that the timescale of the x-ray transfer would also be proportional to the incident optical fluence. However, the speed of the x-ray switch is observed to be independent with the incident optical fluence, which implies that the electron-hole plasma is not very dense and thus the strain would not be supersonic. The other problem is that the time resolved Bragg

diffraction in InSb does not appear to support a electron plasma diffusion model. This would indicate that the fast energy transfer is completely due to the strain predicted by the Thomsen model.

In the end, the generation mechanism may be a combination of the effects described above. The one observed effect that is not described by any of the proposed methods above is the dependence on the asymmetry angle (i.e. diffracted from the $20\overline{2}$ plane the transmitted beam goes down, diffracting from the $\overline{2}02$ plane the transmitted beam goes up). To fully resolve this mechanism it is necessary to study this effect in more detail.

CHAPTER VIII

Conclusions

This work demonstrates the strengths of time-resolved x-ray diffraction for the study of ultrafast lattice dynamics. The techniques developed in this thesis, in principle, can be extended to the study of more complicated and faster crystal dynamics. Future studies may include looking at higher frequency phonons (including optical phonons) and using the diffraction effects described in the previous chapters to study ultrafast dynamics in other systems.

8.1 High frequency acoustic phonons

The acoustic frequencies that are studied in this work are limited by the penetration depth of the laser. Due to the simplicity of the systems studied here, each crystal has a limited range of characteristic phonon frequencies that can be excited by the laser system ($\sim$40GHz). Recent experiments have extended this range with the use of surface transducers [3, 4, 5].

The optical absorption depth is reduced significantly if the crystal surface is coated with a thin layer of aluminum. The ultrafast generation of carriers inside the aluminum coating generates a large surface strain which will propagate into the

crystal substrate. Acoustic phonon frequencies up to 150GHz have been generated and studied with optical scattering techniques. Due to the large frequency components, acoustic pulse dispersion becomes very significant in these systems. The use of time-resolved x-ray diffraction in these systems may prove fruitful in the study acoustic pulse dispersion.

To study acoustic phonons with even larger frequencies requires more elaborate crystalline systems. Crystalline superlattices support the generation of coherent acoustic phonons, which possess frequencies as large as 1THz. The fundamental oscillation of the phonon ($q = 0$) is the vibration of the superlattice itself. The large wavevector of the crystalline superlattice is given to the acoustic phonon. There are two other modes which possess momentum components that are laser dependent ($q = \pm 2k_{laser}$).

If the laser momentum is large enough, sidebands will be generated on both the superlattice sideband as well as the main diffraction peak. Bragg diffraction could be very successful at detecting these phonons since the system can be engineered such that the sidebands are well off the diffraction peak. If the generated phonon has a wavevector large when compared to the spacing of the dispersion surface, Laue diffraction could also prove useful in the detection of these lattice vibrations.

Because acoustic phonons are the motion of the crystalline lattice planes the central oscillation frequency is ultimately limited by the sound speed of the material. Higher frequency lattice motion (1-40THz) is possible using optical phonons. The amplitude of the oscillations has been shown to be as large as 1% of the equilibrium

lattice spacing[36]. Although these oscillations are very large when compared to the equilibrium lattice spacing, optical phonons possess very little momentum making detection via x-ray diffraction difficult. There are two potential methods of detecting these large lattice vibrations with x-ray diffraction; changing the crystal structure factor and artificially increasing the optical phonon wave vector.

Since optical phonons are atomic motion within the unit cell, the structure factor of a given diffraction plane (and thus the strength of the x-ray diffraction) may change with the lattice vibration. Thus as the coherent phonon oscillates the diffraction efficiency will oscillate as well. For allowed diffraction peaks, a 1% lattice vibration changes the structure factor by about 1%. The use of forbidden or quasi-forbidden diffraction peaks may increase the visibility of the optical phonon oscillation. Since a forbidden diffraction peak requires perfect alignment of the atoms within the unit cell to remain forbidden, a 1% lattice vibration could change the structure factor of the forbidden reflection by many times. Even though the structure factor of a forbidden reflection may change greatly, the diffraction efficiency will still be quite small making phonon detection quite difficult. Using allowed reflections is for diffraction experiments is preferred.

Although it may still be possible for an allowed x-ray reflection to detect this lattice motion via a change in the structure factor, a larger phonon wavevector will increase the phonon contrast with the background substrate. By adding a spatial periodicity to the phonon, the effective wavevector of the optical phonon will increase. A transient superlattice can be created with two mutually coherent optical pulses

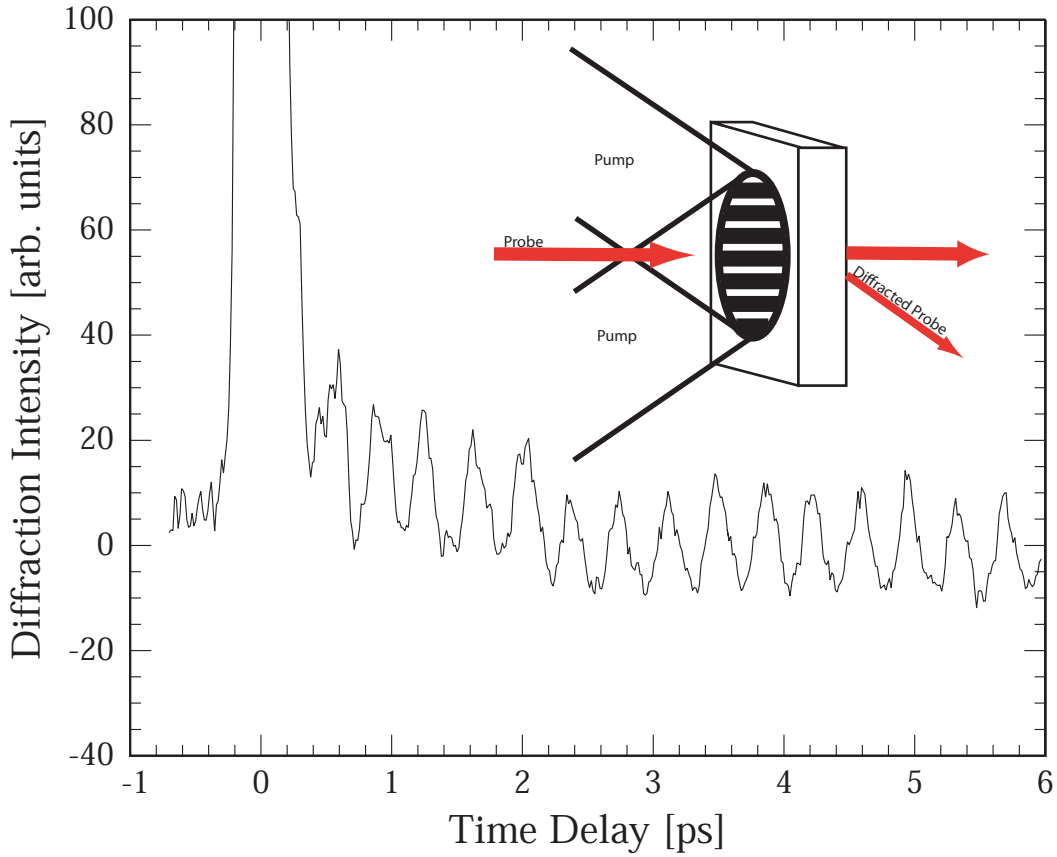

Figure 8.1: Optical phonons oscillations seen using a transient grating pump-probe technique

(see figure 8.1 inset)[74]. The two optical pulses can interfere causing an intensity grating to illuminate the surface. The periodicity of the lattice is determined by the vector difference of the two optical laser beams. The periodicity of the intensity grating can be transferred to an optical phonon if the pump lasers can generate a coherent optical phonon mode. Optical scattering experiments are able to detect these high wavevector phonon oscillations by diffracting from the phonon grating (see figure 8.1). X-rays can also diffract from this phonon grating making detection of optical phonons possible[75].

8.2 Other experiments

Ultrafast dynamics is not limited to crystalline motion. There are a number of systems which can be stimulated to produce ultrafast dynamics; including liquids and gasses [22, 76]. However x-ray pulses generated from a synchrotron currently can only measure dynamics as fast as a streak camera (∼1ps). The techniques developed in this work for the study of phonons can be utilized to generate sub-picosecond x-rays from a standard synchrotron source.

High wavevector acoustic phonons change the x-ray diffraction efficiency causing a change in the temporal profile of a diffracting x-ray pulse. In the Bragg geometry, acoustic phonons have been shown to generate sidebands on a 10 ps timescale[19, 31]. In the Laue geometry, the same acoustic phonon can be used to reduce the diffraction efficiency in ∼15ps. The combination of these two effects has the potential to generate a 20ps x-ray pulse from the 100ps synchrotron pulse.

These same effects can be utilized with coherent folded acoustic phonons. Since the acoustic phonon is coherent, two optical pulses can control the amplitude and duration of the acoustic phonon and thus the time dependence of the sideband can be controlled. The time dependence is limited to the phonon frequency, in this case ∼1ps. Generating high wavevector optical phonons by the method described above can potentially overcome the picosecond barrier [75].

APPENDICES

APPENDIX A

Impulsive Stimulated Raman Scattering

This is a derivation of a calculation of the ion displacement upon the excitation of a coherent optical phonon. This proof is based on the following papers [32, 8, 37, 38]. As with many calculations in Raman scattering many of the assumptions are just approximations.

The Greens function solution for the phonon amplitude in terms of the force on an ion is:

$$Q(z,t) \sim \frac{1}{\Omega_0} \int d\tau \sin(\Omega(t-\tau)) F(z,t) \tag{A.1}$$

where Ω_0 is the central frequency of the incident excitation field. In the cgs units, the force on an ion undergoing Raman transition is:

$$F(z,t) \sim -\frac{1}{8\pi^2} \int dt_1 dt_2 d\omega_1 d\omega_2 E(z,t_1) e^{-i\omega_1(t_1-t)} E^*(z,t_2) e^{i\omega_2(t_2-t} \Re_Q \tag{A.2}$$

where E_ω is the field exciting the Raman transition, $\Re_Q$ is the Raman susceptibility and can be defined in terms of the dielectric constant:

$$\Re_Q \sim \pm \frac{d\omega}{dQ} \left[\frac{\epsilon^*(\omega_1) - \epsilon(\omega_2)}{\omega_1 - \omega_2} \right] \tag{A.3}$$

where $\frac{d\omega}{dQ}$ is some deformation potential of the system which generally not known. Assuming the Raman tensor is susceptibility is constant over the band width of the excitation pulse:

$$\Re_Q \sim \pm \frac{d\omega}{dQ} \left[\frac{\epsilon^*(\omega) - \epsilon(\omega)}{\Omega} \right]_{\frac{\omega_1+\omega_2}{2}} \tag{A.4}$$

The complex dielectric constant of an ion as a function of excitation frequency is given by:

$$\epsilon(\omega) = \epsilon_1 + i\epsilon_2 = 1 + \frac{C}{\omega_0^2 - \omega^2 - 2i\omega\Gamma} \tag{A.5}$$

using this definition equation A.4 becomes:

$$\Re_Q \sim \frac{d\omega}{dQ} \left[\frac{\partial \epsilon_1}{\partial \omega} - \frac{2i\epsilon_2}{\Omega} \right] \tag{A.6}$$

In the special case of a semi-metal, the imaginary component of the dielectric constant is much larger the real component. This means that the Raman tensor can be approximated as:

$$\Re_Q \sim -\frac{d\omega}{dQ} \left[\frac{2i\epsilon_2}{\Omega} \right] \tag{A.7}$$

Taking the fourier transform of equation A.2 the force becomes:

$$F(z,\Omega) = -\frac{1}{\sqrt{8\pi}} \int d\omega E(z,\omega) E^*(z,\omega-\Omega) \Re_Q(\omega,\omega-\Omega) \tag{A.8}$$

Transforming this equation back:

$$F(z,t) = -\frac{1}{4\pi} \int d\Omega d\omega e^{i\Omega t} E(z,\omega) E^*(z,\omega-\Omega) \Re_Q(\omega,\omega-\Omega) \tag{A.9}$$

Thus equation A.1 becomes:

$$Q(z,t) \sim -\frac{1}{4\pi\Omega_0} \int d\tau d\Omega \sin(\Omega(t-\tau)) d\omega e^{i\Omega t} E(z,\omega) E^*(z,\omega-\Omega) \Re_Q(\omega,\omega-\Omega) \tag{A.10}$$

The incident electric field can be written as:

$$E(z,\omega) = \frac{2E_0(\omega)}{\eta\omega} e^{-i\omega nz/c} e^{-\alpha z/2} \tag{A.11}$$

where α is the absorption depth, $E_0(\omega)$ is the incident field, and $\eta(\omega) \equiv 1 + n(\omega) + ik(\omega)$.

Assuming that the phonon field is harmonic, the field amplitude can be written as:

$$Q(z,t) = \frac{1}{2i}\left[Q_+(z)e^{-i\Omega_0 t} - Q_-(z)e^{i\Omega_0 t}\right] \tag{A.12}$$

the phonon field at the surface can be reduced to:

$$Q_\pm(0) = \frac{2}{\Omega_0}\int \frac{E_0(\omega)E_0^*(\omega+\Omega_0)\Re_Q(\omega,\omega\pm\Omega_0)}{\eta(\omega)\eta(\omega\pm\Omega_0)} \tag{A.13}$$

Assuming that η_ω, $E(\omega)$, and $\Re_Q(\omega)$ is constant over the bandwidth of the excitation field then the field amplitude is:

$$|Q(0,0)| \sim \frac{E(\omega)E^*(\omega)\Re_Q(\omega)}{\Omega_0\eta^2(\omega)\tau_l} \tag{A.14}$$

If the material is a semi-metal, $\Re_Q$ may be substituted and thus:

$$|Q(0,0)| \sim \frac{E(\omega)E^*(\omega)}{\Omega_0\eta^2(\omega)\tau_l}\frac{\partial\omega}{\partial Q}\frac{2i\epsilon_2\hbar}{\hbar\Omega\tau_l} \tag{A.15}$$

The detection of the optical phonons in opaque material is usually accomplished by measuring the change in surface reflectivity.

$$\delta R \sim \frac{\partial R}{\partial Q}Q \tag{A.16}$$

$$\sim \frac{\partial R}{\partial \epsilon}(\omega)\frac{\partial \epsilon}{\partial \omega}(\omega)\frac{\partial \omega}{\partial Q}(\omega)Q \tag{A.17}$$

The total reflectivity change due to the phonon is:

$$\frac{\Delta R}{R} = \frac{\int d\omega \delta R |e_l(0,\omega)|^2}{\int d\omega R |e_l(0,\omega)|^2} \tag{A.18}$$

where $|e_l(0,\omega)|^2$ is the intensity of the optical probe. Assuming that the frequency spread of the probe pulse is small to any frequency dependent variable, the probe pulse can be approximated by a delta function. Making a change of variables ($dE = \hbar d\omega$) the two integrals can be solved and thus the normalized differential optical reflectivity is:

$$\frac{\Delta R}{R} \sim D \frac{\partial \omega}{\partial Q} Q\hbar \tag{A.19}$$

where $D = \frac{1}{R(E)} \frac{\partial R}{\partial \epsilon}(E) \frac{\partial \epsilon}{\partial E}(E)$.

In the specialized case of a semi-metal equations A.15 and A.19 can be combined to attain an approximate amplitude of the displacement of a specific atom in the unit cell.

$$Q^2 \sim \frac{E(\omega)E^*(\omega)}{\Omega_0 \eta^2(\omega)\tau_l} \frac{\partial \omega}{\partial Q} \frac{2i\epsilon_2}{\hbar\Omega\tau_l} \frac{\Delta R}{R} \frac{1}{D} \tag{A.20}$$

The displacement of an ion due to a phonon oscillation can be written in the form:

$$u_i(\Omega t) \sim \sqrt{\frac{V}{M_i}} [Q e^{-i\Omega t} + Q^* e^{i\Omega t}] \tag{A.21}$$

where V is the volume of the unit cell and M_i is the mass of the specific atom. Solving for u^2:

$$u^2 \sim \frac{\Delta R}{R} \frac{I_o (\frac{2i\epsilon_2}{\hbar\Omega})^2}{\epsilon \rho_m \Omega \tau_l D} \tag{A.22}$$

where I_o is the intensity of pump in $\frac{statvolt^2 s^2}{cm^2}$ and ρ_m is the density of the material in $\frac{g}{A^3}$. For bismuth, $\frac{2i\epsilon_2}{\hbar\Omega} \sim 10^3$ and $D \sim 10^{-2}$ this equation can be simplified to:

$$u^2 \sim \frac{\Delta R}{R} \frac{I_o 10^5}{|\epsilon| \rho_m \Omega \tau_l} \tag{A.23}$$

In practical experimental units:

$$u^2[\mathring{A}^2] \sim \frac{\Delta R}{R} \frac{I[\frac{mJ}{cm^2}]377}{\rho[\frac{amu}{\mathring{A}^3}]\nu[THz]|\epsilon|} \tag{A.24}$$

APPENDIX B

Deriving the Dispersion Surface

The Ewald construction provides a simple, yet effective method of predicting x-ray reflections. However, to model the response of an x-ray reflection when equation 3.2 is almost satisfied, we must solve Maxwell's equations inside the crystal. Generally solving Maxwell's equations inside a solid object is difficult, however, if we are dealing with a perfect crystalline body, we can solve for the field amplitudes in a straight forward manner. Batterman and Cole[50] provide a straight forward method of calculating the field amplitudes inside a crystal.

Maxwell's equations for the propagation of electro-magnetic waves can be written in the form:

$$\nabla \times \mathbf{E} = -\frac{\partial \mathbf{B}}{\partial t} \tag{B.1}$$

$$\nabla \times \mathbf{H} = \frac{\partial \mathbf{D}}{\partial t} \tag{B.2}$$

where:

$$\mathbf{D} = \epsilon_0(1+\psi)\mathbf{E} \tag{B.3}$$

where ψ is the complex dielectric constant. Assuming that we have a periodically varying index of refraction (as we do in a perfect crystal), we can write the solution

of the fields as a Bloch function[52]:

$$\mathbf{A} = \sum_H \mathbf{A}_H e^{i\omega t - 2i\pi \mathbf{k}_H \cdot \mathbf{r}} \tag{B.4}$$

where $\mathbf{A}$ can be any of the components of the electro-magnetic field ($\mathbf{D}$,$\mathbf{E}$, or $\mathbf{B}$). Placing this solution into equations B.1 and B.2 the field amplitudes can be solved.

Placing the solution for $\mathbf{E}$ and $\mathbf{B}$ into equation B.1 we find:

$$-i2\pi e^{i\omega t} \sum_H (\mathbf{K}_H \times \mathbf{E}_H) e^{-i2\pi \mathbf{K}_H \cdot \mathbf{r}} = i\omega e^{i\omega t} \sum_H \mathbf{B}_H e^{-i2\pi \mathbf{K}_H \cdot \mathbf{r}} \tag{B.5}$$

From the rules of orthogonality, the amplitudes of each Fourier component must be equal so that:

$$\mathbf{K}_H \times \mathbf{E}_H = \omega/(2\pi)\mathbf{B}_H \tag{B.6}$$

Repeating this process for equation B.2 we find that:

$$\mathbf{K}_H \times \mathbf{H}_H = -\omega/(2\pi)\mathbf{D}_H \tag{B.7}$$

Taking the cross product of $\mathbf{K}_H$ with both sides of equation B.6 and using the relationship found in equation B.7 the following set of equations are obtained:

$$\mathbf{K}_H \times (\mathbf{K}_H \times \mathbf{E}_H) = -\omega^2/(4\pi^2)\mathbf{D}_H \tag{B.8}$$

Since we have assumed that ψ is spatially periodic, we can break ψ into its fourier components.

$$\psi = \sum_H \psi_H e^{-i\pi n_H} \tag{B.9}$$

This transforms equation B.3 into:

$$\mathbf{D} = \epsilon_0 (1 + \psi_0 \mathbf{E}_H + \sum_{P \neq H} \psi_{H-P} \mathbf{E}_P) \tag{B.10}$$

Substituting this equation into equation B.8 we find a system the following system of equations:

$$[k^2(1+\psi_0) - (\mathbf{K}_H \cdot \mathbf{K}_H)]\mathbf{E}_H + k^2 \sum_{P \neq H} \psi_{H-P}\mathbf{E}_P + (\mathbf{K}_H \cdot \mathbf{E}_H)\mathbf{K}_H = 0 \qquad \text{(B.11)}$$

This system of equations is completely general if we neglect the time dependence of the fields. Assuming that we are near a strong reflection and that only two fields are significant, we can further simplify this equation into 2 coupled linear equations.

$$(k^2(1+\psi_0) - (\mathbf{K}_0 \cdot \mathbf{K}_0))\mathbf{E}_0 + k^2 P\psi_H \mathbf{E}_H = 0 \qquad \text{(B.12)}$$

$$k^2 P\psi_H \mathbf{E}_0 + (k^2(1+\psi_0) - (\mathbf{K}_H \cdot \mathbf{K}_H))\mathbf{E}_H = 0 \qquad \text{(B.13)}$$

where $\mathbf{K}_0 \cdot \mathbf{K}_0 = 2\Theta$, $P = 1, \cos 2\Theta$ if the x-rays are σ or π polarized respectively and $\psi_{0,H}$ is defined in equations D.3 and D.4. This system of equations only has a solution if the following determinate is equal to zero:

$$\begin{vmatrix} k^2(1+\psi_0) - (\mathbf{K}_0 \cdot \mathbf{K}_0) & k^2 P\psi_H \\ k^2 P\psi_H & k^2(1+\psi_0) - (\mathbf{K}_H \cdot \mathbf{K}_H) \end{vmatrix} = 0 \qquad \text{(B.14)}$$

To help solve this determinant we introduce two variables $\xi_{0,H}$

$$\xi_0 \equiv (\mathbf{K}_0 \cdot \mathbf{K}_0)^{0.5} - k(1 + \frac{1}{2}\psi_0) \qquad \text{(B.15)}$$

$$\xi_H \equiv (\mathbf{K}_H \cdot \mathbf{K}_H)^{0.5} - k(1 + \frac{1}{2}\psi_0) \qquad \text{(B.16)}$$

Physically these two variables represent the difference between the wavevectors of the two wave solutions and the incident wave vector corrected for the average index of refraction. Using this formalism, the equation B.14 is zero when:

$$\xi_0 \xi_H = \frac{1}{4} k^2 P^2 \psi_H \psi_{\bar{H}} \qquad \text{(B.17)}$$

This solution to the x-ray wave equation is referred to as the dispersion surface.

APPENDIX C

Propagating Field Solutions In the Laue Geometry

The x-ray dispersion surface provides an elegant method of determining the propagating solutions to the x-ray wave equation (see [50] for more details on this section). The following equation is the mathematical representation of the x-ray dispersion surface assuming that there is only two wavefields inside the crystal.

$$\xi_0 \xi_H = \frac{1}{4} k^2 P^2 \psi_H \psi_{\bar{H}} \tag{C.1}$$

where:

$$\xi_0 \equiv (\mathbf{k}_0 \cdot \mathbf{k}_0)^{0.5} - k(1 + \frac{1}{2}\psi_0) \tag{C.2}$$

$$\xi_H \equiv (\mathbf{k}_H \cdot \mathbf{k}_H)^{0.5} - k(1 + \frac{1}{2}\psi_0) \tag{C.3}$$

k is the wavevector of the incident light, and P=1,$\cos 2\theta$ depending on the polarization of the x-ray field. As the crystal orientation changes, ξ_0 and ξ_H will also change accordingly. Using some simple assumptions and geometry, an analytic solution for the angular dependence of $\xi_{0,H}$ may be obtained.

All of the angular dependence is represented with the complex wavevectors of the particular solutions. If it is assumed that the magnitude of the real parts of $\mathbf{k}_{0,H}$ are

much larger than the complex component then:

$$\mathbf{k}_{0,H} \cdot \mathbf{k}_{0,H} \sim \ (k^{'}_{0,H})^2 - 2ik^{'}_{0,H}k^{''}_{0,H}\cos\beta \tag{C.4}$$

where $\cos\beta$ is the angle between $\mathbf{k}^{'}$ and $\mathbf{k}^{''}$. Substituting this value into the equations for ξ:

$$\xi_0 \ \simeq \ k^{'}_0 - k^{''}_0\cos\beta_{0,H} - k(1+\frac{1}{2}\psi_0) \tag{C.5}$$

$$\xi_H \ \simeq \ k^{'}_H - k^{''}_H\cos\beta_{0,H} - k(1+\frac{1}{2}\psi_0) \tag{C.6}$$

Recalling figure 3.3, if it is assumed that $\overline{P0}$ and $\overline{PH}$ are in approximately the same direction as k and k_H, then:

$$k^{'}_0 \ \simeq \ k - q\mathbf{n}\cdot\mathbf{s}_0 \tag{C.7}$$

$$k^{'}_H \ \simeq \ \overline{PH} - q\mathbf{n}\cdot\mathbf{s}_H \tag{C.8}$$

where $\mathbf{q}$ is the vector between P and the tie point, $\mathbf{s}$ is the unit vector along the 0 or H directions, and $\mathbf{n}\cdot\mathbf{s}_{0,H} \equiv \gamma_{0,H}$. Noting that:

$$\overline{PH} = k - \overline{LP}\sin 2\theta = k - k\Delta\theta\sin 2\theta \tag{C.9}$$

(where $\overline{LP}/k \ \equiv \ \Delta\theta$) and assuming that $\cos\beta_{0,H} \ \sim \ \gamma$ then the explicit angular dependence of $\xi_{0,H}$ can be written.

$$\xi_0 \ = \ \frac{1}{2}k\Gamma F_0 - qk\gamma_0 \tag{C.10}$$

$$\xi_H \ = \ \frac{1}{2}k\Gamma F_H - qk\gamma_0 - k\Delta\theta\sin 2\theta \tag{C.11}$$

Using equation 3.8 we can eliminate q and have a solution for $\xi_{0,H}$ as a function of

diffraction angle:

$$\xi_0 = 0.5k|P||b|^{0.5}\Gamma[F_H F_{\overline{H}}]^{0.5}[\eta \pm (\eta^2 + \frac{b}{|b|^{0.5}})^{0.5}] \quad \text{(C.12)}$$

$$\xi_H = 0.5k|P|\frac{\Gamma}{|b|^{0.5}}[F_H F_{\overline{H}}]^{0.5}[\eta \pm (\eta^2 + \frac{b}{|b|^{0.5}})^{0.5}]^{-1} \quad \text{(C.13)}$$

Using the surface boundary conditions and the solution for $\xi_{0,H}$ the propagating field solutions can be solved. If the crystal is in the Laue geometry ($b > 0$), the angular deviation of the crystal, η (see equation 3.13), can be rewritten into the form:

$$\eta \equiv \sinh \nu \quad \text{(C.14)}$$

This form simplifies $\xi_{0,H}$ to:

$$\xi_0 = 0.5k|P||b|^{0.5}\Gamma[F_H F_{\overline{H}}]^{0.5}e^{\pm\nu} \quad \text{(C.15)}$$

$$\xi_H = 0.5k|P|\frac{\Gamma}{|b|^{0.5}}[F_H F_{\overline{H}}]^{0.5}e^{\pm\nu} \quad \text{(C.16)}$$

Combining equation 3.16 with the solution for ξ we find:

$$\frac{E_H}{E_0} = \mp\left(\frac{|P||b|^{0.5}}{P}\right)\frac{[F_H F_{\overline{H}}]^{0.5}}{F_{\overline{H}}}e^{\pm\nu} \quad \text{(C.17)}$$

The sign of the equation depends on which branch the tie point is located on. In the Laue geometry the initially boundary conditions are that all of the x-rays are in the forward direction:

$$E_0 = E_{0\alpha} + E_{0\beta}$$

$$0 = E_{H\alpha} + E_{H\beta}$$

Using the boundary conditions along with the ratio for $\frac{E_H}{E_0}$ the following initial fields

are found:

$$\begin{aligned}
E_{0\alpha} &= E_i \frac{e^{-\nu}}{2\cosh\nu} \\
E_{0\beta} &= E_i \frac{e^{\nu}}{2\cosh\nu} \\
E_{H\alpha} &= -E_i \left(\frac{|P||b|^{0.5}}{P}\right) \frac{[F_H F_{\overline{H}}]^{0.5}}{F_{\overline{H}}} \frac{1}{2\cosh\nu} \\
E_{H\beta} &= E_i \left(\frac{|P||b|^{0.5}}{P}\right) \frac{[F_H F_{\overline{H}}]^{0.5}}{F_{\overline{H}}} \frac{1}{2\cosh\nu}
\end{aligned}$$

Using these coefficients the propagating wave solutions are determined:

$$E_{0\alpha} = CE_0 e^{-\nu} e^{-2\pi i((K'_{0\alpha} + iK''_{0\alpha})\cdot r)} \tag{C.18}$$

$$E_{H\alpha} = -CDE_0 e^{-2\pi i((K'_{H\alpha} + iK''_{H\alpha})\cdot r)} \tag{C.19}$$

$$E_{0\beta} = CE_0 e^{-\nu} e^{-2\pi i((K'_{0\beta} + K''_{0\beta})\cdot r)} \tag{C.20}$$

$$E_{H\beta} = CDE_0 e^{-2\pi i((K'_{H\beta} + iK''_{H\beta})\cdot r)} \tag{C.21}$$

where:

$$\begin{aligned}
C &= \frac{e^{2\pi i v t}}{2\cosh\nu} \\
D &= \frac{|P|}{P}|b|^{0.5}\frac{[F_H F_{\overline{H}}]^{0.5}}{F_H}
\end{aligned}$$

APPENDIX D

Deriving the Takagi-Taupin Equations

The following proof is modelled after Taupin's original paper[55] deriving the differential equations that define dynamical diffraction theory. A similar proof was published by Takagi[54] and some of the steps in this proof have been influenced from that paper.

To calculate the wave fields diffracting from a perfect or almost perfect crystal, one must take into account the periodically varying index of refraction inside the crystal. To determine the magnitude of the diffracted waves we will solve the wave equation inside the crystal. The wave equation inside the crystal is:

$$\nabla \times \nabla \times (1 - \psi)\mathbf{D} = \frac{4\pi^2}{\lambda^2}\mathbf{D} \tag{D.1}$$

where

$$(1 - \psi)\mathbf{D} = \epsilon_0 \mathbf{E}$$

and where ψ is a spatially varying dielectric function defined by

$$\psi = \sum_H \psi_H e^{-ie\pi n_H} \tag{D.2}$$

and

$$\psi_0 = -\frac{\lambda^2 r_e}{\pi V} F_0 \tag{D.3}$$

$$\psi_H = -\frac{\lambda^2 r_e}{\pi V} F_H \tag{D.4}$$

The solutions for the wave fields are generally complicated, but since we are in a regime of a periodic dielectric constant, the displacement fields are defined by Bloch waves of the form:

$$\mathbf{D} = \sum_H \mathbf{D}_H e^{i\omega t - 2i\pi k} \tag{D.5}$$

Thus

$$(1-\psi)\mathbf{D} = e^{i\omega t} \sum_H \mathbf{Q}_H e^{-i2\pi\Phi_H} \tag{D.6}$$

where

$$\mathbf{Q}_H = \mathbf{D}_H - \sum_L \psi_{H-L}\mathbf{D}_L \tag{D.7}$$

$$\Phi_H = \mathbf{k}\cdot\mathbf{r} - \mathbf{G}\cdot\mathbf{u} \tag{D.8}$$

where $\mathbf{u}$ represents the positions of the atoms away from equilibrium. In this term, the strain or lattice defect may be taken into account. By placing equations D.7 and D.8 into the wave equation, one can solve for the amplitude of the waves $\mathbf{D}_{0,H}$.

To help solve for the field amplitudes, we use the vector identity:

$$\nabla \times \nabla \times \mathbf{A} = \nabla(\nabla \cdot \mathbf{A}) - \nabla^2 \mathbf{A}$$

Also expressed as:

$$\nabla \times \nabla \times A_i = \frac{\partial^2 A_k}{\partial x_i \partial x_k} - \frac{\partial^2 A_i}{\partial x_k \partial x_k} \tag{D.9}$$

Using this identity in conjunction with the Bloch fields, the wave equation can be simplified to a set of coupled differential equations.

First we solve the wave equation by solving for the left side of equation D.1. Using the vector identity described above we can simplify the equations. Putting the Bloch solution into the first half of equation D.9, we find that:

$$\begin{aligned}\frac{\partial^2(1-\psi)D_k}{\partial x_i \partial x_k} &= \frac{\partial}{\partial x_i}(e^{-i2\pi\Phi_H}\frac{\partial Q_{Hk}}{\partial x_k} - i2\pi Q_{Hk}K_{Hk}e^{-i2\pi\Phi_H}) && \text{(D.10)}\\ &= \frac{\partial^2 Q_{Hk}}{\partial x_i \partial x_k} - i2\pi\frac{\partial Q_{Hk}}{\partial x_k}K_{Hi} - i2\pi\frac{\partial Q_{Hk}}{\partial x_i}K_{Hk} \\ &\quad -4\pi^2 Q_{Hk}K_{Hk}K_{Hi} - i2\pi Q_{Hk}\frac{\partial K_{Hk}}{\partial x_i} && \text{(D.11)}\end{aligned}$$

where

$$\begin{aligned}\frac{\partial^2 Q_{Hk}}{\partial x_i \partial x_k} &= \nabla(\nabla\cdot\mathbf{Q})\\ \frac{\partial Q_{Hk}}{\partial x_k}K_{Hi} &= K_H\nabla\cdot\mathbf{Q}_H\\ Q_{Hk}K_{Hk}K_{Hi} &= (K_H\cdot Q_H)K_H\\ \frac{\partial Q_{Hk}}{\partial x_i}K_{Hk} + Q_{Hk}\frac{\partial K_{Hk}}{\partial x_i} &= -\nabla(K_H\cdot Q_H)\end{aligned}$$

The second half of equation D.9 is then very similar:

$$\begin{aligned}\frac{\partial^2(1-\psi)D_i}{\partial x_k \partial x_k} &= \frac{\partial}{\partial x_k}(e^{-i2\pi\Phi_H}\frac{\partial Q_{Hi}}{\partial x_k} - i2\pi Q_{Hi}K_{Hk}e^{-i2\pi\Phi_H}) && \text{(D.12)}\\ &= \frac{\partial^2 Q_{Hi}}{\partial x_k \partial x_k} - i2\pi\frac{\partial Q_{Hi}}{\partial x_k}K_{Hk} - i2\pi\frac{\partial Q_{Hi}}{\partial x_i}K_{Hk} \\ &\quad -4\pi^2 Q_{Hi}K_{Hk}K_{Hk} - i2\pi Q_{Hi}\frac{\partial K_{Hk}}{\partial x_k} && \text{(D.13)}\end{aligned}$$

where

$$\begin{aligned}
\frac{\partial^2 Q_{Hi}}{\partial x_k \partial x_k} &= \nabla^2 \mathbf{Q} \\
\frac{\partial Q_{Hi}}{\partial x_k} K_{Hk} &= K_H \frac{\partial Q_H}{\partial r} \\
Q_{Hi} K_{Hk} K_{Hk} &= K_H^2 Q_H \\
Q_{Hi} \frac{\partial K_{Hk}}{\partial x_k} &= Q_H \nabla K_H
\end{aligned}$$

Taking the difference of equation D.11 and D.13 we can solve for the left side of equation D.1:

$$\begin{aligned}
\nabla \times \nabla \times (1-\psi)\mathbf{D} &= \sum_H e^{-i2\pi\Phi_H}(4\pi^2(K_H^2 \mathbf{Q}_H - (K_H \cdot Q_H)K_H) \\
&\quad + i4\pi K_H \frac{\partial Q_H}{\partial r} - i2\pi\nabla(K_H \cdot Q_H) - i2\pi K_H \nabla \cdot \mathbf{Q}_H \\
&\quad + i2\pi Q_H \nabla K_H - \nabla^2 \mathbf{Q} + \nabla(\nabla \cdot \mathbf{Q})) \qquad \text{(D.14)}
\end{aligned}$$

Combining this result with the right side of equation D.1 a solution for the field amplitudes may be obtained. Thus the full wave equation looks something like:

$$\frac{4\pi^2}{\lambda^2} \sum_H \mathbf{D}_H e^{-i2\pi\Phi_H} = \sum_H (...) e^{-i2\pi\Phi_H} \qquad \text{(D.15)}$$

Using Fourier's trick, the coefficients of each of the fourier components are equal:

$$(...) - \frac{4\pi^2}{\lambda^2} \mathbf{D}_H = 0$$

Taking the dot product of both sides with $\mathbf{Q}_H$ we find that following equation holds:

$$\begin{aligned}
0 &= 4\pi^2(K_H^2 Q_H^2 - K_0^2(\mathbf{D}_H \cdot \mathbf{Q}_H) - (K_H \cdot Q_H)^2) + i2\pi K_H \nabla Q_H^2 \\
&\quad - i2\pi \mathbf{Q}_H \cdot \nabla(K_H \cdot Q_H) - i2\pi \mathbf{Q}_H \cdot K_H \nabla \cdot \mathbf{Q}_H \\
&\quad + i2\pi Q_H^2 \nabla K_H - \mathbf{Q}_H \cdot \nabla^2 \mathbf{Q} + \mathbf{Q}_H \cdot \nabla(\nabla \cdot \mathbf{Q}) \qquad \text{(D.16)}
\end{aligned}$$

By substituting equation D.7 into the $\mathbf{D}_H$ term the entire equation can be expressed completely by $\mathbf{Q}_H$.

$$K_0^2(\mathbf{D}_H \cdot \mathbf{Q}_H) = K_0^2\mathbf{Q}_H^2 + K_0^2 \sum_L \psi_{H-L}\mathbf{D}_L \cdot \mathbf{Q}_H \tag{D.17}$$

Combining the left side of this equation with the first term in equation D.16, we find:

$$K_H^2\mathbf{Q}_H^2 - K_0^2\mathbf{Q}_H^2 = (K_H^2 - K_0^2)\mathbf{Q}_H^2$$

Using the law of cosines:

$$K_H^2 = H^2 + K_0^2 - 2H \cdot K_H$$

and defining the function

$$\alpha_H \equiv \lambda^2(G^2 - 2K_0 \cdot G) \tag{D.18}$$

$$2(\Theta - \Theta_B)\sin(2\Theta_B) \tag{D.19}$$

we find that

$$K_H^2\mathbf{Q}_H^2 - K_0^2\mathbf{Q}_H^2 = \alpha_H K_0^2\mathbf{Q}_H^2 \tag{D.20}$$

By substituting this result into equation D.16, we find:

$$\begin{aligned} 0 = {} & 4\pi^2(\alpha_H K_0^2\mathbf{Q}_H^2 - K_0^2 \sum_L \psi_{H-L}\mathbf{D}_L \cdot \mathbf{Q}_H - (K_H \cdot Q_H)^2) \\ & + i2\pi K_H \nabla Q_H^2 - i2\pi \mathbf{Q}_H \cdot \nabla(K_H \cdot Q_H) - i2\pi \mathbf{Q}_H \cdot K_H \nabla \cdot \mathbf{Q}_H \\ & + i2\pi Q_H^2 \nabla K_H - \mathbf{Q}_H \cdot \nabla^2\mathbf{Q} + \mathbf{Q}_H \cdot \nabla(\nabla \cdot \mathbf{Q}) \end{aligned} \tag{D.21}$$

This equation is completely general for any type of incoming wave front or any strained crystal. However, equation D.21 is very complicated to integrate thus the

field amplitudes are very difficult to calculate. By making some simple physical constraints we can greatly reduce the complication of this equation.

First we assume that any strain in the crystal is macroscopic in its origin. That is, the crystal is almost perfect allowing us to make the simplification that only the 1st order terms are important and that $\nabla K_H \sim 0$[54]. We will also assume that since the crystal is almost perfect, that K_H is almost perpendicular to Q_H such that $K_H \cdot Q_H \sim 0$. Making these assumptions we find that equation D.21 reduces to:

$$4\pi^2(\alpha_H K_0^2 \mathbf{Q}_H^2 - K_0^2 \sum_L \psi_{H-L} \mathbf{D}_L \cdot \mathbf{Q}_H) + i2\pi K_H \nabla Q_H^2 = 0 \tag{D.22}$$

If the dielectric constant is much smaller than 1 (typically $\psi \sim 10^-5$), then $Q_H \sim D_H$ and the equation above reduces to:

$$4\pi^2(\alpha_H K_0^2 \mathbf{D}_H^2 - K_0^2 \sum_L \psi_{H-L} \mathbf{D}_L \cdot \mathbf{D}_H) + i2\pi K_H \nabla D_H^2 = 0 \tag{D.23}$$

Defining $\mathbf{D}_L \cdot \mathbf{D}_H \equiv D_L D_H \cos\gamma$ and dividing through by $4\pi^2 K_0^2$ the equation becomes:

$$\alpha_H D_H - \sum_L \psi_{H-L} D_L \cos\gamma + \frac{i\lambda^2}{2\pi} 2K_H \nabla D_H = 0 \tag{D.24}$$

where $\cos\gamma = 1$ when the x-ray polarization is in the plane of incidence and $\cos\gamma = \cos 2\theta$ when the x-ray polarization is out of the plane of incidence.

This is the fundamental system of equations that describe dynamical diffraction theory. In general the sum is infinite so that calculating the fields is nontrivial. However, if one is in a region where there are only two strong fields (i.e. near a Bragg peak) and the x-ray polarization is in the plane of incidence the system can

be simplified further:

$$\frac{i\lambda}{\pi}\frac{\partial D_H}{\partial x_H} = \psi_0 D_H + \psi_H D_0 - \alpha_H D_H \quad \text{(D.25)}$$

$$\frac{i\lambda}{\pi}\frac{\partial D_0}{\partial x_0} = \psi_0 D_0 + \psi_H D_H \quad \text{(D.26)}$$

where

$$r = x_0 s_0 + x_H s_H$$

$$s_0 = \lambda K_0$$

$$s_H = \lambda K_H$$

This system of equations is known as the Takagi-Taupin equations for dynamical diffraction.

APPENDIX E

Time-Resolved Dynamical Diffraction Program

This program is an adaptation of the algorithm described in chapter III. This program is written for use in the programming language of MATLAB.

Main Program

```
    %Program By Matt DeCamp 2000
%Algorithm found in C.R. Wie et.al. J. Appl. Phys vol. 59 pg 3743
% globals and a few touches added by d reis if blame be necc.

    %define some constants
plank=6.626e-34; light=3e8; ev=1.6e-19;
re=2.82e-15; %classical electron radius [m]
fwhmFact=2*sqrt(2*log(2)); % rms = fwhmFact* fwhm
    %define and set global variables and others
global gEnergy gLambda
gEnergy=10000; %Energy of the x-ray
gLambda=plank*light/ev/gEnergy; %wavelength of the x-ray

    %scattering factors
global fin fsb;
fGe=13.0186+i*0.613322;fin=fGe;fsb=fGe; %scat. Ge 10kV put into InSb for simp.
%fin=43.185+i*3.3742; %scattering factors for Indium for 10 kV @10 deg
%fsb=44.6864+i*3.8673; %scattering factors for antimony for 10kV@10 deg

    %polarizabilities, directions, etc.
global gPsi01 gPsi02 gPsiH1 gPsiH2; global gG gK gGamma0 gGammaH gBeta;
global gA0 gVol; global gThetaB gSin2QB gTanQB;
    %gA0=6.4784e-10; %a0 for InSb
%gVol=2.72e-28; %unit cell volume
```

```
gA0=5.6578e-10; %Germanium
gVol=gA0^3;
gPsi01=18.163e-6; % Average index for Germanium at 10keV
gPsi02=3.51e-7;
%gPsi01=2.014e-5; %Average Index for InSb at 10keV
%gPsi02=14.64e-7;
    %calculate complex index for the Bragg
orientation=[4 0 0]; %hkl
[Freal, Fimag]=structurefactor2(orientation)
gPsiH1=-re/pi*gLambda^2/gVol*Freal; %get from structure factor to psi
gPsiH2=-re/pi*gLambda^2/gVol*Fimag;
%sinChi=1; %Normal Polarization
sinChi=cos(2*gThetaB); %P-Polarization
gPsiH1=abs(gPsiH1)*sinChi;
gPsiH2=abs(gPsiH2)*sinChi;

    %currently there is no asymmetry here
gGamma0=sin(gThetaB); %cosine of the incident wave
gGammaH=sin(gThetaB); %cosine of the diffracted wave
gK=gPsiH2/gPsiH1; %k-factor
gBeta=gGamma0/gGammaH; %this is the asymmetry angle
gG=-(1+gBeta)*gPsi02/2/abs(gPsiH1)/sqrt(gBeta);

    %other globals
global gRes gNumber gAlpha0;
gRes = (0.0001*pi/180.0)^-1; %1/res = deltatheta step size in Rads
gNumber = 300; %number of angular steps
scaledegrees=180/pi/gRes; % convert to degrees

    %these are the stepsizes
timesteps=50; %in ps
distancesteps=20; %in nm;
gAlpha0=[-2*gNumber/3:gNumber/3]*(-2)*gSin2QB/gRes; %angular offset
gNumber=size(gAlpha0,2); %just in case gNumber originally even

    fluence=input('what is the incident fluence (mJ/cm^2)? n'); %mj/cm^2

    %initialize the time dependent strain function
%strainfun = timestrain(fluence,timesteps,distancesteps,0); %InSb strain function
strainfun = Getimestrain(fluence,timesteps,distancesteps,0); %Ge strain function

    %These are the axis scales
subplot(2,2,1);
[time,distance]=size(strainfun);
```

```
xscale=-gAlpha0*scaledegrees/gSin2QB/2*gRes;
xscale2=-((gNumber+100)/2-1)*scaledegrees:1*scaledegrees:... ((gNumber+100)/2-
1)*scaledegrees;
d=0:.001*distancesteps:(distance-1)*.001*distancesteps;
yscale=0:timesteps:(time-1)*timesteps;

    %initializing curves
x =initialcurve3; %Darwin Curve substrate

    %the angular convolution formula
convdegrees=.003/fwhmFact; %convolution fullwidth
a=1:100;
b=exp(-(a-50).^2/(2*(convdegrees/scaledegrees)^2));
    %plotting the substrate rocking curve with the angular convolution
xsmooth=conv(abs(x.^2),b); peak=max(xsmooth);
max2=length(xsmooth); subplot(2,2,2); plot(xscale2,xsmooth);
title('Rocking curve of the substrate (convultion included)');
xlabel('Delta Theta (degrees)'); xold=x; subplot(2,2,3);
title('Current Rocking Curve'); xlabel('Delta Theta (degrees)');

    %drawing the strain function
subplot(2,2,1);
title('Strain function');
xlabel('Depth (microns)');
ylabel('Strain');
output=zeros(time,gNumber); drawnow;

    Freal=abs(Freal);
    %Thickness steps in units of the diffraction scale
thickness=2.818e-15*gLambda*Freal/gVol...
/sqrt(gGamma0*gGammaH)*distancesteps*1e-9;

    %This is the main loop for dynamical diffraction
    %it can be sped up by commenting out the plots
    %it can also be sped up with the unequal bins
equalbin=0; %equalbin==0 unequal
output(1,:)=abs(x').^2; %make sure 1st curve is "virgin"
for t=2:time;

    %determine the depth dependent strain subplot(2,2,1);
strain = strainfun(t,:);
xold=x;

    %perform the rocking curve analysis of the strain if (equalbin =0)
```

```
%old method with equal bins
for depth = distance:-2:1
xnew=multilayer2(strain(depth), strain(depth-1),... thickness,xold);
xold=xnew;
end;
plot(d,strain,'b');
else

    %new method with unequal bins: caution numerical errors
[layer,theStrain]=unequal(strain,distance,0.0001);
numPoints=size(layer,2);
for depth = numPoints:-2:2; %stop at 2 in case odd
layerThick=thickness*(layer(depth)-layer(depth-1));
xnew=multilayer2(theStrain(depth), theStrain(depth-1)... ,layerThick, xold);
xold=xnew;
end;
plot(layer*0.001*distancesteps,theStrain,'r+');
hold on;
plot(d,strain,'b');
hold off;
end

    % plot strain
title('Strain function');
xlabel('Depth (microns)');
ylabel('Strain');
drawnow;
subplot(2,2,3);

    %calculated Rocking curves
output(t,:)=abs(xnew').^2; %this is the unconvoluted picture
new=conv(output(t,:),b);
newoutput(t,:)=new; %this is with the convolution  new=new/max(new);

    %plot Calculation
plot(xscale2,new);
title('Current Rocking Curve (no convolution included)');
xlabel('Delta Theta (degrees)');
drawnow;

    %end of main loop
end;

    %plotting the unconvoluted data
```

```
subplot(2,2,4);
surf(xscale,yscale,output);
title('Time-dependant diffraction curve (no convolution)');
xlabel('Delta Theta (degrees)');
ylabel('Time (ps)');
shading interp; view(2); axis tight;

    %plotting the convoluted data
subplot(2,2,3);
surf(xscale2,yscale,newoutput);
title('Time-dependant diffraction curve (convolution with Si)');
xlabel('Delta Theta (degrees)');
ylabel('Time (ps)');
shading interp; view(2); axis tight;
save('temp.mat'); 'data saved in temp.mat'
```

Strain Routine

```
    %This is the calculation of the time dependant Strain Profile

    function [strain]= timestrain(fluence,timesteps,distancesteps,conv);

    %contstants
intensity=fluence*10; %converting to J/m2^
R=0; %.17; %this is the optical surface reflectivity;
absorb=20200; %laser absorbtion length in Angstroms
density=5.3234e3; %kg/m3^
specificheat=321.9; %J/kg/K
beta=6.1e-6; %1/K
bulk= 1/.442e-10; %N/m2^
sound=5000; %m/s
area=3e-6; %m2^
taueph=10; %electron phonon relaxation time in ps
poisson=bulk*3/density/sound2^;
length=absorb*1e-10; %absorbtion length in meters
C=specificheat*density;
abslength=length*1e9; %absorbtion depth in 1 nm
v=sound/1000; %speed of sound in 1nm/1picoseconds

    %allow user input on maximum strain or optical fluence
if (fluence>0)
coeff=(1-R)*intensity*beta/length/C*poisson
else
coeff=-fluence;
end
```

```
    z= 1:4000; %Number of spatial steps
zprime=z.*distancesteps;
aa=0.5; %phonon amplitude aa=0.5 is normal
fudge=1; %phonon asymmetry
%strain0(1,:)=0;
    %main loop
for t =2:200; %number of time steps

    % For the phonon only strain0(t,z)=coeff*(exp(-zprime/abslength).*...
(.5*exp(-v*(t-1)*timesteps/abslength))-...
.5*exp(-abs(zprime-v*(t-1)*timesteps)/abslength).*...
sign(zprime-v*(t-1)*timesteps));

    %Thomsen model
strain0(t,z)=coeff*(exp(-zprime/abslength).*(1-aa*exp(-v*(t-1)...
*timesteps/abslength))-aa*exp(-abs(zprime-v*(t-1)...
*timesteps)/abslength).*sign(zprime-v*(t-1)*timesteps));

    %asymmetric acoustic pulse
if sign(z*distancesteps-v*(t-1)*timesteps)*2¿0
strain0(t,z)=coeff*(exp(-z*distancesteps/abslength).*...
(1-aa*exp(-v*(t-1)*timesteps/abslength/10))...
-aa*fudge*exp(-abs(z*distancesteps-v*(t-1)*...
timesteps)/abslength).*sign(z*distancesteps-v*(t-1)*timesteps));
else
strain0(t,z)=coeff*(exp(-z*distancesteps/abslength).*...
(1-aa*exp(-v*(t-1)*timesteps/abslength))...
-aa*exp(-abs(z*distancesteps-v*(t-1)*timesteps)...
/abslength/1).*sign(z*distancesteps-v*(t-1)*timesteps));
end;

    %Justin's Hyperbolic tanget model strain0(t,z)= coeff* ...
(exp(-zprime/abslength).*(-.5*exp(-v*(t-1)*timesteps/abslength)) ...
-.5*exp(-abs(zprime-v*(t-1)*timesteps)/(abslength)).* ...
tanh((zprime-v*(t-1)*timesteps)/(v*taueph)));
end; %end of main loop

    %for a phonon reflection
for t=2:200
z2=1:2000;
zprime2=z2.*.5;
strain2(t,z2)=strain0(t,z2)-strain0(t,4000-z2);
strain3(t,z2)=-strain2(t,(2001-z2))+...
coeff/4*(exp(-zprime2*distancesteps/abslength));
```

```
end;
strain0=strain3;
```

Perfect crystal substrate Routine

```
    %this is the initial rocking curve calculation
function [data] = initialcurve3()
global gRes gPsi01 gPsiH1 gK gG gBeta gNumber gSin2QB gTanQB gAlpha0;
B=-(1+i*gK);

    %main loop
for deltatheta = 1: gNumber
alpha=gAlpha0(deltatheta);
y=((1+gBeta)*gPsi01-gBeta*alpha)/(2*abs(gPsiH1)*sqrt(gBeta));
C=y+i*gG;
if abs((-B/(-C-sqrt(C2̂-B2̂))).̂(-1)) <=1
data(deltatheta) = (-B/(-C-sqrt(C2̂-B2̂))).̂(-1);
else
data(deltatheta) = (-B/(C-sqrt(C2̂-B2̂))).̂(-1);
end;
end;
data=data';
```

Multilayer Routine

```
    %This is the superlattice calculation
function [data] = multilayer(strain1, strain2, thickness, startcurve)
global gNumber gRes gPsiH1 gK gG gBeta gPsi01 gSin2QB gTanQB gAlpha0;
start=startcurve'; % initialize substrate
sin2bragg=gSin2QB; tanbragg=gTanQB;
gone=gG; gtwo=gG;
kone=gK; ktwo=gK; B1=-(1+i*kone); B2=-(1+i*ktwo);
alphaone = gAlpha0-gTanQB*gSin2QB*strain1;
yone=((1+gBeta)*gPsi01-gBeta*alphaone)/(2*abs(gPsiH1)*sqrt(gBeta));
C1=yone+i*gone;
alphatwo = gAlpha0-gTanQB*gSin2QB*strain2;
ytwo=((1+gBeta)*gPsi01-gBeta*alphatwo)/(2*abs(gPsiH1)*sqrt(gBeta));
C2=ytwo+i*gtwo;
s1=sqrt(C1.*C1-B1*B1);
s2=sqrt(C2.*C2-B2*B2);
P=(B1*B2-C1.*C2).*tan(s1.*thickness).*(tan(s2.*(thickness)))+s1.*s2;
Q1=C1.*s2.*tan(s1.*thickness);
Q2=C2.*s1.*tan(s2.*(thickness));
```

```
R1=s1*B2.*tan(s2.*(thickness));
R2=s2*B1.*tan(s1.*thickness);
T=(B1*C2-B2*C1).*tan(s2.*(thickness)).*tan(s1.*thickness);
Q=Q1+Q2;
R=R1+R2;
data = ((P-i*Q).*start+(T-i*R))./((T+i*R).*start+(P+i*Q));
data=data';
removenan = isnan(data);
[m,n] =find(removenan);
data(m)=data(m-1);
```

BIBLIOGRAPHY

BIBLIOGRAPHY

[1] C. Thomsen et al. Coherent phonon generation and detection by picosecond light pulses. *Phys. Rev. Lett.*, 53(10):989–992, 1984.

[2] C. Thomsen et al. Surface generation and detection of phonons by picosecond light pulses. *Phys. Rev. B*, 34(6):4129–4138, 1986.

[3] H.-Y. Hao and H.J. Maris. Study of phonon dispersion in silicon and germanium at long wavelengths using picosecond ultrasonics. *Phys. Rev. Lett.*, 84:5556–5559, 2000.

[4] H. Y. Hao and H.J. Maris. Experiments with acoustic solitons in crystalline solids. *Phys Rev B*, 64:064302, 2001.

[5] H. Y. Hao and H.J. Maris. Dispersion of the long-wavelength phonons in ge, si, gaas, quartz, and sapphire. *Phys. Rev. B*, 63:224301, 2001.

[6] G. C. Cho, W. Kutt, and H Kurz. Subpicosecond time-resolved coherent-phonon oscillations in gaas. *PRL*, 65(6):764–767, 1990.

[7] H. J. Zeiger et al. Theory for displacive excitation of cohernet phonons. *Phys. Rev. B*, 45(2):768–778, 1992.

[8] R. Merlin. Generating coherent thz phonons with light pulses. *Solid State Comm.*, 102(2):207–220, 1997.

[9] William H. Zachariasen. *Theory of X-ray Diffraction in Crystals*. John Wiley and Sons, Inc., 1945.

[10] B. E. Warren. *X-Ray Diffraction*. Dover Publications Inc., 1990.

[11] A. Authier, S. Lagomarsino, and B.K. Tanner, editors. *X-ray and Neutron Dynamical Diffraction: Theory and Applications*. NATO ASI Series, 1996.

[12] A. Hauer and S. J. Burns. Observation of an x-ray shuttering mechanism utilizing acoustic interruption of the borrmann effect. *Applied Phys. Lett.*, 27(10):524–526, 1975.

[13] I. R. Entin et al. X-ray acoustic resonance in a perfect silicon crystal. *Sov. Phys. Solid State*, 20(5):754–756, 1978.

[14] E. Zolotoyabko et al. Determination of ultrasound velocity and attenuation in single crystals by means of x-ray diffraction. *Rev. Sci. Instrum.*, 64(5):1274–1279, 1993.

[15] K. D. Liss et al. Towards a new (Q,t) regime by time-resolved x-ray diffraction: Ultra-sound excited crystals as an example. *Europhys. Lett.*, 40(4):369–374, 1997.

[16] J.S. Wark et al. Shock launching in silicon studied with use of pulsed x-ray diffraction. *Phys. Rev. B*, 35:9391–9394, 1987.

[17] J.S. Wark et al. Subnanosecond x-ray diffraction from laser shocked crystals. *Phys. Rev. B*, 40:5705–5714, 1989.

[18] J. S. Wark. Picosecond x-ray diffraction. *Contemporary Physics*, 37(3):205–218, 1996.

[19] C. Rose-Petruck et al. Picosecond-milliångström lattice dynamics measured by ultrafast x-ray diffraction. *Nature*, 398:310–312, 1999.

[20] M. Uesaka et al. Generation and application of femtosecond x-ray pulse. *Nucl. Inst. Meth. Phys. A*, 455:90–98, 2000.

[21] J.C. Kieffer et al. Ultrafast x-ray sources. *Phys. Fluids B*, 5:2676–2680, 1993.

[22] A. Rousse, C. Rischel, and J. Gauther. Colloquium: Femtosecond x-ray crystallography. *Rev. Mod. Phys.*, 17(15):17–31, 2001.

[23] C. Rischel et al. Femtosecond time-resolved x-ray diffration from laser-heated organic films. *Nature*, 390(6659):490–492, 1997.

[24] C.W. Siders et al. Detection of nonthermal melting by ultrafast x-ray diffraction. *Science*, 286(5443):1340–1342, 1999.

[25] A. Cavalleri et al. Anharmonic lattice dynamics in germanium measured with ultrafast x-ray diffraction. *Phys. Rev. Lett.*, 85(3):586–589, 2000.

[26] A. Cavalleri et al. Ultrafast x-ray measurement of laser heating in semiconductors: Parameters determining the melting threshold. *Phys. Rev. B*, page 193306, 2001.

[27] J. Larsson et al. Ultrafast structural changes measured by time-resolved x-ray diffraction. *Appl. Phys. A*, 66:587–591, 1998.

[28] R.W. Schoenlein et al. Femtosecond x-ray pulses at 0.4 angstroms generated by 90° thomson scttering: A tool for probing the structural dynamics of materials. *Science*, 274(5285):236–238, 1996.

[29] A.H. Chin et al. Ultrafast structural dynamics in insb probed by time-resolved x-ray diffraction. *Phys. Rev. Lett.*, 83(2):336–339, 1999.

[30] J. Larsson et al. Ultrafast x-ray diffraction using a strek-camera detector in averaging mode. *Optics Letters*, 22(13):1012–1014, 1997.

[31] A.L. Lindenberg et al. Time-resolved x-ray diffraction from coherent phonons during a laser-induced phase transition. *Phys. Rev. Lett.*, 84(1):111–114, 2000.

[32] G. A. Garrett et al. Coherent thz phonons driven by light pulses and sb problem: What is the mechanism? *PRL*, 77(17):3661–3664, 1996.

[33] S. Hunsche et al. Impulsive softening of coherent phonons in tellurium. *PRL*, 75(9):1815–1818, 1995.

[34] M. Hase et al. Optical control of coherent optical phonons in bismuth films. *Appl. Phys. Lett.*, 69(17):2474–2476, 1996.

[35] M. Hase et al. Selective enhancement of coherent optical phonons using thz-rate pulse tran. *Jpn. J. Appl. Phys*, 37:L281–L283, 1998.

[36] M.F. DeCamp et al. Dynamics and coherent control of high amplitude optical phonons is bi. *Phys. Rev. B*, 64:092301, 2001.

[37] T. E. Stevens, J. Hebling, J. Kuhl, and R. Merlin. Coherent phonon dynamics studied by impulsive stimulated raman scattering. *Phys. Stat. Sol. (b)*, 215:81–86, 1999.

[38] Troy E. Stevens. *Ultrafast dynamics of low energy elementary excitations in semiconductors*. PhD thesis, University of Michigan, 2000.

[39] Charles Kittel. *Introduction to Solid State Physics*. John Wiley and Sons, 1996.

[40] J.S. Wark. *Personal Communication*.

[41] S.A. Akhmanov and V. É. Gusev. Laser excitation of ultrashort acoustic pulses: New possibilities in solid-state spectroscopy, diagnostics of fast processes, and nonlinear acoustics. *Sov. Phys. Usp.*, 35(3):153–191, 1992.

[42] Charles Kittel and Herbert Kroemer. *Thermal Physics*. W.H. Freeman and Company, 1980.

[43] J.F. Young and H.M. van Driel. Ambipolar diffusion of high-density electrons and holes in ge, si, and gaas: Many-body effects. *Phys. Rev. B*, 26:2147–2158, 1982.

[44] A. Bartels et al. Coherent zone-folded longitudinal acoustic phonons in semiconductor superlattices: Excitation and detection. *PRL*, 82(5):1044–1047, 1999.

[45] K. Mizoguchi et al. Observation of coherent folded acoustic phonons propagating in a gaas/alas superlattice by two-color pump-probe spectroscopy. *Phys. Rev. B*, 60(11):8262–8266, 1999.

[46] T. Dekorsy et al. Coherent acoustic phonons in semiconductor superlattices. *Phys. Stat. Sol. (b)*, 215:425–430, 1999.

[47] A. Bartels et al. Coherent control of acoustic phonons in semiconductor superlattices. *Appl. Phys. Lett*, 72:2844–2846, 1998.

[48] U. Ozgur et al. Control of coherent acoustic phonons in semiconductor quantum wells. *Phys. Rev. Lett.*, 86:5064–5067, 2001.

[49] N.W. Ashcroft and N.D. Mermin. *Solid State Physics*. Saunders College publishing, 1976.

[50] B. Batterman and H. Cole. Dynamical diffraction of x rays by perfect crystals. *Rev. Mod. Phys.*, 36(3):681–716, 1964.

[51] J.M. Ziman. *Principles of the Theory of Solids*. Cambridge University Press, 1995.

[52] J.C. Slater. Interaction of waves in crystals. *Rev. Mod. Phys*, 30:197–222, 1958.

[53] S. Takagi. Dynamical theory of diffraction applicable to crystals with any kind of small distortion. *Acta Cryst.*, 15:1311, 1962.

[54] S. Takagi. A dynamical theory of diffraction for a distorted crystal. *Jour. Phys. Soc. Jpn.*, 26:1239–1253, 1969.

[55] D. Taupin. Théorie dynamique de la diffraction des rayons x par les cristaux déformé. *Bull. Soc. Franç. Minér. Crist.*, 87:469–511, 1964.

[56] C. R. Wie, T. A. Tombrello, and Jr. T. Vreeland. Dynamical x-ray diffraction from nonuniform crystalline films: Application to x-ray rocking curve analysis. *J. Appl. Phys.*, 59(11):3743–3746, 1986.

[57] C. R. Wie and H. M. Kim. Kinematical x-ray diffraction model with a new boundary condition for analysis of bragg-peak profiles of layered crystals. *J. Appl. Phys.*, 69(9):6406–6412, 1991.

[58] H.M. Bizek, editor. *The Advanced Photon Source List of Parameters*. Argonne National Labs, 1996.

[59] Albert C Thompson and Douglas Vaughan, editors. *Center for X-ray optics and Advanced Light Source: X-ray Data Booklet*. Lawerence Berkeley National Labs, 2001.

[60] A. Baron. A fast, convenient, x-ray detector. *Nucl. Instr. Meth.*, A400(1):124–132, 1997.

[61] R. Shepherd et al. Ultrafast x-ray streak camera for use in ultrashort laser-produced plasma research. *Rev. Sci. Inst.*, 68:719–721, 1995.

[62] Z. Chang et al. Demonstration of a sub-picosecond x-ray streak camera. *Appl. Phys. Lett*, 69:133–135, 1996.

[63] B.L. Henke et al. The characterization of x-ray photocathodes in the 0.1-19 kev photon energy region. *J. Appl. Phys.*, 52:1509–1520, 1981.

[64] J.A.R Samson. Photocathodes: Their efficiency and stability. *Nucl. Inst. Meth. Phys*, 222:215–220, 1984.

[65] S. Backus et al. High power ultrafast lasers. *Rev. Sci. Inst.*, 69:1207–1223, 1998.

[66] D. Strickland and G. Mourou. Compression and amplification of chirped optical pulses. *Optics Comm.*, 56:219–221, 1985.

[67] David R. Lide, editor. *Handbook of Chemistry and Physics*. CRC press, 1996.

[68] D. Reis, M. DeCamp, et al. Probing impulsive strain propagation with x-rays. *Phys. Rev. Lett.*, 86:3072–3075, 2001.

[69] N. C. Woolsey and J. S. Wark. Modeling of time resolved x-ray diffraction from laser-shocked crystals. *J. Appl. Phys*, 81(7):3023–3037, 1997.

[70] S. D. LeRoux, R. Colella, and R. Bray. X-ray-diffraction studies of acoustoelectrically amplified phonon beams. *PRL*, 35(4):230–234, 1975.

[71] S. D. LeRoux, R. Colella, and R. Bray. Effect of acousticelectric phonons on anomalous transmission of x rays. *PRL*, 37(16):1056–1059, 1976.

[72] G Borrmann and G. Hildebrandt. Rontgen-wellenfelder in grossen kalkspatkristallen und die wirken einer deformation. *Z. Naturforsch A*, 11:585–587, 1956.

[73] M.F. DeCamp et al. Coherent control of pulsed x-ray beams. *Nature*, 413:825–828, 2001.

[74] A.A. Maznev, T.F. Crimmins, and K.A. Nelson. How to make femtosecond pulses overlap. *Optics Letters*, 23:1378–1380, 1998.

[75] P.H. Bucksbaum and R. Merlin. The phonon Bragg switch: a proposal to generate sub-picosecond x-ray pulses. *S.S. Comm.*, 111(10):535–539, 1999.

[76] R. Neutze et al. Visualizing photochemical dynamics in solution through picosecond x-ray scattering. *Phys. Rev. Lett.*, 87:195508, 2001.

ABSTRACT

Seeing Sound: Dynamical Effects in Ultrafast X-ray Diffraction

by

Matthew F. DeCamp

Chair: Philip H. Bucksbaum

Time-resolved x-ray diffraction has become a very powerful tool in the study of structural dynamics of solids. The wave nature of x-rays allows the detection of milliÅngstrom changes in crystalline structure. Coupling the sensitivity of x-ray scattering with ultrafast pump-probe techniques can provide unprecedented studies of ultrafast dynamics in solids. This thesis demonstrates how time-resolved x-ray diffraction can be used to view transient strains in crystalline solids. Several different x-ray scattering geometries are explored.

In the Bragg scattering geometry, laser generated picosecond acoustic phonons in single crystal Ge and InSb are analyzed. Comparisons with dynamical diffraction theory have shown that the accepted theory of laser driven acoustic phonons is inconsistent with the observed data. It is also observed that the dispersion associated with pulse propagation is much larger than expected.

In the Laue scattering geometry, studies using single crystal Ge, InSb, and GaAs have demonstrated a direct coupling between the ultrafast acoustic pulse and the diffracting x-ray pulse. Qualitative agreement is found between the observed data and a simple two crystal model. In the two crystal model the acoustic pulse is assumed to be a moving thin interface lying between two unstrained thick crystals. The resulting moving interface causes time-dependent Pendellösung oscillations in the diffracted beams. It is also shown that this coupling is dependent on the direction of the acoustic phonon when compared to the reciprocal lattice vector. The generation of an acoustic pulse causes an ultrafast coherent transfer of population between the two diffracting beams. The time scale for this diffraction effect ranges from 10-300ps. Several potential mechanisms describing the physics behind this phenomena are proposed, but exact nature of this diffraction effect is not known and requires further study.